UNIVERSITÀ DEGLI STUDI DI PADOVA

DIPARTIMENTO DI INGEGNERIA INDUSTRIALE

DIPARTIMENTO DI TECNICA E GESTIONE DEI SISTEMI INDUSTRIALI

in collaborazione con

ROLLS-ROYCE UTC - DEPT. OF MATERIALS SCIENCE & METALLURGY

UNIVERSITY OF CAMBRIDGE

CORSO DI LAUREA MAGISTRALE IN INGEGNERIA DEI MATERIALI

Tesi di Laurea Magistrale in Ingegneria dei Materiali

ON THE PHASE STABILITY OF $Al_xCrFeCoNiCu$ HIGH ENTROPY ALLOYS

Relatore: ***Prof. Franco Bonollo***

Correlatori: ***Prof. Andrea Zambon***

Dr. Howard Stone

Dr. Nicholas Jones

Laureando: Frezza Aligi

ANNO ACCADEMICO: 2012/2013

A mia Nonna Milena

e alla mia famiglia

TABLE OF CONTENTS

LIST OF FIGURES

LIST OF TABLES

1. INTRODUCTION

1.1 PURPOSE OF THE STUDY

High Entropy Alloys (HEAs) were firstly defined by Yeh *et al.* in 2004 [1] as alloys "composed of five or more principal elements in equimolar ratios. In order to extend the scope of alloy design, HEA may contain principal elements with the concentration of each element being between 35 and 5 at.%". Their distinctive property is the ability to form simple solid solution phases with face centred cubic (*fcc*) or body centred cubic (*bcc*) [1]. Single simple solid solution is not expected accordingly to the traditional understanding of physical metallurgy since the formation of intermetallic compounds is predicted.

According to Yeh [1], the stability of solid solutions of many elements is due to the large mixing entropy of a system containing five or more elements that is able to overwhelm the formation enthalpy of intermetallic compounds and to stabilise the random solid solution, as further explained in §2. Thanks to the formation of these advocated simple single solid solutions without a principal matrix element, all the elements play the role of solute providing to the alloy high strength and hardness, high annealing softening resistance, high wear and fatigue resistance, high corrosion and oxidation resistance [1]–[9]. Furthermore, since the entropy contribution to solid solution stability is increased at higher temperature, these alloys are supposed to have elevated thermodynamic phase stability at higher temperature. Moreover, given the multi-principal element matrix of these alloys, diffusion is expected to be sluggish and then phase transformation are kinetically prevented even at lower temperature [1].

All these suggested properties, especially creep resistance and high temperature phase stability, make these alloys attractive innovative materials for high temperature applications, as in aerospace industry. The AlCrFeCoNiCu system (§2.1.3) is the most largely investigated since it is based on the elements that constitute the traditional alloys employed in aerospace industry, as Ni-based superalloys. The interests on these possible applications has lead Yeh to obtain a patent about HEAs in 2002 [7].

However, the presumed excellent phase stability of these alloys is still under debate since several studies have detected phase transformation and precipitation following heat treatment at high temperature [10]–[12]. Similar phenomena have been confirmed in a previous work conducted by Dr. Jones N. *et al.* at the Rolls-Royce UTC (Department of Materials Science and Metallurgy – University of Cambridge, UK) [13].

Hence, the purpose of the study is to investigate the phase stability of $Al_xCrFeCoNiCu$ HEAs during long term high temperature exposure in order to evaluate the feasibility of application of these materials in high temperature devices.

1.2 RESEARCH QUESTIONS AND HYPOTHESIS

1.2.1 HEAs Phase Stability

As stated in the previous section §1.1 and more in detail described in §2.1.3, several works have casted doubts on the extent of the stabilising effect of the configurational entropy in HEAs given the presence of intermetallic compounds after relatively short aging treatments (5-72h) or thermo-mechanical treatments [10]–[12]. Whilst this does not alter the fact that the microstructure subsequently decomposed during aging, it is not possible to separate thermo-mechanical effects from purely thermodynamics processes and neither to be confident that the aging time was sufficient to allow the diffusion process to occur completely and then to reach the thermodynamic equilibrium (given that slow diffusion rate is expected in HEAs, as argued in§1.1, and more in detail in §2.1.1).

Therefore, in this thesis the $Al_xCrFeCoNiCu$ HEAs were submitted to very long aging treatment of 1000 hours at several temperatures (700°C, 850°C and 1000°C) directly from the as cast condition and then water quenched in order to freeze the high temperature microstructure to room temperature. The 1000 hours aging time is hypothesised to be enough to allow to the system to reach the thermodynamic equilibrium structure even if kinetic constraints due to sluggish diffusion may subsist in HEAs. Hence, after quenching, the investigated samples are supposed to be representative of the equilibrium microstructure at the respective temperature. In this way it is possible to answer to the question if phase separation and intermetallic

formation are thermodynamic suppressed by the configurational entropy change due to the mix of six elements. Moreover, it is also possible to determine the extent of the kinetic prevention to phase separation and atomic ordering (intermetallic formation) looking at the as cast sample (air cooled) and at the DSC measurements. All the techniques employed (§0) revealed several intermetallics and phase segregation after the long aging treatment at high temperature (§4), implying that they are the thermodynamic stable phases and casting doubts on the extent of configurational entropy stabilisation.

1.2.2 Phase prediction according to ternary diagrams

The evidence of the fact that intermetallic phases and multiple solid solutions are the thermodynamic stable phases suggests that they may be predicted by the means of opportune ternary phase diagrams. Previous works by Otto *et al.* (2013) [14] and Senkov *et al.* (2013) [15] suggested a direct correlation between the phases found in the binary diagrams of any two elements contained in the alloy.

The extended review of the known ternary diagrams allowed to rationalised the phase detected and to predict the intermetallic precipitation and phase separation accordingly to the solubility limits and phase equilibriums from isothermal section or vertical sections of ternary diagrams. Hence, the concept of HEAs as "new and uncharted territory, in which many possible new materials, new phenomena, new theories and new applications are awaiting to be discovered" (Yeh *et al.* [1]) should be revised since the phased formed in the HEAs are described by the conventional metallurgy and since the possibility to create single simple solid solution mixing five or more elements is not thermodynamically guaranteed by the configurational entropy (i.e. increasing the number of alloying elements) only.

1.2.3 Survey program

In order to answer the questions in §1.2.1 and §1.2.2, the following survey program was performed (as described in §0):

1. Three Al_xCrFeCoNiCu alloys with different Al content (x=0.5, 1 , 3) were investigated in order to evaluate the compositional influence over microstructure and phase equilibriums;

2. 1000 hours long aging heat treatments at three different temperatures (700°C, 850°C and 1000°C) for each alloy in order to assure the achievement of the thermodynamic equilibrium and then water quenched to freeze the microstructure;
3. Scanning Electron Microscopy in Back Scattered Electron Mode EM on the as cast and aged samples in order to identify the phases are formed in each condition;
4. EDX microanalysis and elemental maps in order to evaluate phase compositions and elements partitioning in different phases;
5. X-Ray diffraction in order to identify the crystallographic structures in the sample and to relate them with micrographic observation, EDX data and ternary diagrams;
6. Differential Scanning Calorimetry in order to monitor the formation of phases upon heating and cooling and to verify the happening of ordering transformation;
7. Wide ternary diagram review in order to explain the formation of the equilibrium phases detected.

1.3 SIGNIFICANCE OF THE STUDY

This study aims to contribute to the debate concerning the phase stability of the HEAs when exposed to high temperature for long time. Indeed, contrarily to previous works, the heat treatments applied in this project are assumed to be long enough to allow the system to reach the thermodynamic equilibrium permitting to verify the extent of the supposed high entropy stabilisation effect on single solid solutions against intermetallics and phase separations.

Given the advocated properties of HEAs in terms of high temperature phase stability and strength, which make HEAs attractive new materials for high temperature applications, the relevance of this study lies on the evaluation of the actual feasibility to employ $Al_xCrFeCoNiCu$ HEAs as high temperature structural materials in the aerospace industry. Indeed, it is well known that the pursuit for materials able to bear higher temperature performs a strategic role in enhancing engines efficiency and then the evaluation of new candidate materials fulfil a primary importance role.

2. LITERATURE REVIEW

2.1 HIGH ENTROPY ALLOYS

2.1.1 Role of Configuration Entropy

The phrase "High Entropy Alloys", HEAs, was for the first time adopted by Yeh *et al.* (2004) [1] to describe alloys "composed of five or more principal elements in equimolar ratios. In order to extend the scope of alloy design, HEA may contain principal elements with the concentration of each element being between 35 and 5 at.-%". Their distinctive property is the ability to form simple solid solution phases with face centred cubic (*fcc*) or body centred cubic (*bcc*), contrarily to traditional metallurgy predcitions. However, Cantor *et al.* (2004) [16] were the first to report that an equiatomic alloy consisting of the five transition metals Co, Cr, Fe, Mn and Ni crystallized as a single solid solution phase and they referred to this alloy as a multi-component alloy. From a traditional metallurgical point of view, such mixture would be expected to form several intermetallic compounds according to Hume-Rothery rules for alloying [17][1]. Nevertheless, XRD from these alloys has shown only simple solid solution such as *fcc* and *bcc* [1], [8], [9], [18]–[25]. The suppression of intermetallic phases in such alloys has been rationalised by Yeh *et al.* [1] suggesting that the configurational entropy of random solid state solution counterbalances the enthalpy of formation of intermetallic phases. Hence, according to this theory, the high configurational entropy of HEAs is considered sufficient to thermodynamically stabilize a single-phase solid solution against intermetallics via a reduction of the Gibbs free energy [1], [2], [8], [9], [18], [19], [23].

[1] Hume-Rothery rules [17] are here briefly recapped:

1. Atomic Size Rule: extensive substitutional solid solution occurs only if the relative difference between the atomic radii of the two species is less than 15%. If the difference > 15%, the solubility is limited.
2. Crystal Structure Rule: for appreciable solid solubility, the crystal structures must be identical.
3. Valency Rule: a metal will dissolve a metal of higher valency to a greater extent than one of lower valency. Solute and solvent should have the same valence in order to achieve maximum solubility.
4. Electronegativity Rule: Electronegativity difference close to zero gives maximum solubility. The greater the electronegativity difference, the greater is the likelihood that they will form an intermetallic instead of a substitutional solid solution.

The variation of Gibbs free energy between solid solution and the pure metals mixture ΔG_{mix} is given by Eq. 2.1:

$$\Delta G_{mix} = \Delta H_{mix} - T\Delta S_{mix} \qquad \textbf{Eq. 2.1}$$

ΔH_{mix} is the enthalpy change associated with the fact that interactions between A and B atoms are not the same as those between A–A pairs or B–B pairs. Three cases are then possible:

- $\Delta H_{mix} = 0$: A–B interactions are energetically equivalent to A–A and B–B interactions and then the system can form an ideal solid solution. For the ideal solution is then $\Delta G_{mix} = -T\Delta S_{mix}$, i.e. the constituents do not introduce significant enthalpy contributions.
- $\Delta H_{mix} < 0$: A–B interactions are energetically more favourable than A–A and B–B interactions. This provides for the tendency to form an ordered structure, i.e. an intermetallic compound;
- $\Delta H_{mix} > 0$: A–A and B–B interactions are energetically more favourable than A–B interactions. This provides for the tendency for the solution to segregate into A-rich and B-rich regions [26].

ΔS_{mix} consists of several contributes like vibrational, electronic, magnetic moment randomness. The main contribution to solid solution is given by ΔS_{conf} i.e. the variation of configurational entropy between a random solid solution and the pure metal mixture. According to Boltzmann's equation between entropy and system complexity entropy, ΔS_{conf} during the formation of a solid solution from *n* elements with equimolar ratio is given by Eq. 2.2 [1]:

$$\Delta S_{conf} = -k \ln \omega = R \ln n \qquad \textbf{Eq. 2.2}$$

Where k is the Boltzmann's constant, ω the number of distinguishable ways of arranging the atoms on the available sites and R is the gas constant $8.314\ \mathrm{J/K\,mol}$. Consequently, ΔS_{conf} for equimolar alloys with 3, 5, 6 elements is $1.10R, 1.61R, 1.79R$ respectively [1]. These values are considered high since the value of the entropy change during melting is approximately *R* according to Richards' law [27]. The role played by $\Delta S_{conf} \cong \Delta S_{mix}$ is supposed to be twofold.

Firstly, it can extend single solid solution field to systems, as Cantor's alloy CoCrFeMnNi, which should not form one single solid solution according to Hume-Rothery rules. Indeed, these five elements have four different crystal structures at room temperature (Co hexagonal close-packed *hcp*, Cr and Fe body-centred cubic *bcc*-A2, Mn A12 cubic structure and Ni face-centred cubic *fcc*-A1) and some pairs differ in electronegativity more than 20% [14]. Moreover, this five element equimolar alloy has a configurational entropy contribution to ΔG_{mix} ($-T\Delta S_{mix}$) at 1000°C of $-17.04\ \mathrm{kJ/mol}$ and then it is able to counterbalance a positive ΔH_{mix} up to about $10\ \mathrm{kJ/mol}$ thus allowing effective mixing between typically incompatible elements [28].

Secondly ΔS_{conf} is supposed to make solid solution thermodynamically more stable than intermetallic compounds. Briefly, in systems where there is strong chemical bonding between the atoms ($\Delta H_{mix} \ll 0$) there is a tendency for the formation of intermetallic phases. These are distinct phase from solutions based on the pure components since they have a different crystal structure and may also be highly ordered. Since they are a different phase, they follow their own Gibbs free energy curve. Hence, the variation of Gibbs free energy ΔG_{form} during formation of the intermetallic phase from a pure metal mixture is given by Eq. 2.3:

$$\Delta G_{form} = \Delta H_{form} - T\Delta S_{form} \qquad \textbf{Eq. 2.3}$$

Where ΔH_{form} and ΔS_{form} are the variation enthalpy and entropy during the intermetallic formation. Entropy change of mixing during the formation of intermetallic compounds ΔS_{form} is usually not elevated [26]. For example for the NiAl intermetallic (one amongst the strongest intermetallic) ΔS_{form} is evaluated around $1.56R$ [29]. This value is lower than ΔS_{conf} of a five or six element HEA. Hence, ΔS_{conf} of HEAs is comparable and even larger of ΔS_{form} of intermetallics. Consequently, HEAs will more easily promote the formation of random solid solution during solidification rather than intermetallic compound, except for those with very large negative enthalpy of formation ΔH_{form}. Indeed, the solid solution will form if the variation of Gibbs free energy for solid solution ΔG_{mix} is more negative than the variation of Gibbs free energy of intermetallic formation ΔG_{form} , as shown by Eq. 2.4:

$$\Delta H_{mix} - T\Delta S_{conf} < \Delta H_{form} - T\Delta S_{form} \qquad \textbf{Eq. 2.4}$$

Therefore, given that it is supposed that $\Delta S_{conf} > \Delta S_{form}$, the configurational entropy may provide a solid solution stabilisation even if $|\Delta H_{mix}| < |\Delta H_{form}|$ ($\Delta H_{mix} = 0$ for ideal solid solution).

The multi-principal element solid solutions stabilised by ΔS_{conf} are supposed to exhibit the following properties [1], [3], [4], [8], [9]:

- Phase stability: ΔS_{conf} provides a thermodynamic stabilisation of solid solution and its contribution is enhanced at higher temperature. Even if the ΔS_{conf} stabilising effect is reduced by lowering the temperature, partitioning and phase separation are prevented by the sluggish diffusion in a multi-principal element matrix;
- Ultrafine microstructure: the absence of a principal element matrix reduce the long-range diffusion so that nucleation and growth rate are lowered and nanosized grains obtained;
- High strength: since there is no principal matrix element, all the atoms play a role of solute giving solution strengthening effect, enhanced by the nanosized grains effect;
- Hot hardness: significant solution hardening and lower vacancy mobility due to multi-principal-element composition have contributions to softening resistance;
- Resistance to corrosion and resistance to oxidation at high temperature up to 1100°C.

These promising properties have attracted extensive interest on these materials since they may be attractive for high temperature applications like in the aerospace industry [1], [7]–[9], [20], [30].

2.1.2 Extent of Configurational Entropy Stabilisation Effect

Several recent studies conducted also at the Rolls-Royce UTC, Department of Materials Science & Metallurgy (University of Cambridge) by Dr. Nicholas Jones *et al.* [13] have launched some doubts about the extent of the stabilisation provided by configurational entropy. There are three main contributions to the questions raised about the actual ability to form single solid solutions by HEAs:

1. Some inaccuracies in the interpretation of extra peaks in XRD diffractograms are found in some studies, as described in §2.1.3 ([1], [2], [8], [9], [31]–[33]).
2. Some studies about HEAs have reported segregation and the consequent formation of another entropically stabilised phase [2], [5], [12], [23], [28], [33]–[35] as well as age hardening effects and microstructural evolution and precipitation following heat treatment at elevated temperature [10]–[12], [14], [32], [36]–[42]. The precipitates detected in these investigations are often intermetallic compounds like NiAl, σ, Laves phases and γ'. Examples are provided in §2.1.3.
3. The use of many elements in nearly equimolar ratios is not a sufficient condition to ensure individual solid solutions. This point is largely discussed in this section.

Cantor *et al.* [16] had demonstrated that simply increasing the system complexity (i.e. increasing the number of alloying elements) did not significantly extend single-phase stability in multi-component alloys. To support that, they produced an alloy containing 20 elements. Such an alloy is supposed to have a significantly greater configurational entropy than the five-element CoCrFeMnNi alloy, but it nevertheless resulted in a multi-phase microstructure [16]. Interestingly, they found that the primary *fcc* solid solution phase in the 20-element alloy prevalently consisted of its original five elements. This suggests that other factors, such as good chemical compatibility among the elements Co, Cr, Fe, Mn and Ni, are more important in determining the microstructural state than configurational entropy.

This concept was largely analysed by Otto *et al.* (2013) [14]. Their approach was based on the premises that if any one of the elements in Cantor's alloys is replaced by another element the configurational entropy of the alloys is, to first approximation, unchanged. The substitution elements were chosen in order to be as closely as possible in terms of atomic radius and electronegativity, i.e. as close as possible to the miscibility requirements stated by Hume-Rothery rules [17]. The ideal solid solution Gibbs free energy can be expressed by (§2.1.1):

$$\Delta G_{mix-id} = -T\Delta S_{conf} \qquad \textbf{Eq. 2.5}$$

Considering $\Delta S_{mix-id} \approx \Delta S_{config}$; $\Delta H_{mix-id} = 0$. This is a very rare condition since it required that all the constituents do not introduce any substantial enthalpy and no-configurational entropy contributions. Considering this premise, the relevant question is

"how far can the Gibbs free energy of the alloy deviate from that of an ideal solid solution and still result in a single –phase solid solution?" [14]. They answered this question calculating the thermodynamic data of the minimum energy state ($\Delta G, \Delta H, \Delta S$) at equimolar ratio for the ten binary subsystems contained in each alloy. The minimum energy state of each system (equilibrium state) can consist of non-ideal solid solution phases or intermetallic compounds (as will be discussed in §2.2.1). The calculated $\Delta G, \Delta H, \Delta S$ are not only related to pure mixing effects but can also include energies of formation of second phases. Afterwards, they compared these values to the ones relative to the ideal solid solution and they calculated the deviation (G_D, H_D, S_D) between the real equilibrium state and the ideal one ($G_D = \Delta G - \Delta G_{mix-id}$; $H_D = \Delta G - 0$; $S_D = \Delta S - \Delta S_{conf}$). For example for the Cantor's single phase quinary alloy CoCrFeMnNi deviation values are shown in Fig. 2.1. The deviation from the ideal state is really small. Therefore, in the quinary system composed of these binaries, these small energy differences can be effectively counterbalanced by the formation of an *fcc* solid solution with a higher configurational entropy provided by the increased number of elements (from two to five). Consequently, the thermodynamic properties of Cantor's alloy are enough close to those of an ideal solid solution that configurational entropy is sufficient to overcome any tendency to form intermetallic or secondary solid solution phase.

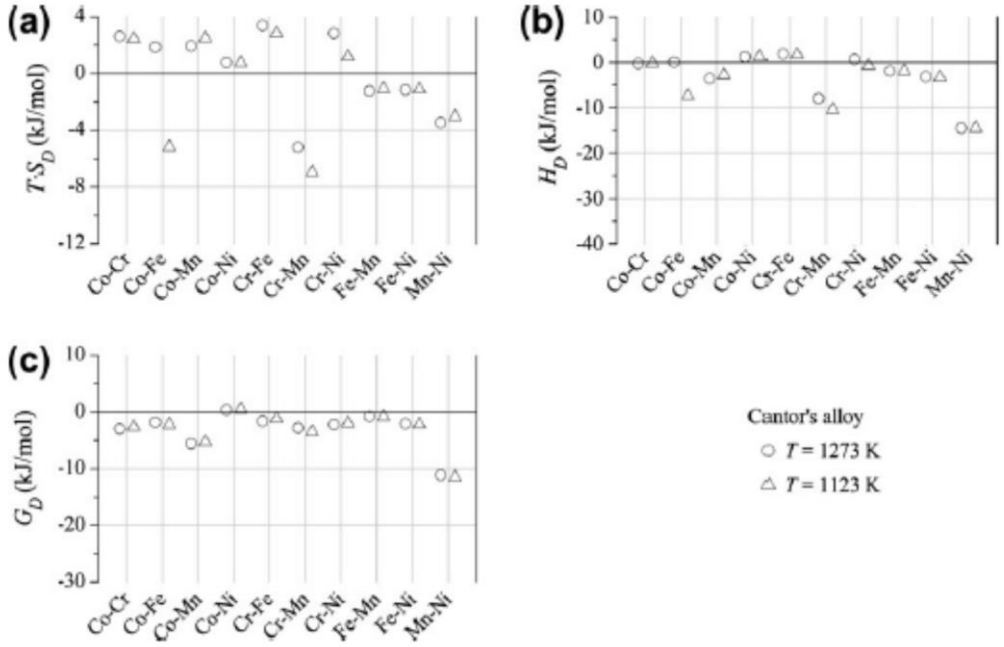

Fig. 2.1: Calculated deviations of (a) entropy, (b) enthalpy and (c) Gibbs free energy for all binary element pairs in the base CoCrFeMnNi alloy.
The depicted values correspond to equiatomic alloys at 1123 K (triangles) and 1273 K (circles). From Ref. [14]

The substitution of Cr with Mo and V leads to binaries systems that have much larger deviation from the ideal solid solution as shown in Fig. 2.2.

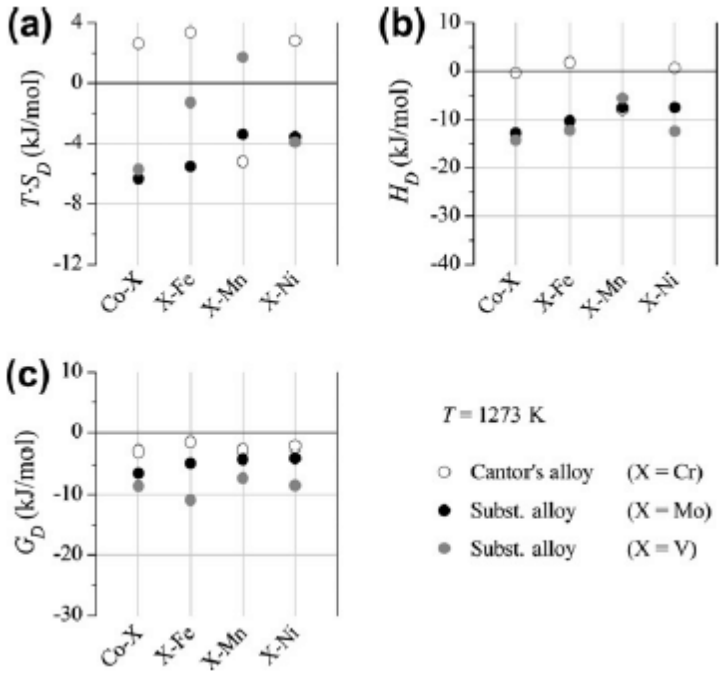

Fig. 2.2: Changes in the deviation of (a) entropy, (b) enthalpy and (c) Gibbs free energy for all binary element pairs as a result of replacing Cr in the base CoCrFeMnNi alloy (open symbols). With either Mo (black symbols) or V (grey symbols). The depicted values correspond to equiatomic alloys at 1273 K. Ref. [14]

This large deviation is due to the fact that intermetallic compounds are predicted by the binary diagrams of MoCo, FeMn (μ phases), MoNi (δ phase) and CoV and FeV (σ phase) [14]. Interestingly, both μ and σ phases, predicted by the binaries, are found in the microstructure of the quinary alloy [14]. This phenomenon is observed by Otto *et al.* [14] also in other substituted alloys. This investigation pointed out that phase formation in five-component alloys is consistent with a minimization of the total Gibbs free energy, including both enthalpy and entropy contributions and not just with a maximization of the sole configurational entropy. Indeed, an energy reduction is realised by precipitation of intermetallic compounds and the formation of segregated solid solution. Moreover, the intermetallics found in the alloys are the same formed by those elements in the alloy that are prone to form intermetallic when alloyed as binary pairs. Therefore, the ΔS_{conf} is not sufficient to counterbalance the intermetallic phase stability seen in binary systems due to the enthalpy of formation. "This finding casts doubt on the usefulness of an alloying strategy that consists merely of increasing the number of alloying elements if the

ultimate goal is to produce a single-phase solid solution microstructure" [14]. Similar conclusions are drawn also in other works [12], [34], [37], [43].

The fact that the trend observed in the binary diagram has direct repercussions on the multi-component alloys was used by Senkov *et al.* to design refractory single solid solution high entropy alloys [15], [20]–[22]. Indeed, Senkov's alloys are based on refractory metals that when alloyed in pairs exhibits a predisposition to form extensive solid solutions, for examples: WNbMoTa and WNbMoTaV [6],[7], TaNbHfZrTi [22] and NbTiVZr [15] are A2 (disordered *bcc*). Senkov's work suggests that a reasoned selection of the elements constituting a multi-principle alloys, i.e. among elements whose binary phase diagrams show wide disordered solid solution field [15]. In this way all the elements are prone to mix together rising the ΔS_{conf} contribute that can therefore provide an effective stabilization role in lowering the Gibbs free energy of the single solid solution phase under the Gibbs free energy of intermetallics.

2.1.3 AlCrFeCoNiCu HEAs

The alloys investigated in this work belong to the system Al_xCrFeCoNiCu. These alloys (also without Cu) have been the most largely investigated in recent years since they are based on elements employed in traditional high temperature structural metals, as Ni-based superalloys (AlCrFeCoNiCu: [1], [2], [12], [18], [19], [25], [28], [33], [34], [39], [42], [44]–[47]; AlCrFeCoNi: [10], [31], [32], [38], [48]–[52]).

Some studies on them have reported only simple solid solution (*bcc* A2 or *fcc* A1) on the XRD diffractograms ([1], [2], [8], [9], [31]–[33]). In these cases, reflection peak of the {100} planes was detected and labelled "ordered *bcc*", but not clearly attributed to intermetallic. Actually, this reflection, absent in solid solution (A2 and A1), is due to superlattice reflections of intermetallic compounds, as it will be discussed in §2.2.2.

Moreover in many works Cu-rich segregation into the interdentrites is reported to form because of the highly positive ΔH_{mix} with Co, Fe and Cr (respectively: 6, 12 and 13 kJ/mol [53]) that is too high to be counterbalanced by ΔS_{conf}. This leads to the fact that copper dislikes mixing in dendrite with Co, Fe and Cr and then separates into the interdentrites ([2], [5], [12], [23], [28], [33]–[35]).

Also the role of Al has been largely discussed. Increasing its amount in the alloy $Al_xCrFeCoNi(Cu)$, with $0 \leq x \leq 3$, the system changes its crystal structure from *fcc* to *bcc*, with a dual phase field at intermediate amount of Al ([1], [23], [31], [38], [50]). Furthermore, rising the Al amount increases the hardness and strength of the alloy, reducing its ductility and changing the fracture mechanism from ductile to cleavage [23], [33], [36], [54]. According to [23], [33], these observations are due to the lattice distortion introduced by Al (the biggest atom among the alloy constituents) and to the fact that *bcc* is harder to deform than *fcc* since slip along the {110} *bcc* planes is harder than along the {111} *fcc* planes (the latter are denser and then more spaced each other) [55]. However, other investigations [36], [38], [49], [54] have revealed that the increase of Al promotes precipitation of NiAl intermetallic (§2.3.1): the strengthening mechanism promoted by Al is not only based on lattice distortion but to the formation multiphase alloys and intermetallics. In particular, this can account for the brittle fracture met by the Al-rich alloys since strong intermetallics like NiAl are known to be brittle. Indeed[56] plastic deformation is more difficult in intermetallics than in metals and conventional metals alloys because of the stronger atomic bonding and the resulting ordered atomic distribution [56].

Precipitation of NiAl has been detected also after aging and annealing heat treatment at high temperatures [10], [11] or after thermo-mechanical treatments [12]. These results cast question about the extent to which the entropic stabilisation can be used to control microstructure given that at high temperature the configurational entropy should be enhanced and then provide a stabilisation effect to solid solution against intermetallics.

2.2 INTERMETALLIC COMPOUNDS

2.2.1 Thermodynamic considerations

The previous model to quantify the ΔG_{mix} for solid solution formation, known as "Regular Solution Model", is an oversimplification and its practical use is rather limited. In non-ideal alloys ($\Delta H_{mix} \neq 0$), the assumption that a random arrangement of atoms is the equilibrium or the most stable arrangement is not correct. Indeed inreal alloys, the actual arrangement of atoms will be a compromise that gives the lowest possible value of enthalpy (bonding energy) consistent with sufficient entropy (randomness), to achieve the lowest value of Gibbs free energy. As already indicated, if $\Delta H_{mix} < 0$, the energy of the system is reduced by increasing the number of A-B bonds, i.e. by ordering. On the contrary, if $\Delta H_{mix} > 0$ the energy is reduced by increasing the number of A-A and B-B bonds, i.e. by the clustering atoms into A-rich and B-rich regions. However, the degree of ordering or clustering will decrease as temperature increases due to the increasing importance of entropy. Tendency for the formation of intermetallic compounds happens when there is a strong chemical bonding between the atoms. Hence intermetallics are highly long-range ordered and with different crystal structure respect to the solid solution. Such a phase is considered to be a distinct (ordered) phase separate from the random or nearly random solution. The atom sites are no longer equivalent and can be identified as A-sites and B-sites. Therefore the whole lattice structure is described as an A_xB_y superlattice. The crystal structure of an intermetallic is determined by the strength and character of bonding in the crystal, which depends on the particular electronic configuration. The relation between structure type and atomic properties of the constituent atoms, however, is not simple and thus various criteria have been used for correlating structure and phase type [56]. Some simple intermetallics are shown in Fig. 2.3.

The entropy of mixing of ordered structures is extremely small and with increasing temperature the degree of order decreases and above some critical temperature there is no long-range order at all. The critical temperature is at its maximum when the composition is the ideal required for the superlattice. When the composition deviates from the ideal it is easier to disrupt the order with increasing temperature and the critical temperature is lower.

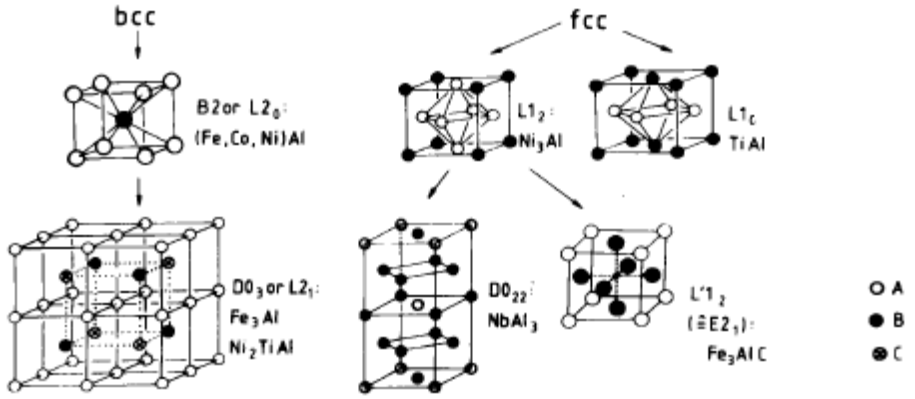

Fig. 2.3: Some simple intermetallic structures derived from *bcc* and *fcc* structures. From Ref. [56]

2.2.2 Intermetallic Superlattice Reflections in XRD

The superlattice structure of intermetallic has important consequences in XRD diffractograms. Indeed, depending on the type of Braives lattice, or more precisely if it is P (primitive), F (face centred) or I (body centred), the reflection according to Bragg' law can occurs only if precise conditions are respected by the Miller indexes of the family of planes, as shown in Table 2.1 [57].

Lattice Type	Condition for Presence
P	none
I	h + k + l= 2n
F	h, k, l all odd or all even

Table 2.1: Conditions for reflection according to the lattice type

In an intermetallic compound atoms occupy specific sites, meaning that, considering for example the B2 structure derived from the *bcc* in Fig. 2.3, A and B atoms are at the corners or centres of the unit cell (A and B sublattices respectively), creating the long-range ordering described as superlattice. This denomination could be ambiguous since it suggests the existence of lattices other than the 14 Bravais lattices. Ordering rather consists of a change of lattice type. Indeed, since there are two different atoms, the repeating element in the space (the motif) is not just A or B, but is A+B. Hence, the *bcc* structure of B2 implies a change from Cubic I to Cubic P and the *fcc* structure of $L1_2$ a change from Cubic F to Cubic P [57]. As a consequence, reflections that are forbidden for a random *bcc* or *fcc* are allowed in an ordered *bcc* or *fcc*. For example, reflection of {100} planes is forbidden in the Cubic I (random *bcc*) but is allowed in the Cubic P (ordered *bcc*).

2.3 TERNARY PHASE DIAGRAMS REVIEW

The review of the ternary diagrams derived from any three of the constituents of the AlCrFeCoNiCu alloys have been analysed in order to identify solubility limits, phase equilibriums and intermetallic compounds. This analysis allowed to interpret the data from XRD, micrographs and EDX microanalysis and to make predictions about phases present in the alloy after aging treatments. In this chapter only the data related to the relevant phases met during this work are presented. All the diagrams are taken from ASM Alloy Phase Diagram Database™ (APD) website [58].

2.3.1 NiAl B2

Although Ni and Al possess the same crystal structure so that complete mutual solid solubility might be anticipated, the binary Ni–Al system exhibits a number of solid phases other than the *fcc* one, as shown in Fig. 2.4. These phases possess an intermetallic nature given by the significant degree of directional, covalent bonding such that precise stoichiometric relationships exist between the number of Ni and Al atoms in each unit cell. As stated in §2.1.1 and §2.2.1, this results derives from the highly negative enthalpy of formation since Ni–Al rather than Ni–Ni or Al–Al bonds are preferred (Fig. 2.5).

NiAl is the best known example of the intermetallics with a cubic B2 structure (Fig. 2.3), which form one of the largest groups of intermetallics [56] with lattice parameter of 2.8863Å [59]. Ni occupies the sites at the centre, Al the sites at the corners [49].

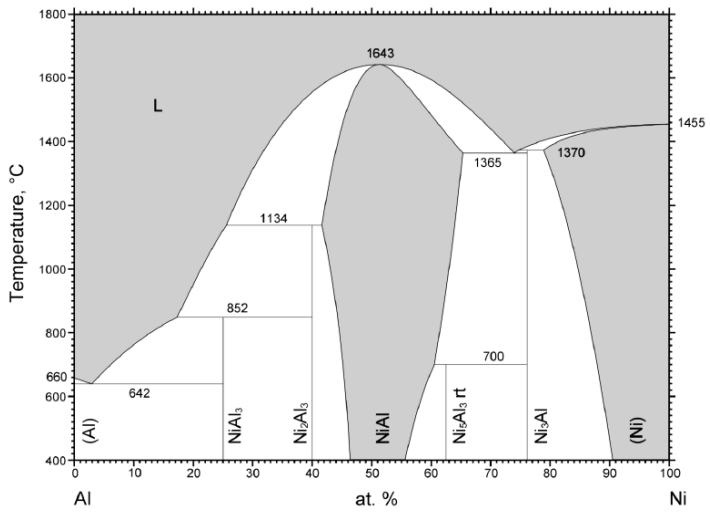

Fig. 2.4: Binary phase diagram of NiAl. From ASM APD [56]. Ref: [60]

The phase NiAl has an extended range of homogeneity and melts congruently at about 1643°C for the stoichiometric composition with 50 at.% Al. This melting point, higher than those of the constituent elements, indicates a strong bonding between Ni and Al and a corresponding high phase stability with a strong tendency for atomic ordering. This interpretation has been confirmed by quantum-mechanical calculations according to which the strong Ni-Al bonding is of a mixed type, i.e. metallic with contributions of covalent and ionic bonding [56]. Moreover it is confirmed by the highly negative value of enthalpy of formation, as reported in Fig. 2.5 (even lower values are reported in [29], $\Delta H_{form} = -65.7 KJ/mol$):

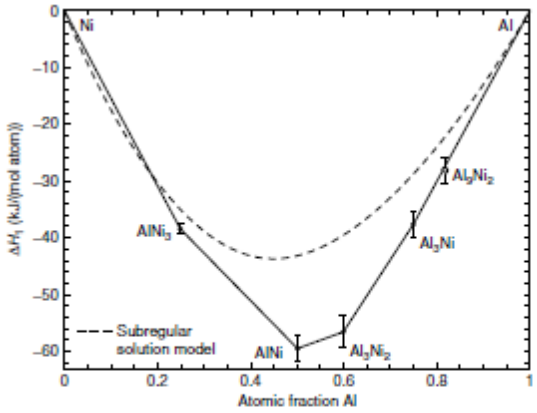

Fig. 2.5: Variation of the enthalpy of formation for the various intermetallic compounds in the binary Ni–Al system.
The broken line corresponds to the enthalpy of mixing of the disordered *fcc* phase, with respect to the pure Ni and Al constituents. Ref: [61].

Indeed NiAl with a stoichiometric composition is highly ordered up to the melting point [56]. Deviations from stoichiometry (resulting in constitutional disorder) are tolerated by NiAl since it is a Berthollide compound [62]: excess Ni atoms replace Al in Al sublattice on the Ni-rich side and vacancies in the Ni sublattice are created on the Al-rich side.

NiAl can be alloyed with further elements in order to form ternary phases with a B2 structure, which is then known as an $L2_0$, or to obtain additional phases in equilibrium with NiAl.

Fe, as well as Co, can substitute for Ni in NiAl completely without affecting the B2 structure, as it is expected in view of the binary transition-metals aluminides B2 phases FeAl and CoAl and as shown in the ternary diagrams AlCoNi [63] and AlFeNi [64] in Fig. 2.6 and Fig. 2.7. These diagrams show the extended B2 phase field and the

respective equilibriums with Ni,Al and Al-rich phases on the Al-rich portion and with disordered *fcc* A1 on the other.

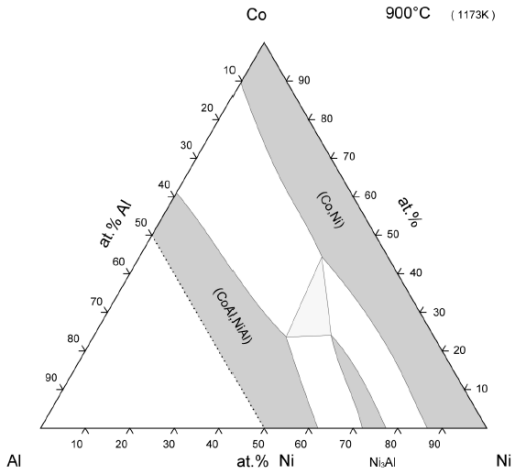

Fig. 2.6: Ternary phase diagram of AlCoNi at 900°C. From ASM APD [56]. Ref: [63]

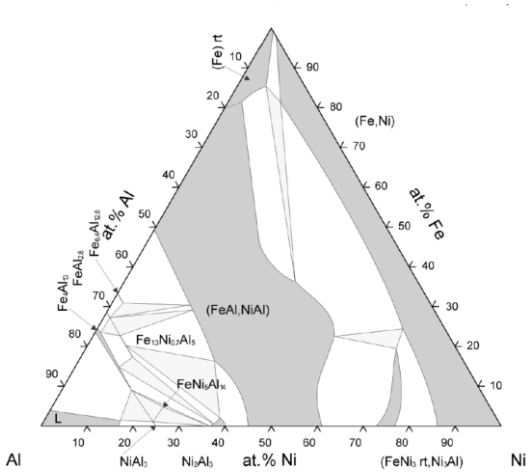

Fig. 2.7: Ternary phase diagram of AlFeNi at 850°C. From ASM APD [56]. Ref: [64]

Cr solubility in B2 structure is quite low. Cr substitutes Ni and Al almost equally in NiAl B2 with slight preference for Al sites, as shown in the AlCrNi ternary diagram at 1025°C [65]. Solubility limit of Cr in NiAl is about 8% at 1027°C [66] but is even lower in FeAl, less than 5% as displayed by AlCrFe diagram in Fig. 2.8. Temperature increases Cr solubility in NiAl B2 [66]. Excess of Cr sets the B2 phase in equilibrium with the solid solution A2.

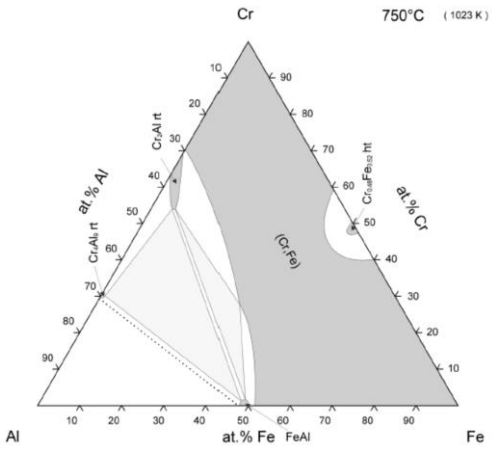

Fig. 2.8: Ternary phase diagram of AlCrFe at 750°C. From ASM APD [56]. Ref: [67]**.**

Finally, the Cu solubility has to be analysed. Cu can be dissolved into the NiAl B2 almost to 30%. Exceeding Cu promotes the equilibrium of NiAl with the $Cu_{0,75}Al_{0,25}$ A2 and the Ni-rich A1. Notably, Cu solubility is higher on the low Ni side of NiAl: indeed Ni vacancies are created in Ni sublattice and they can be occupied by Cu.

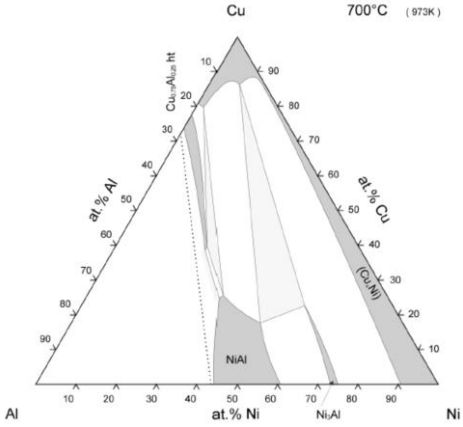

Fig. 2.9: Ternary phase diagram of AlCuNi at 700°C. From ASM APD [56]. Ref: [68]

2.3.2 Ni_3Al $L1_2$

Ni_3Al is the most studied and best known intermetallic because it has been used as a strengthening phase in the Ni-based superalloys [56], [61]. The nickel aluminide Ni_3Al, known as the y' phase, crystallizes with the cubic $L1_2$ structure which results from the *fcc* structure by ordering (Fig. 2.3) with Al atoms at the cube corners and Ni atoms at the centres of the faces. The binary Ni-Al diagram in Fig. 2.4 shows that Ni_3Al melts incongruently at about 1370°C to form liquid Ni-Al and solid A1 (disordered *fcc*) Ni-Al peritectically [56]. In addition, there is a eutectic equilibrium at 1365°C with the B2 phase NiAl and liquid Ni-Al. Ni_3Al is stable, i.e. ordered, up to the melting point, which may, however, only be true near the stoichiometric [61].

Ni_3Al can dissolve further elements, in particular other transition metals. The direction of the Ni_3Al lobes in the isothermal sections of the Al-Ni based ternary diagrams indicates what sites are occupied by the alloying additions.

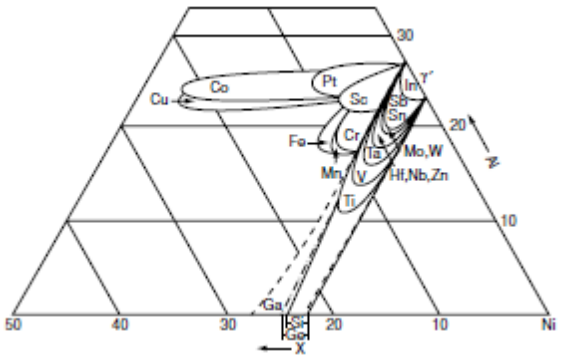

Fig. 2.10: Superimposed ternary phase diagrams Ni–Al–X, illustrating the great effect of X on the extent of the γ' field. Ref. [69]

According to this, Co and Cu occupy Ni sites, whereas Cr and Fe occupy both sites with a slight preference for the Al sites. Indeed elements such as Co and Cu create γ' fields which are parallel to the Ni–X axis on the ternary section, implying a constant Al fraction and providing confirmation of Ni substitution. Moreover Fig. 2.10 shows that Cr and Fe solubility in the $L1_2$ is quite low, around 10%.

The most interesting thing is to point out the condition of precipitation of Ni_3Al γ' phase from an Ni-based A1 phase (known as γ phase), as in superalloys metallurgy [61], [70]. From AlCoNi and AlFeNi diagrams in Fig. 2.6 Fig. 2.7 ([63], [64]) it can be concluded that a minimum amount of Al is required in the γ matrix (around 10%) to promote γ' precipitation (equilibrium γ/γ'). A significant role is played by Cr since it enhances the γ' precipitation at lower amounts of Al, as displayed comparing Fig. 2.11 [71] with Fig. 2.4 especially at temperature below 950°C.

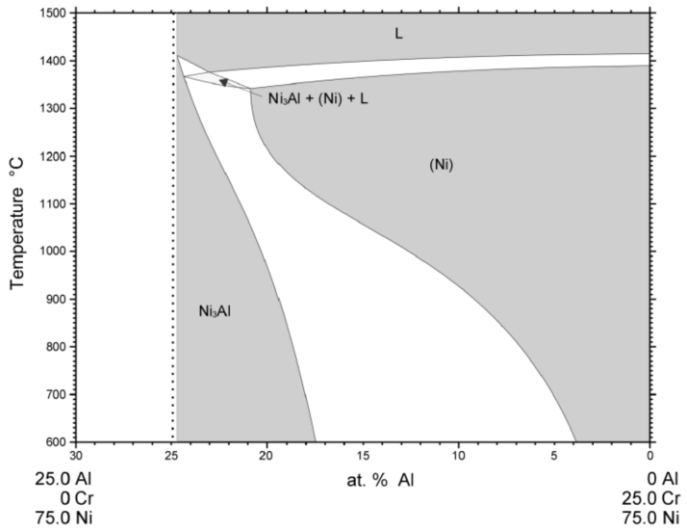

Fig. 2.11: Vertical section of AlCrNi diagram. From ASM APD [56]. Ref: [71]

Precipitation temperature for a given amount of Al can be read from the *solvus* projection of AlCrNi diagram in Fig. 2.12. At temperature below 927°C, Cr increase moves the system from the γ field to the dual phase γ/ γ' field. Alloys of composition consistent with a two-phase γ/γ' microstructure exhibit γ' precipitates which are often cuboidal in form and with nanometric size and their formation cannot be prevented neither by rapid cooling [61], [70].

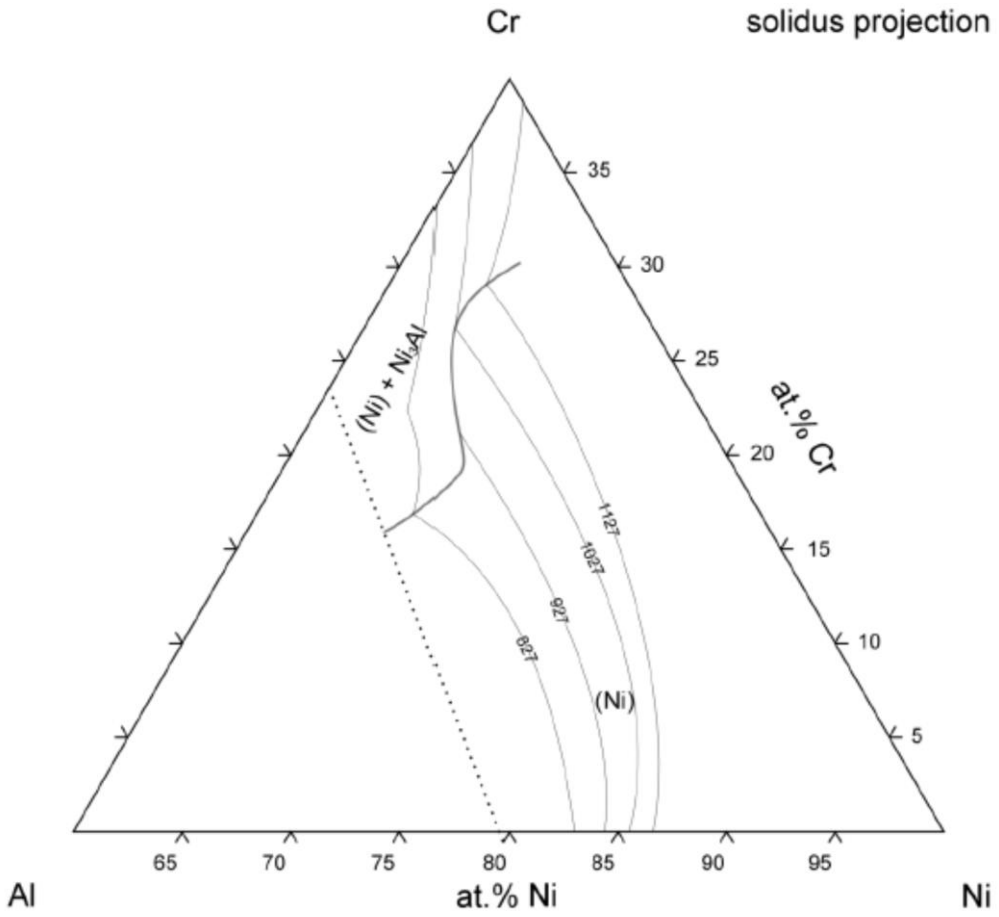

Fig. 2.12: *Solvus* line of γ/γ' in AlCrNi ternary diagram. From ASM APD [56]. Ref: [72]

The lattice parameter of γ' at room temperature is 3.570 Å, which is equivalent to the Al–Al distance and it is only ~1.5% larger than the lattice parameter of pure Ni, which is 3.517 Å [61]. Since the lattice parameters of the A1 γ and $L1_2$ γ' phases are so similar, the XRD diffraction patterns exhibit maxima which are common. For example, the {110}, {200}, {220} reflections are in common, in the contrary the {100}, {210} are due only to γ', as discussed in §2.2.2. The lattice mismatch is even reduced by the addition of some elements. Indeed, the lattice parameters of γ and γ' lattice parameters are linear with the mole fractions of added solutes according to Vegard's law, weighed by Vegard's coefficient [61]. The effect on the lattice parameter (shown in Fig. 2.13) of elements of central part of the transition metals (like Cr, Fe and Co), is null for $L1_2$ but increases the A1 lattice parameter. In this way the lattice parameter of γ gets very close to the one of the $L1_2$ [61], [73].

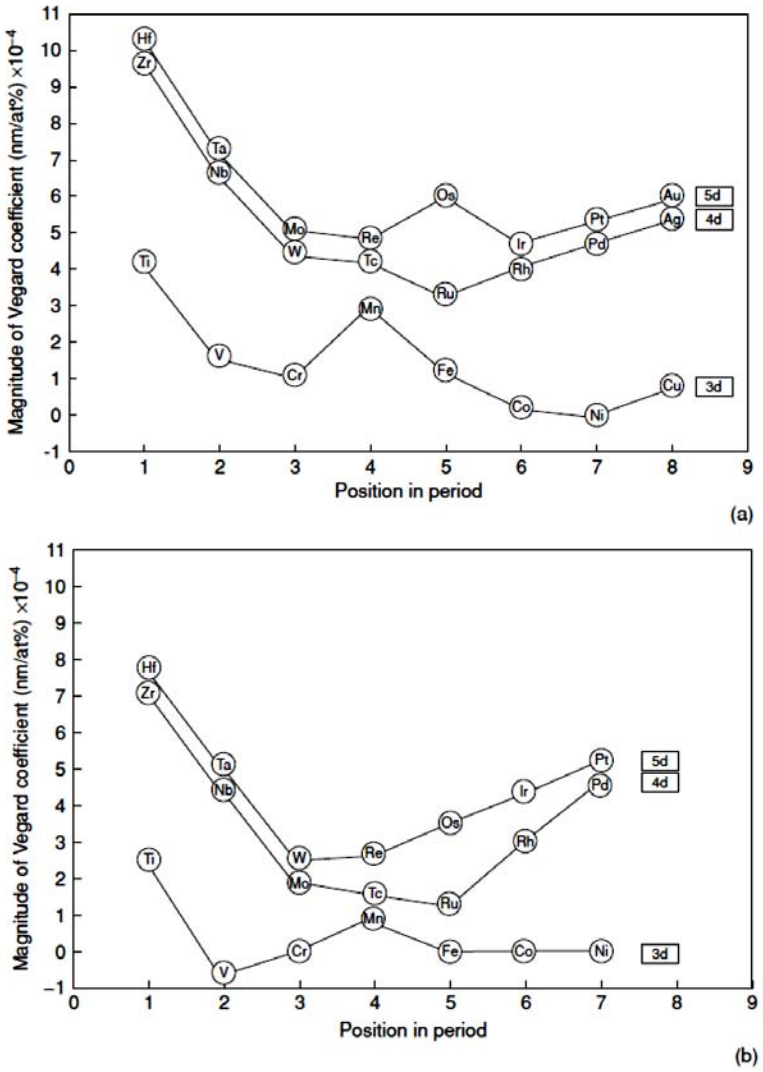

Fig. 2.13: Variation of the Vegard coefficients with position in the transition metals series. (a) for the A1 phase, (b) for the ordered $L1_2$ Ni_3Al phase. From ref. [61]

2.3.3 Sigma phase (σ)

In the AlCrFeCoNiCu system here considered, σ phase can be formed by CrFe and CoCr, as shown in Fig. 2.14. This intermetallic phase is based on a tetragonal unit cell, containing 30 atoms and has ideal stoichiometry $Cr_{0.48}Fe_{0.52}$ (with lattice parameters a=8.790 Å and c=4.559 Å [74]) and $Cr_{0.6}Fe_{0.4}$ (with lattice parameters a=8.81 Å and c=4.56 Å [75]). σ arises mixing two metals with *bcc* structure and with similar atomic radius (deviation around 8%) and examples are found in the metallurgy of duplex steels [76] and Ni-based super alloys [61]. σ is undesirable not only because of the embrittlement effect, but also because of it sequestrates Cr out of the matrix, reducing corrosion resistance [77]. σ formation requires a coordinate movement of a large number

of atoms for each unit cell and this explain why its kinetic of formation is quite low and it cannot form upon cooling [76]. Moreover, CoCrFe σ phase dissolves in the matrix at temperature between 850°C and 985°C, as shown by Elmer *et al.* (2007) [76] and as argued from the binary in Fig. 2.14. Indeed, congruent dissolution of σ phase into the A2 matrix is achieved at the stoichiometric composition at 1282°C for CoCr σ and 840°C for CrFe σ, so that it is then expected that the stability of a mixed σ phase takes place at intermediate values. For non-stoichiometric composition the dissolution temperature range increases and the composition of σ gets closer to the ideal one as temperature increases.

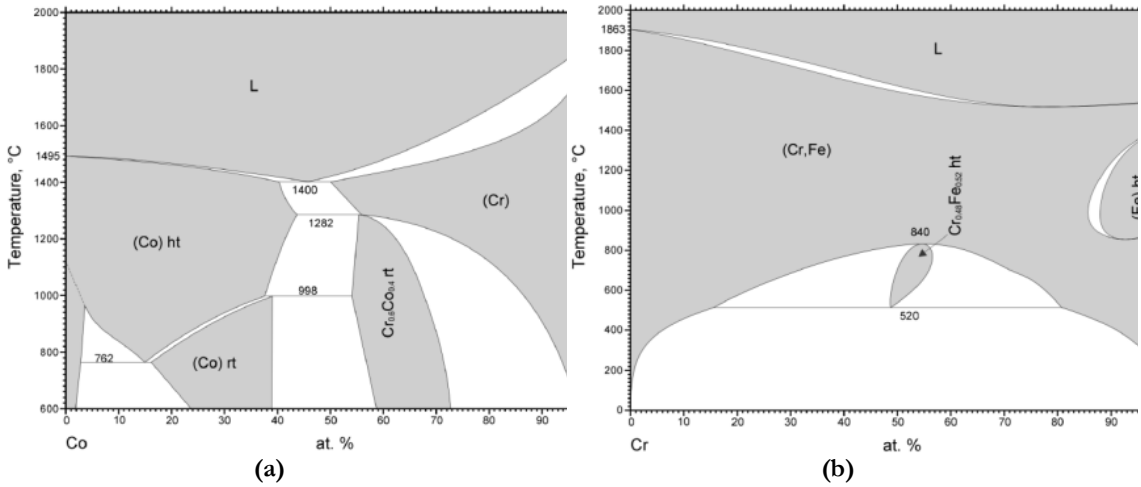

Fig. 2.14: Binary phase diagrams of CoCr (a) and CrFe (b). From ASM APD [56]. Ref. [78], [79]

Important considerations derive from the analysis of solubility limits. First of all, there is no Cu solubility is σ phase, as shown in the CoCrCu phase diagram [80].

The tetragonal σ phase has very little solubility for Al. Indeed, as shown in Fig. 2.8, Al solubility is around 3% and the σ stability field is greatly reduced by the Al presence and it is totally deleted at 900°C [67]. Same effects are played by Al on CoCr σ, as shown on the AlCoCr diagram in Fig. 2.15. In particular, these diagrams show that Al can completely prevent σ formation when Al is more than 40% at 950°C and 30% at 1250°C so that it is clear that Al effect as σ blocker is enhanced by temperature. When Al exceeds its solubility it promotes B2 formation and A1 or A2 solid solution (according to composition).

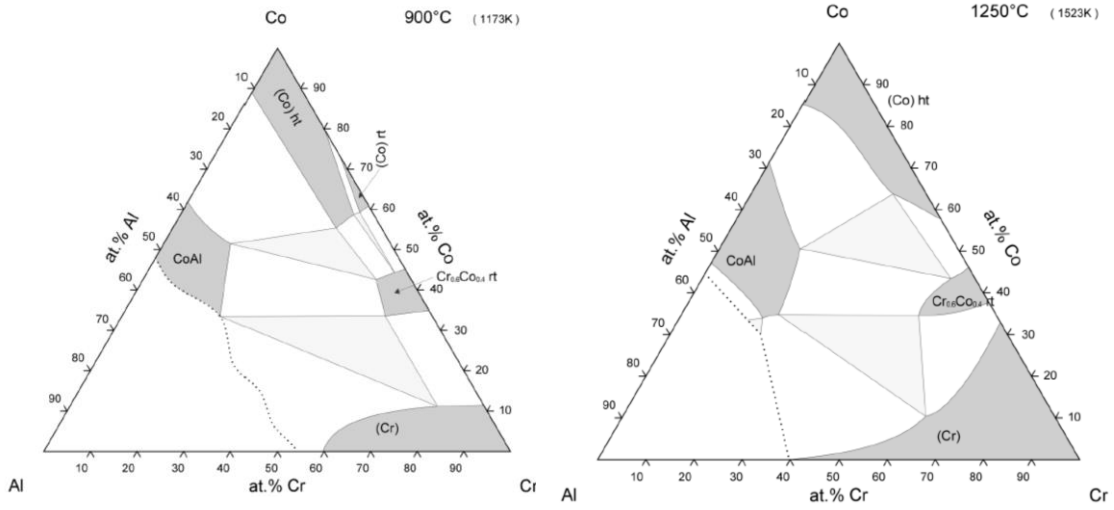

Fig. 2.15: Ternary phase diagram of AlCoCr at 900°C and 1250°C. From ASM APD [56]. Ref: [81]**,** [82] **respectively**

Ni plays a similar role in blocking σ phase. Ni substitutes Co and Fe in σ phase, as evident in the ternary diagrams CrFeNi [83] and CoCrNi [84] and shown in Fig. 2.16 and Fig. 2.17.

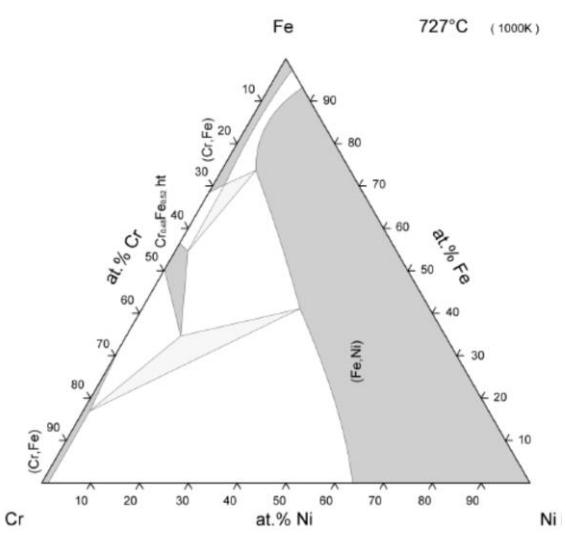

Fig. 2.16: Ternary phase diagram of CrFeNi at 727°C. From ASM APD [56]. Ref: [83]

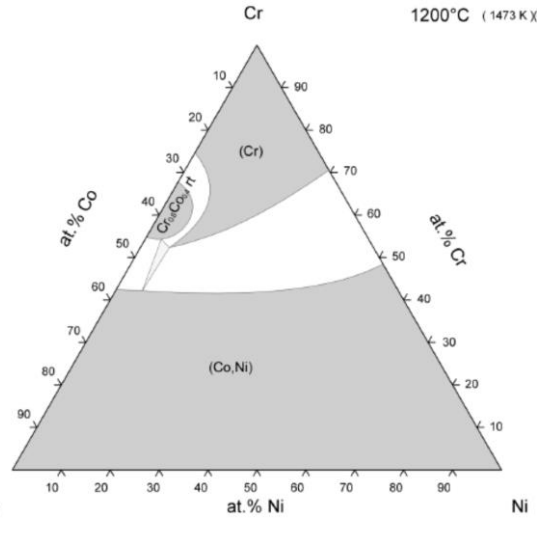

Fig. 2.17: Ternary phase diagram of CoCrNi at 1000°C. From ASM APD [56]. Ref: [84]

Ni solubility in σ is set at around 10% at 727°C in CrFe σ (even lower considering CoCr σ) and Ni can prevent σ formation when added in sufficient amount, roughly 30% for CrFe and much less for CoCr. CoCr σ is then more sensitive to Ni than CrFe. Moreover, excess Ni brings sigma in equilibrium with A1 (A2 only if the Cr the dominant element, over 40%).

Finally also the effect of Fe on σ has to be investigated. Fe solubility in CrCo σ decreases with temperature and it reaches its maximum at 800°C (stoichiometric value) and drops down to 38% at 1000°C and then 10% at 1200°C [85]. Excess Fe leads to equilibrium with A1 or A2 solid solution depending on Cr content in the alloy, with A1 is preferred in the Co-rich side of the diagrams.

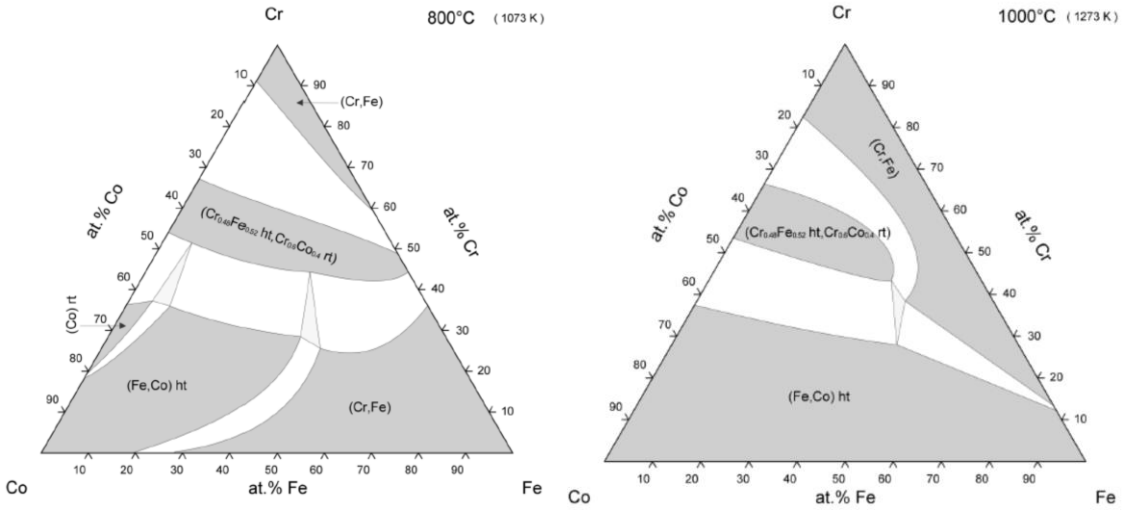

Fig. 2.18: Ternary phase diagram of CoCrFe at 800°C and 1000°C. From ASM APD [56]. Ref: [85]

2.3.4 CrFeCoNi A1

Among all the possible pairs based on Ni (the only one that possess fcc crystal structure at any temperature), Co-Ni exhibits the largest single A1 solid solution field as evident from the diagram in Fig. 2.19 [86] compared with CrNi [87] and FeNi [88].

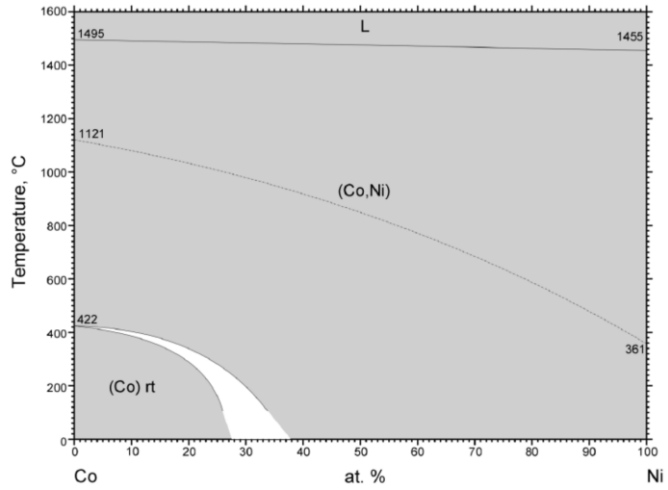

Fig. 2.19: Binary Diagram CoNi. From ASM APD [56]. Ref: [86]

The role of Cr and Fe are to destabilize the A1. Cr is largely dissolved in Co,Ni A1, but when it is over the solubility it promotes the A2 and even σ formation in equilibrium with the A1, as shown in Fig. 2.17. Also Fe is largely soluble in Co,Ni A1 and its solubility increases with temperature, given the allotropic transformation of Fe from *bcc* to *fcc* [89]. Finally, as shown in Fig. 2.18, the A1 is still possible in absence of Ni thanks to role played by Co: indeed the A1 field takes place on the Co-rich side, especially at lower temperature (when Fe is *bcc*).

The strong A1 stabilising role of Ni against Cr is highlighted in the ternary diagram CrFeNi in Fig. 2.16: A1 is stable down to 10% of Ni if Cr does not exceed 25%.

The solubility of Al in the Co,Ni-based A1 will be considered analysing first of all the ternary diagram AlCoNi and then all the ternary containing Al and at least Ni or Co. Starting with the AlCoNi, the solubility limit of Al in the A1 phase is set at 10% at 900°C (Fig. 2.6) and no sensible variations is detected at higher temperature [63]. Excess of Al induces the precipitations of (Ni,Co)Al B2 intermetallic or $L1_2$ in the Ni-rich side of the diagram. The vertical section along the Co:Ni=4:1 line in Fig. 2.20 [90] may be useful to point out the role of Al in determining the crystal structure of the alloy: increasing Al moves the system from an A1 to a dual phase A1+B2 field and finally to a B2 field. This observation confirms the fact that Al promotes B2 formation in HEAs and not A2 (random *bcc*), as stated in §2.1.3.

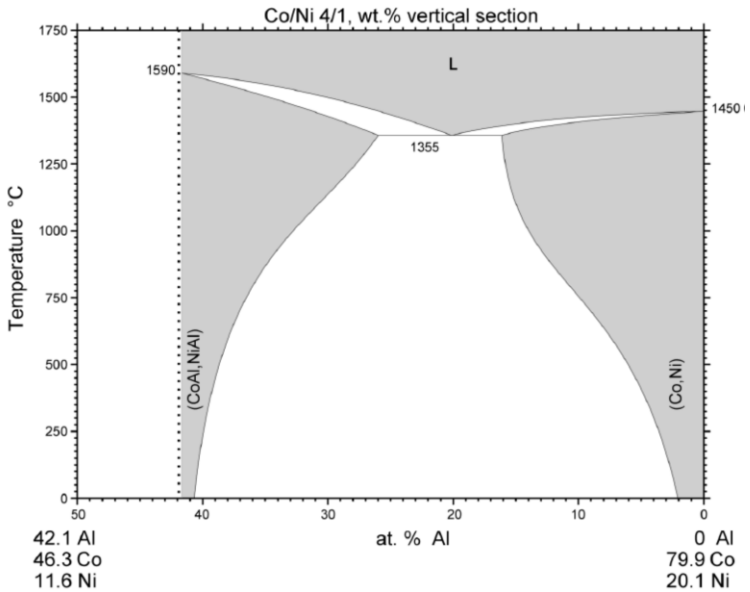

Fig. 2.20: Vertical section of AlCoNi ternary diagram. From ASM APD [56]. Ref: [90]

The AlCrNi at 1427°C in Fig. 2.21(a) shows that at high temperature there is no A1, but the system solidifies as A2 and B2. But at lower temperature (as displayed in Fig. 2.21(b)) the pure A1 is stable only if Al does not exceeds 10-15%, otherwise A1 is set in equilibrium with B2 and A2 or A2 and $L1_2$, depending on Ni content. There is no marked influence of temperature.

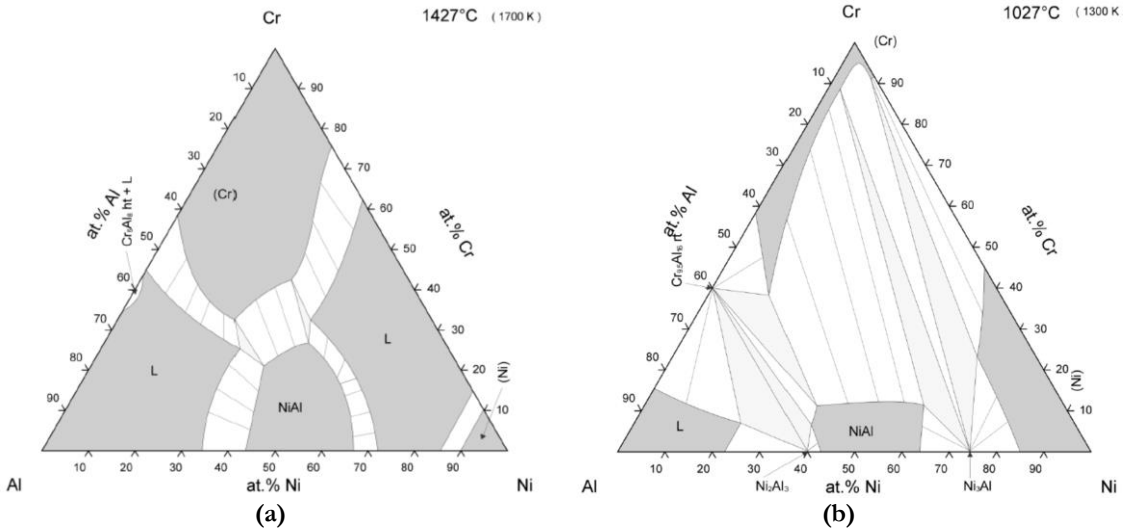

Fig. 2.21: Ternary phase diagram of AlCrNi at 1427°C (a) and at 1027°C (b). From ASM APD [56]. Ref:[66]

In the AlFeNi system at 850°C in Fig. 2.7 [64], Al is soluble up to 7% when Ni is over 10% (otherwise A2 may be present). Solubility limit slightly increases with temperature up to 10% [64]. Excess Al establishes the equilibrium between A1 and B2.

From Fig. 2.15 it can be seen that in the AlCoCr system, Al solubility in A1 is around 10% at 900°C and temperature does not alter it in a significant way. Excess of Al provokes σ CoAl B2 precipitation, whereas excess of Cr leads to σ and A2.

Finally, solubility of Al in the A1 of the AlCoFe system is around 10% at 1000°C and it gets lower decreasing the temperature (5% at 650°C) [91], [92]. Once again, Al excess establishes equilibrium between A1 and B2 and A2.

Obviously, the AlCrFe (without both Ni an Co), shown in Fig. 2.8, does not show any A1 at any temperature: no stable A1 is possible since all the three constituents are *bcc* structure.

The solubility of Cu in Co,Ni-based A1 has been treated as for the Al one. Preliminarily, it has to be pointed out that low solubility is expected. Indeed Fig. 2.22(a) displays the CrCu system exhibits total immiscibility at the solid state [93] and also Co and Fe show

large miscibility gap with Cu [94], [95]. This is in agreement with the highly positive values of mixing enthalpy, as stated in §2.1.3. On the contrary Ni has full miscibility with Cu (Fig. 2.22(b) [60]). This means that Ni will play the roles of both A1 stabiliser and Cu solvent.

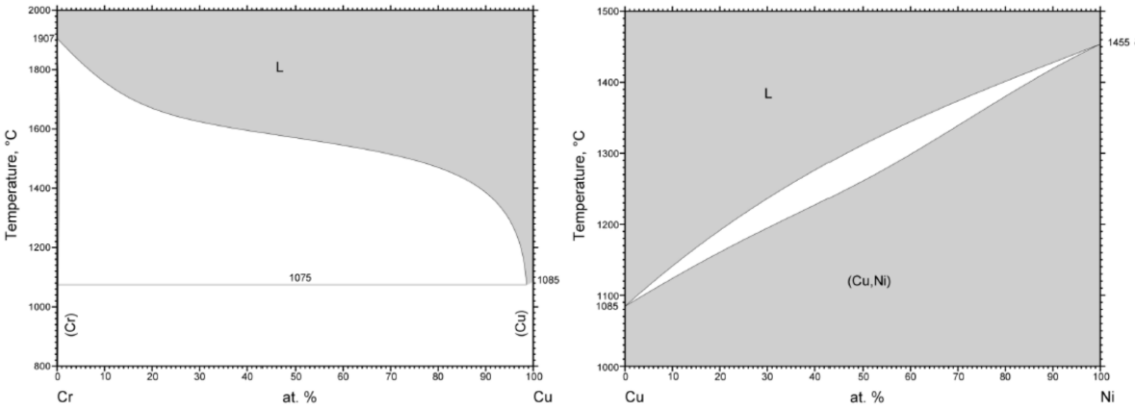

Fig. 2.22: Binary phase diagrams of CrCu (a) and CuNi (b). From ASM APD [56]. Ref. [60], [93] **respectively**

From these binary diagrams it derives that the A1 in CrCoCu [80] has no solubility for Cu at all, and CrCuFe [96] and CoCuFe [94] has a little solubility for Cu, increased by temperature. On the contrary, Fig. 2.23 shows that Cu solubility is greatly enhanced by the presence of Ni. Indeed in the CuFeNi [97] and CoCuNi [98] systems, the solubility of Cu in A1 can be as high as 35-40% in the Ni-rich portion of the diagram (Ni>45%). On the other hand, the Cr has a much lower compatibility with Cu and phase segregation is avoided only in the very Ni-rich portion, as demonstrated by CrCuNi [99] in Fig. 2.24.

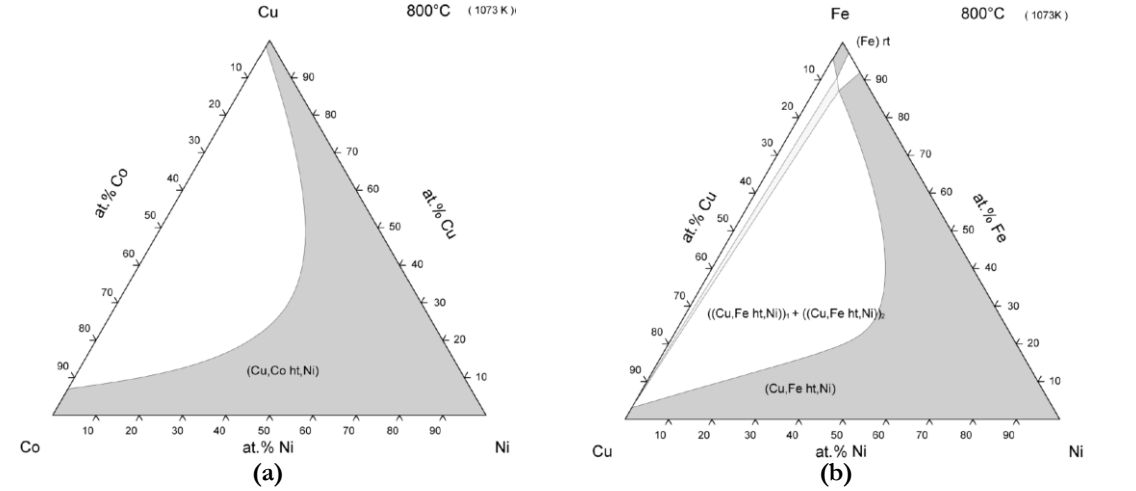

Fig. 2.23: Ternary phase diagrams of CoCuNi (a) and CuFeNi (b). From ASM APD [56]. Ref. [97], [98] **respectively**

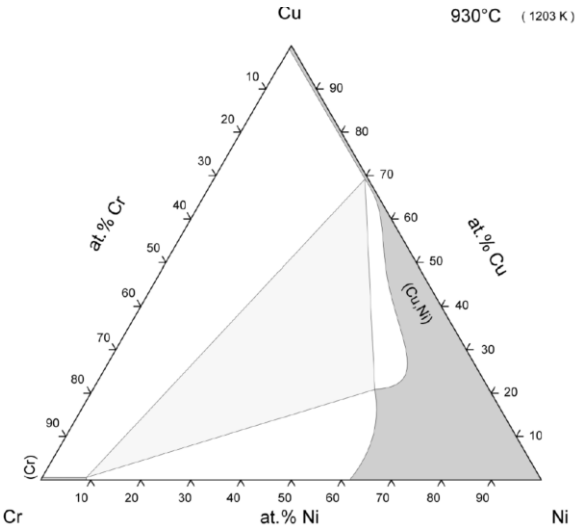

Fig. 2.24: Ternary phase diagram of CrCuNi at 930°. From ASM APD [56]. Ref: [99]

In conclusion, A1 solid solution based on Co,Ni is stabilised against Cr by Ni that acts as Cu solvent and compatibilizer between Cr,Co,Fe and Cu. Solubility of Al is limited at values close to 10% and excess of Al induces B2 formation, whereas Cr excess promotes σ and A2.

2.3.5 CrFe A2

As shown in Fig. 2.14(a) and (b), Cr and Fe exhibit large miscibility at high temperature contrary to Cr and Co. For this reason an A2 solid solution with Cr as dominant element as Fe and Co as solutes in large amounts has to be considered based on the Cr,Fe A2 solid solution.

Co solubility in the Cr,Fe A2 is shown in Fig. 2.18: it increases with temperature from 10% at 800°C up to almost 20% at 1000°C and Co excess prevalently provokes σ formation [85].

The solubility of other elements is described considering the ternary diagrams. Ni solubility in the Cr,Fe A2 is significantly low (<5%) as evident in the ternary diagram CrFeNi in Fig. 2.16 and it is slightly reduced as temperature increases [83]. This result is expected considering the different crystal structure of Cr,Fe (*bcc*) and Ni (*fcc*): indeed Ni establishes the equilibrium A2 + A1.

Contrarily to the A1 phase described in §2.3.4, Al solubility is much greater in the A2 as shown in the AlCrFe diagram in Fig. 2.8, where precipitation of secondary phases are

enhanced only if Al exceeds 30%. However, the presence of Ni greatly promotes the precipitations of NiAl B2 (as displayed in Fig. 2.21(b) in the AlCrNi system) so that Al is sequestrated by Ni thanks to the highly negative enthalpy of formation of NiAl (§2.3.1).

Finally, the solubility of Cu in CrFe is almost negligible [96].

2.3.6 $Cu_{0.75}Al_{0.25}$ A2

The binary diagram AlCu on the Cu rich side exhibits several intermetallics compounds and one solid solution with A2 structure stable at higher temperature as $Cu_{0.75}Al_{0.25}$, shown in Fig. 2.25 [100]. This phase is particularly important and studied in shape-memory alloys since it is the mother phase that originates the martensitic phase [101]. Contrary to its identification, it is not stoichiometric intermetallic but a solid solution that congruently melts at 1050°C when Cu:Al=75:25 [102] and it is stable only at high temperature above 560°C.

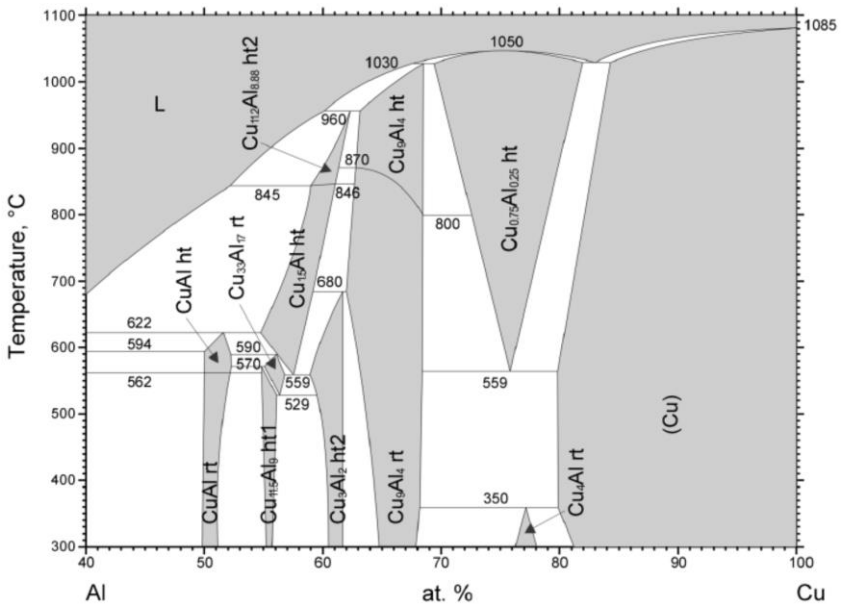

Fig. 2.25: Binary Diagram AlCu. From ASM APD [56]. Ref: [100]

The solubility limits of Co, Cr Fe is almost negligible in this phases as visible from the ternary diagrams AlCoCu [103], AlCrCu [104] and AlCuFe [105], inducing segregation between the Cu rich phase and Co,Cr,Fe one.

On the contrary, the solubility of Ni is much higher as evident in the AlcuNi ternary diagram in Fig. 2.9 [68] where it is possible to see that Ni substitutes Cu up to 30% at

700°C. According to the binary diagram AlCu, $Cu_{0.75}Al_{0.25}$ disappears at temperature below 600°C.

2.3.7 CuNi A1

As stated in §2.3.4, among the other elements in AlCrCoFeNiCu alloys, Ni is the only one able to form extended solid solution with Cu (Fig. 2.22).

Cr solubility in Cu,Ni A1 is basically negligible if Ni amount is below 35-40%, as proved by the ternary diagram CrCuNi in Fig. 2.24. Solubility of Co and Fe are greatly enhanced increasing the amount of Ni and they are significant only in the Ni-rich side of the diagram. As described, §2.3.4, Ni plays a compatibilizer role in between Cu and Co,Fe and even Cr.

The AlCuNi diagram in Fig. 2.9 [68] shows that Al solubility in Cu,Ni A1 decreases as Cu amount increase and it is particularly low (<5%) when Cu is over 65%. Al solubility in Cu,Ni A1 increases over 10% at higher temperature (900°C [68]). Excess of Al promotes the equilibrium with Ni_3Al $L1_2$ and NiAl B2. The effect of Al on the Cu-rich A1 is well highlighted in the vertical section at Ni=10% of the ternary diagram AlCuNi shown in Fig. 2.26 [60]. Increasing Al, the system shifts from a single Cu,Ni A1 field to a duplex field A1+ Ni_3Al $L1_2$ and then three phase field $Cu_{0.75}Al_{0.25}$ A2 +NiAl B2 + Cu,Ni A1 and finally again to a duplex field $Cu_{0.75}Al_{0.25}$ A2 +NiAl B2.

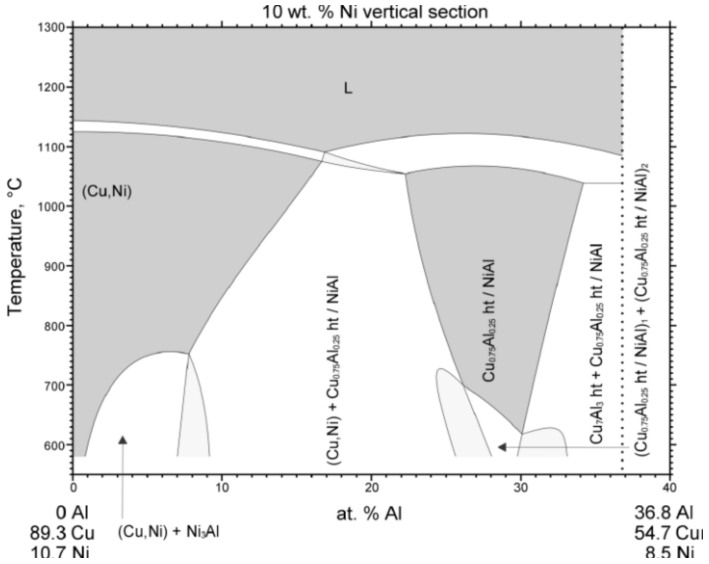

Fig. 2.26: Vertical Section of the ternary diagram AlCuNi. From ASM APD [56]. Ref: [60]

3. MATERIALS AND METHODS

3.1 ALLOY PREPARATION AND HEAT TREATMENT

Three alloys of the system $Al_xCrFeCoNiCu$ were investigated with nominal at.% composition reported in Table 3.1.

Identification	Formula	Al	Cr	Fe	Co	Ni	Cu
HEA5	$Al_{0.5}CrFeCoNiCu$	9.0	18.2	18.2	18.2	18.2	18.2
HEA6	AlCrFeCoNiCu	16.7	16.7	16.7	16.7	16.7	16.7
HEA7	$Al_3CrFeCoNiCu$	37.5	12.5	12.5	12.5	12.5	12.5

Table 3.1: Nominal at.% composition of the alloys under investigation

The alloy preparation and heat treatment was performed by Dr. Jones N. (Rolls-Royce UTC, Department of Materials Science and Metallurgy – University of Cambridge, UK) to perform investigation on the HEA5 [13]. 40g ingots of each alloy were prepared via arc melting in an inert atmosphere from elemental metals with purity of 99.95% or higher. To achieve homogeneity, the alloys were inverted and re-melted five times and then air cooled.

Short section, about 10mm long, were cut from each cast ingot, encapsulated in evacuated argon backfilled quartz ampules and aged for 1000 hours at 700°C, 850°C and 1000°C. After the heat treatment the samples have been water quenched in order to freeze the high temperature microstructure to the room temperature. The possibility to freeze the high temperature microstructure down to room temperature is a premise of several other works [12]–[14] and it is supported by the hypothesis of the advocated sluggish diffusion in the HEAs, as argued in §2.1.1 [1].

3.2 SEM MICROGRAPHIC EXAMINATION

The metallographic preparation started with sectioning thin slices (about 3mm thick) transversally to the ingot axis using a precision table top cut-off machine for precise and deformation-free cutting (Struers Accutom-5). One slice was cut for each heat treatment and as cast condition for each alloy. Since some of the samples (especially the ones

treated at 700°C and 850°C and HEA7 samples) were particularly brittle and exhibit cracks after quenching, the cutting step was performed with low feed speed (0.008-0.015 mm/s) and reduced force limit.

Each thin slice was then mounted in epoxy resin by a Buehler Metaserv automatic mounting press and grinded and polished on an automatic grinder Struers Pedemax-2 using the following steps:

1. P600 SiC abrasive paper (standard grit: 400);
2. P1200 SiC abrasive paper (standard grit: 600);
3. P2400 SiC abrasive paper (standard grit: 800);
4. P4000 SiC abrasive paper (standard grit: 1200);
5. Polishing with napped cloth and colloidal Silica

Microstructural characterisation was carried out using backscattered electron imaging (BSEI) at 15kV accelerating voltage in a JEOL 5800 LV Scanning Electron Microscope equipped with fully integrated digital acquisition and Oxford Instruments energy dispersive X-ray (EDX) spectroscopy system. Images and elemental maps were acquired ad treated by the software Oxford Instruments INCA Microanalysis Suite 4.15. An additional micrographic characterisation on the FEI Helios NanoLab Dual Beam microscope was performed on the HEA6 700°C and 850°C in order to discern secondary phases.

3.3 EDX MICROANALYSIS

EDX microanalysis was performed by Oxford Instruments energy dispersive X-ray (EDX) spectroscopy system in the JEOL 5800 LV Scanning Electron Microscope. Phase compositions were determined by averaging five individual point analyses and the so obtained standard deviations were within 1 at.%. Only the analysis of the smallest phases, below the EDX probe spatial resolution (≈1μm), exhibits standard deviation over 1 at.%: in these cases a scan of an area containing, in similar proportion, the unknown small phase and a phase with known composition was performed in order to have an indication about the likely composition. The bulk composition of each sample was assessed by five large area (≈500x500 μm) executed at low magnification, obtaining values within 1at.% in respect to the nominal composition.

3.4 X-RAY DIFFRACTION (XRD)

Crystallographic information was obtained via X-ray diffraction using a Philips PW1050 diffractometer Bragg Brentano parafocusing geometry, reflection mode with CuKα radiation equipped with graphite beam monochromator. The sample preparation consisted in grinding slices of each sample with a P600 SiC abrasive paper. The slits configuration used was:

1. Divergence slit: ½°
2. Receiving slit: 0.2mm
3. Anti-scatter slit: ½°

Data were collected via PANalytical X'PERT data collector software in a 2θ range between 20° and 120°C with step size of 0.04° and scan step time of 20s (14h for the complete scan). The generator settings used was: 40 mA current, 40 kV voltage.

The preliminary phase identification was performed via PANalytical HighScore Plus software for peak refining and phase identification by comparison within the ICDD (International Centre for Diffraction Data) database.

The calculation of the lattice parameter was performed in a Microsoft Excel spreadsheet since the detected structures were quite simple (cubic or tetragonal). For each phase detected with HighScore Plus a first lattice parameter estimation was performed using just one peak with known Miller's indexes $\{hkl\}$ by the use of Eq. 3.1 derived by Bragg's Law and calculating the lattice parameter by the inverse formula in Eq. 3.2, i.e. the relationship between the d plane spacing and the cell parameters a, b, c for orthorhombic systems (with $a = b = c$ in a cubic system, $a = b$ in a tetragonal system) [57]. Then a pattern of vertical lines was created starting from the list of $\{hkl\}$ plane families that give reflection for that structure and calculating the respective peak position by the use of the estimated lattice parameter and the use of the direct Eq. 3.2 and then the inverse form of Eq. 3.1, finding the estimated 2θ position for each $\{hkl\}$ of reflective planes. The last step was to superimpose the pattern of vertical lines to the experimental diffractogram and adjusting the value of lattice parameter in order to achieve the best matching. This procedure does not allow to attain an extremely precise measure but it was sufficient for the aim of this work. Moreover the matching between experimental

diffractograms and the vertical line pattern was very precise given the simple crystal structure detected.

$$d = \frac{\lambda}{2\sin\vartheta};\ \lambda = 1.5406\text{Å} \qquad \textbf{Eq. 3.1}$$

$$\frac{1}{d^2} = \frac{h^2}{a^2} + \frac{k^2}{b^2} + \frac{l^2}{c^2} \qquad \textbf{Eq. 3.2}$$

Finally, for peaks that exhibits shoulder two to phase with similar lattice parameters la peak fitting was performed with Origin 8.5 using Gaussian peaks in order to obtain information about the area subtended by each of the two peaks.

3.5 DIFFERENTIAL SCANNING CALORIMETRY (DSC)

Differential scanning calorimetry was performed between 50°C and 1450°C under flowing of Argon using a Nietzche 404 high temperature calorimeter at heating and cooling rate of 10°C/min and holding time of 15 min at 50°C before heating, at 1450°C and at 50°C after cooling.

4. RESULTS AND DISCUSSION

This chapter exposes all the experimental data collected during this work through the methods described in the §0 and the respective discussion on the basis of the literature review in §2. The chapter will be divided on the alloy-composition basis, so that for each analysed alloy the experimental results and then the appropriate discussion will be presented. This exposition order will help the reader to keep in mind the experimental evidences in order to have an easier insight into the discussion part. To underline the effect of heat treatment temperature, for each test method the results will be presented with the following order:

- As Cast condition
- Aged at 1000°C – 1000h
- Aged at 800°C – 1000h
- Aged at 700°C – 1000h

The discussion part will take in account each one the microconstituents in order to explain the evolution through the different heat treatment and accordingly to literature previous works.

A summarised résumé will be presented in §5 to provide a synthesis of the whole project and of what the findings here debated reveal about the purpose of the study.

4.1 HEA5 - RESULTS

The High Entropy Alloy no. 5 (HEA5) is the low Al alloy among the three alloys analysed. Its formula can be expressed like Al0.5CrFeCoNiCu and its atomic composition is shown in Table 4.1. As for all the examined alloys, HEA5 has been heat treated as described in §3.1.

at.%	Al	Cr	Fe	Co	Ni	Cu
HEA5	9.0	18.2	18.2	18.2	18.2	18.2

Table 4.1: Nominal Chemical Composition of HEA5 (% at.)

4.1.1 Micrographs

AS CAST CONDITION

The micrographs of the as cast HEA5 in Fig. 4.9-(A) reveals two main regions:

1. Grey dendritic region (DR)
2. White interdendritic region (ID)

The preliminary analysis shows that the dendritic phase is the major one and, thanks to the higher magnification in Fig. 4.9-(B), that a minor compositional contrast is evident in the DR. Images in Fig. 4.9-(C) to (H) display the EDX maps of each element in the alloy. Especially through images (D), (E), (F) and (G), one can discern that the composition contrast is due to the dendrites coring occurred during solidification because of the lack of back-diffusion. Moreover the EDX maps indicate that the DR is Cr,Fe,Co,Ni-rich and the ID is Cu-rich, dissolving some Al and Ni but greatly depleted in Cr,Fe,Co. Cu segregation has then occurred as observed in other works and described in §2.1.3.

1000°C / 1000H AGED

This sample appears extremely similar to the one in the as cast condition, as confirmed by the confrontation between Fig. 4.9-(A) and Fig. 4.11-(B) where only two phases are shown (again DR and ID). The higher magnification in Fig. 4.11-(B) does not exhibit coring phenomenon anymore. Moreover the interfaces are definitely sharper, as confirmed also by the Fig. 4.11-(C) to (G). The long heat treatment at very high temperature allows the diffusion to occur on a longer scale, enhancing the net separation between the two phases. The dendritic phase still appears to be the major one. Remarkably, the two phases are still markedly separated even if this heat treatment was performed in proximity of liquidus temperature: this means that phase separation due to Cu segregation cannot be eliminated.

Like in the as cast condition, the EDX maps (in Fig. 4.11-(C) to (H)) allow to infer that the DR is Cr,Fe,Co,Ni-rich and the ID is Cu-rich, dissolving some amounts of Al and a little of Ni but absolutely depleted in Cr,Fe,Co (proof of the enhanced phase separation).

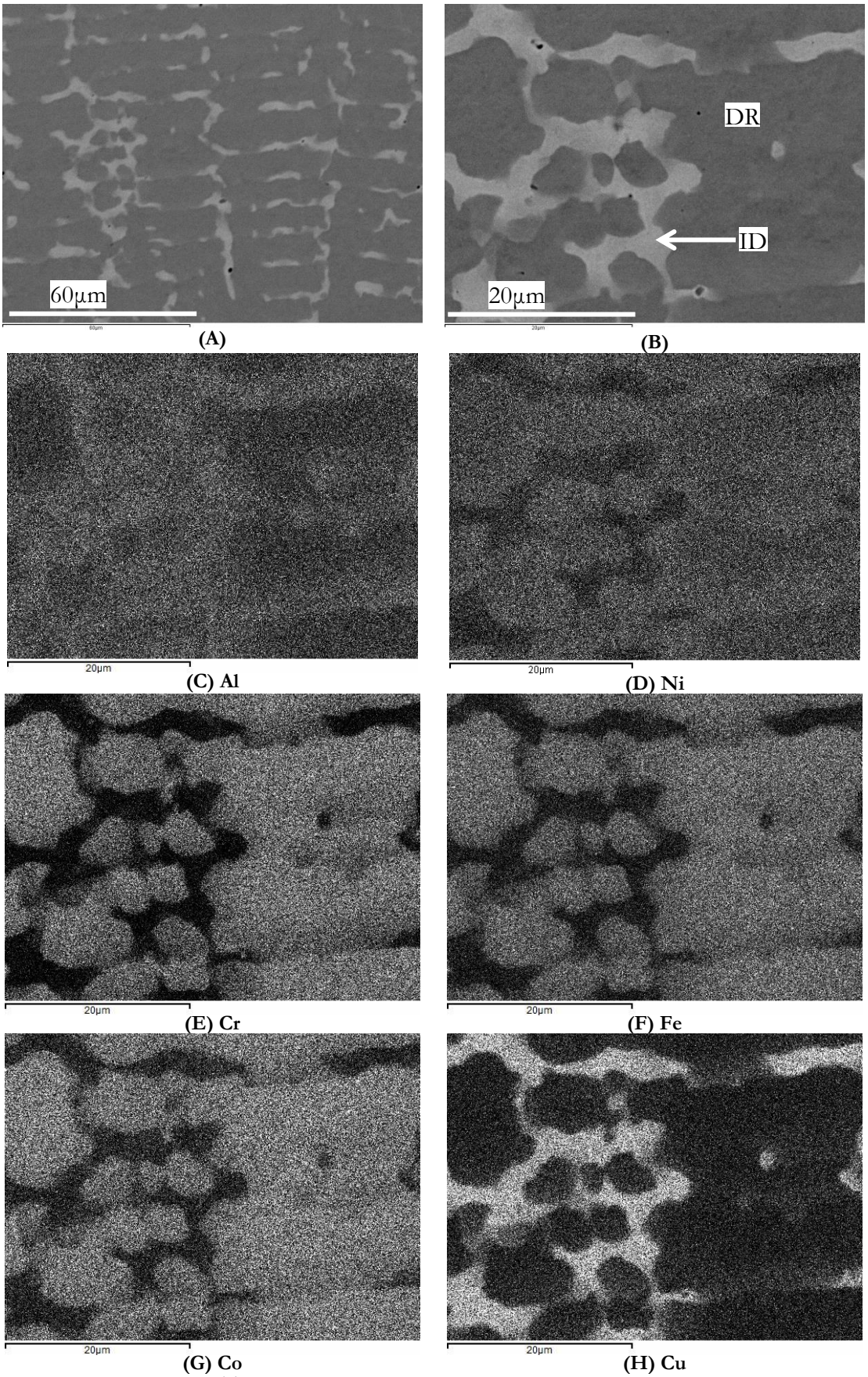

(A) **(B)**

(C) Al **(D) Ni**

(E) Cr **(F) Fe**

(G) Co **(H) Cu**

Fig. 4.1: HEA5 – AS CAST micrographs.
(A): lower magnification; (B): higher magnification; (C-H): EDX elemental maps from image (B)

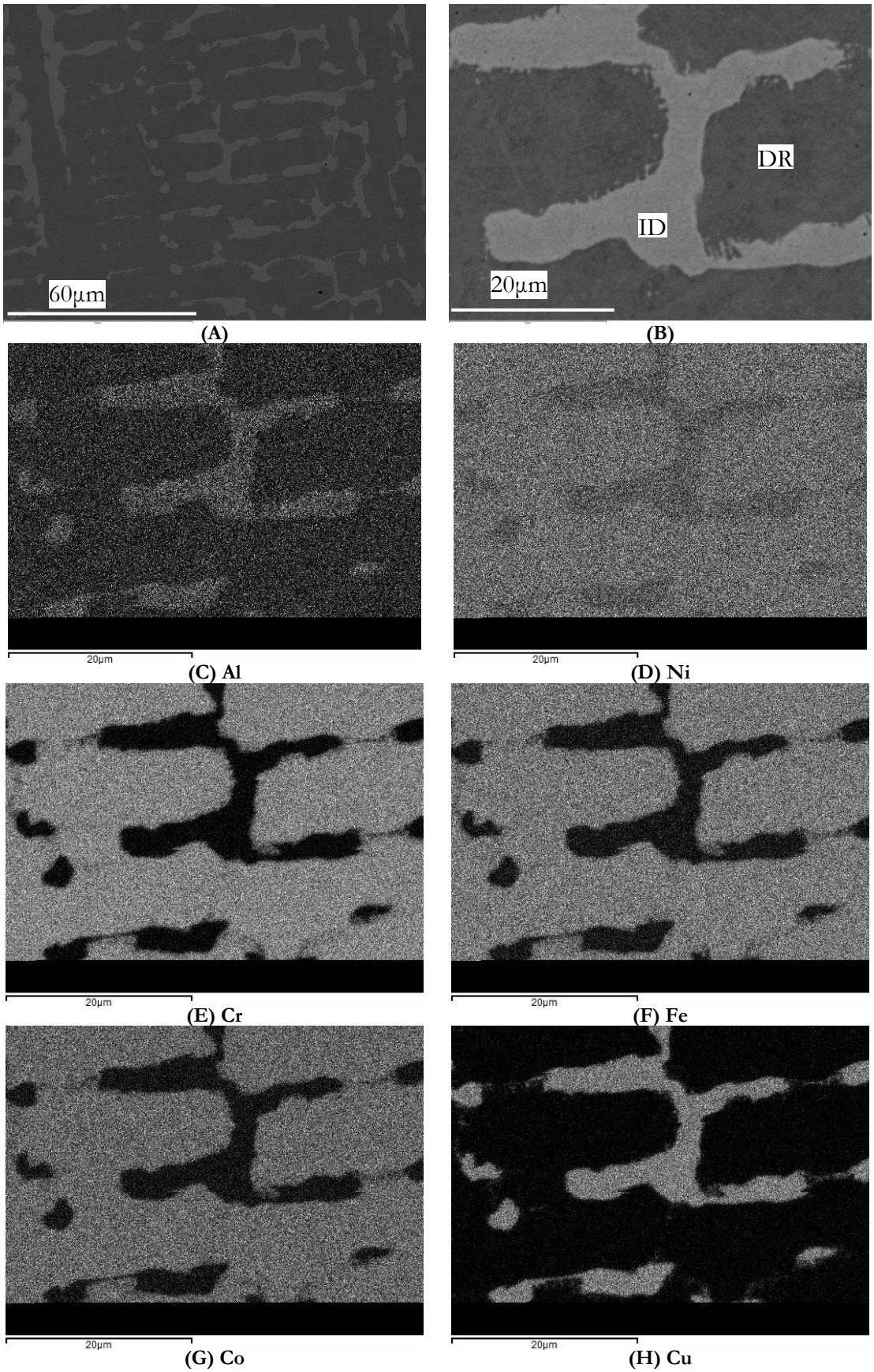

(A) **(B)**

(C) Al **(D) Ni**

(E) Cr **(F) Fe**

(G) Co **(H) Cu**

Fig. 4.2: HEA5 – 1000°C /1000H. micrographs.
(A): lower magnification; (B): higher magnification; (C-H): EDX elemental maps from image (B)

850°C / 1000H AGED

Fig. 4.3-(A) and its higher magnification (B) show the presence of at least six main features, with four new regions in respect to previously discussed samples:

1. Grey dendritic region (DR)
2. Small white precipitates within the DR (DPR)
3. White interdendritic region (ID)
4. Globular dark grey precipitates (PR1)
5. Needle-like dark precipitates (PR2)
6. Light grey globular precipitates (PR3)

The dendritic phase still appears to be the major one. Moreover all the precipitates heterogeneously nucleate from the DR-ID boundaries. The needle-like precipitates PR2s, especially the smaller ones, look to be arranged along two preferential directions inclined of ±45° in respect to the ID. This is explained considering that precipitates within the grains need to be accommodated in a structure with a regular atoms packaging: for this reason the growth of precipitates takes place along preferential directions in order to minimize the lattice stresses due to lattice parameter mismatch. On the contrary, along the grain boundaries, the disorder allows a globular growth since atoms packaging is not regular.

The EDX maps collected in Fig. 4.3-(C) to (H) highlight that:

1. The DR is Cr,Fe,Co,Ni-rich;
2. The DPR are too small to be compositionally resolved;
3. The ID is Cu-rich;
4. The PR1 are Ni,Al-rich;
5. The PR2 are Ni,Al-rich;
6. The PR3 are Cr-rich.

One can observe (considering especially Al and Ni maps) the there is no evidence of compositional differences between PR1 and PR2. This suggests they may be the same phase.

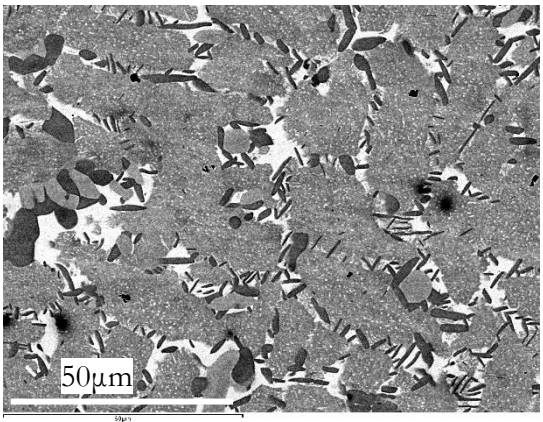

(A)

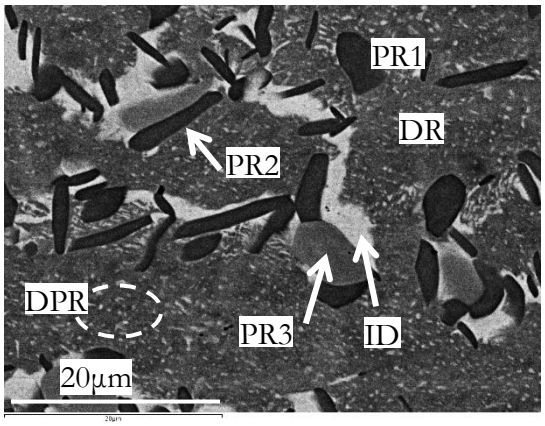

(B)

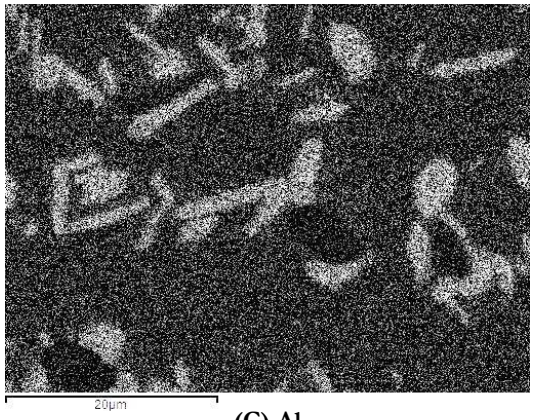

(C) Al

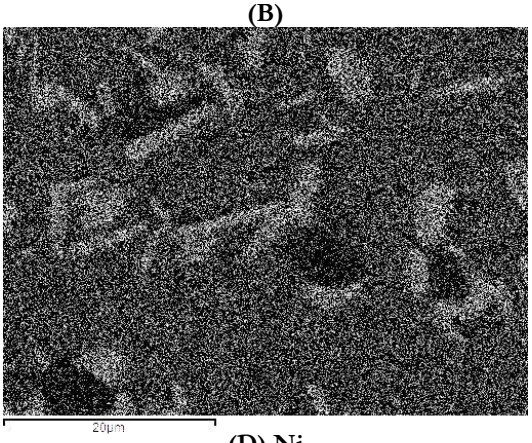

(D) Ni

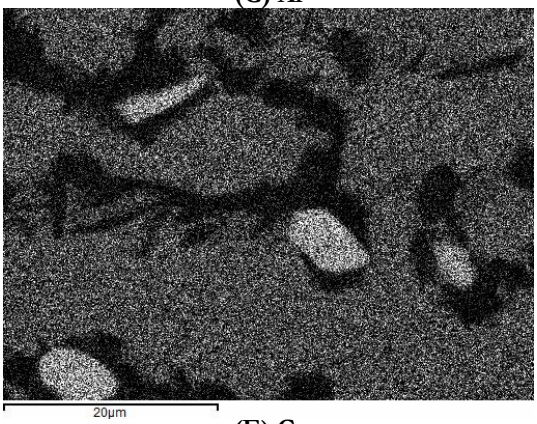

(E) Cr

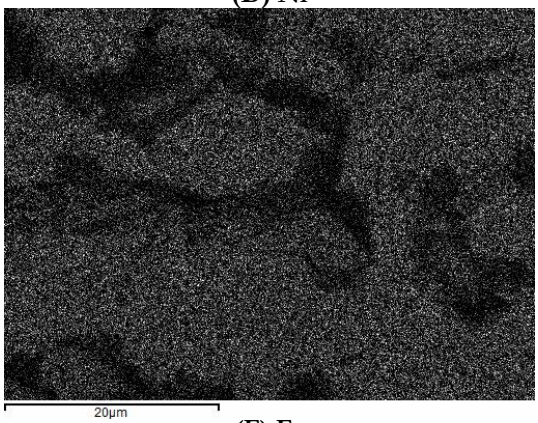

(F) Fe

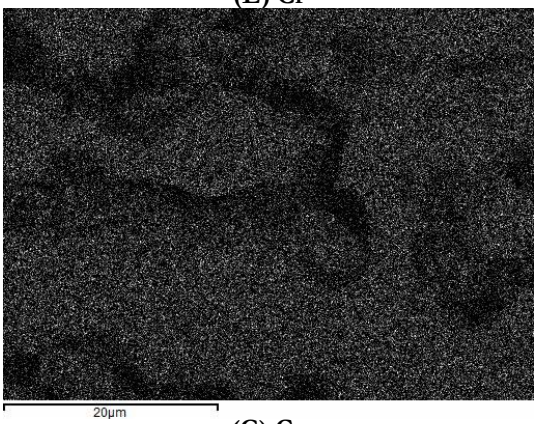

(G) Co

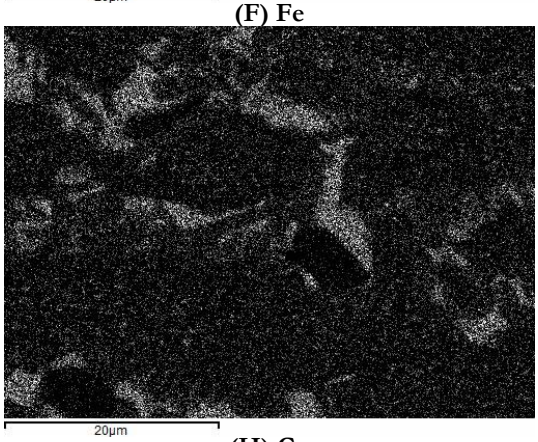

(H) Cu

Fig. 4.3: HEA5 – 850°C /1000H micrographs.
(A): lower magnification; (B): higher magnification; (C-H): EDX elemental maps from image (B).

700°C / 1000H AGED

The 700°C aged sample is quite similar to the 850°C with the exception that the white DPR are no longer visible, as displayed in the Fig. 4.4-(A) and (B):

1. Grey dendritic region (DR)
2. White interdendritic region (ID)
3. Globular dark grey precipitates (PR1)
4. Needle-like dark precipitates (PR2)
5. Light grey globular precipitates (PR3)

Also in this sample the dendritic phase is the major one and the precipitates still appear to be heterogeneously nucleated from the DR-ID boundaries, even if some needle-like PR2s are detected also in the bulk DR. Comparing with the 850°C treated sample, the needle-like PR2s are smaller and their preferential orientation is even more evident in this sample (particularly considering the lower magnification image in (A)).

The EDX maps (Fig. 4.4-(C) to (H)) underline that:

1. The DR is Cr,Fe,Co,Ni-rich;
2. The ID is Cu-rich;
3. The PR1 are Ni,Al-rich;
4. The acicular PR2 are too small to resolve the composition;
5. The PR3 are Cr-rich.

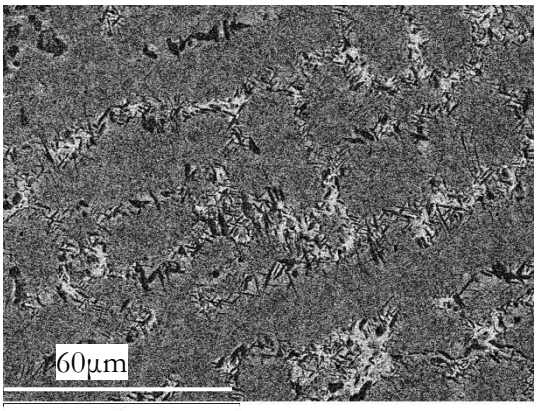

(A)

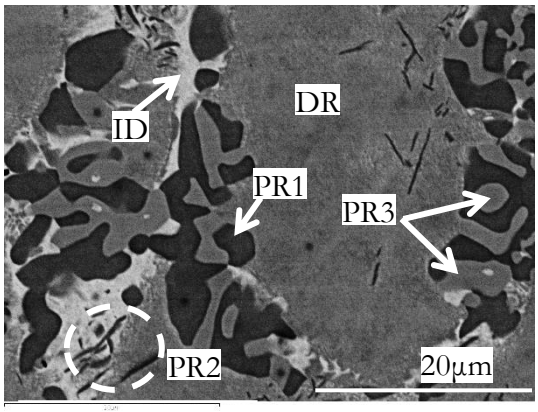

(B)

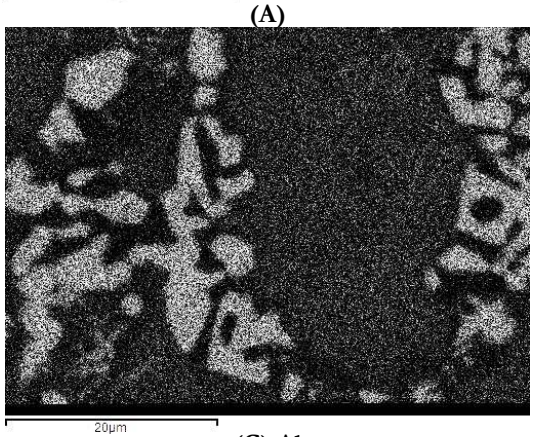

(C) Al

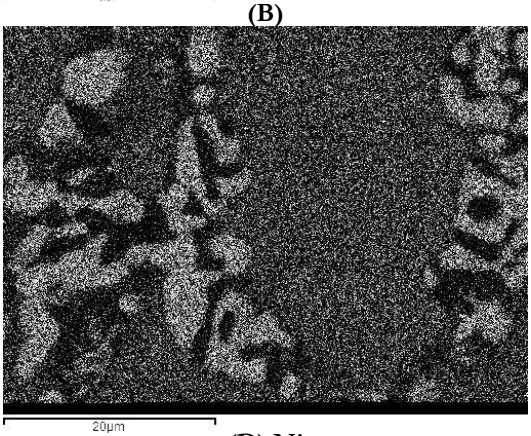

(D) Ni

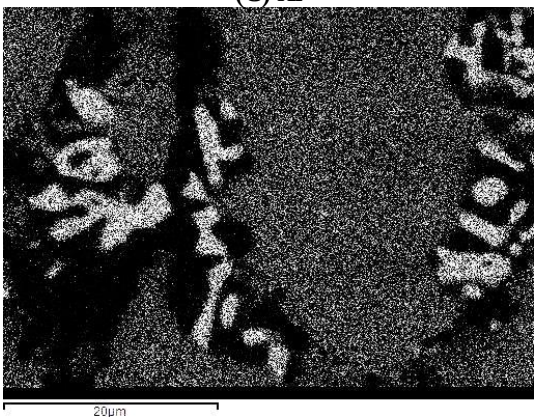

(E) Cr

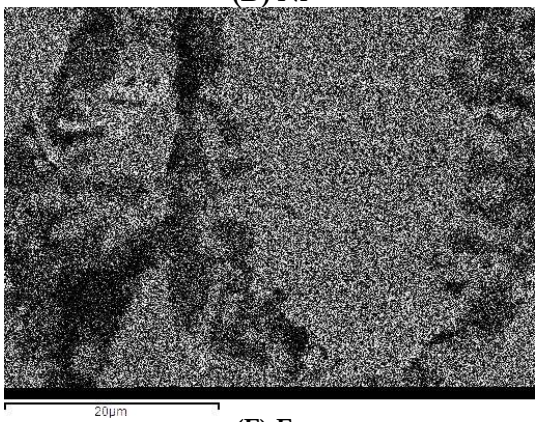

(F) Fe

(G) Co

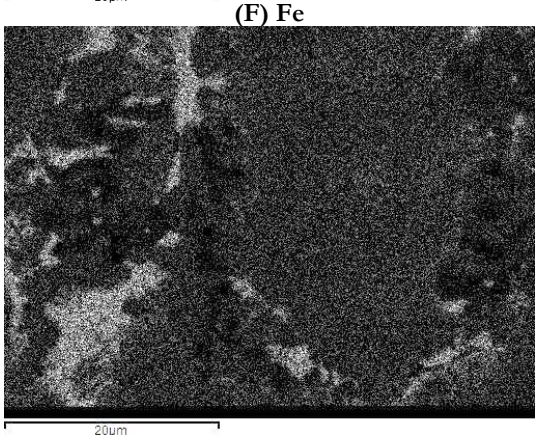

(H) Cu

Fig. 4.4: HEA5 – 700°C /1000H micrographs.
(A): lower magnification; (B): higher magnification; (C-H): EDX elemental maps from image (B)

4.1.2 EDX Microanalysis

PHASE	STATE	Al	Cr	Fe	Co	Ni	Cu
NOMINAL	---	9.0	18.2	18.2	18.2	18.2	18.2
DR	As cast	8.0	18.4	19.3	17.6	20.1	16.6
	1000°C	6.8	22.5	22.7	20.6	18.9	8.4
	850°C	3.9	24.1	24.9	22.0	16.6	8.4
	700°C	6.6	20.4	21.9	19.8	18.5	12.8
ID	As cast	10.3	3.6	4.4	4.2	11.6	65.9
	1000°C	11.4	3.2	4.9	4.9	15.9	59.7
	850°C	9.9	1.9	2.6	2.7	11.0	71.8
	700°C	4.8	1.9	2.3	2.5	6.3	82.3
PR1+PR2	850°C	31.1	3.7	7.8	10.0	35.5	11.9
	700°C	31.8	2.5	8.3	10.7	38.7	8.0
PR3	850°C	0.8	53.0	21.5	18.6	5.5	0.6
	700°C	0.5	52.1	23.2	19.1	4.4	0.7

Table 4.2: EDX microanalysis of the HEA5 samples (at. %)

As introduced in the §3.3, EDX measurements were performed at low magnification over large areas in order to determine the average composition of each heat treated sample. The results are here not included since they are within 1 at.% of the nominal composition.

Table 4.2 collects all the data relative to each one of the microconstituents detected in the micrographs and resolvable by the EDX probe. The data here exposed are average values of 5 point measurements.

The DR contains similar amounts of Cr,Fe,Co,Ni and it is poor of Al and Cu. The amounts of Al,Ni,Cu in the DR drop from 700°C to 850°C: they are probably employed for the coarsening of the Ni,Al-rich precipitates (PR1+PR2) that are bigger in the 850°C aged sample, as formerly stated. The small DPR detected in the 850°C aged sample will be regarded as Cu-rich precipitates, given the small traces in the Cu map in Fig. 4.3-(H).

The ID is extremely Cu-rich and with a mix of others elements each one less than 5%, except for Ni and Al. Looking at the aged samples, Cu gets higher as the temperature

decreases given the significant decreasing of the amount of others elements (particularly low in the 700°C and 850°C).

The microanalysis performed on the 850°C aged sample revealed that globular PR1s are around 30% Al and 35-38% Ni and very low in Cr. The same composition was observed for the PR2s (in the 850°C they are big enough to allow an accurate measurement). This proves the chemical identity between PR1s and PR2s that can be then considered the same phase. The morphological differences may be attributed to the differing formation pathways, as described in §4.3.1. The EDX analysis of needle-like PR2 in the 700°C treated sample was not enough accurate since they are too small. Notwithstanding, the analysis of an area containing both the DR and the PR2 showed composition close to an average between the DR and PR1 suggesting the PR2 may be the same phase as PR1, as demonstrated in the 850°C.

PR3s are composed primarily of Cr, over 50%, and of 20% of both Fe and Co. Al and Cu are present only in very small concentrations.

Remarkably, the 1000°C aged sample and as cast condition sample are very similar: the ID and DR phases are the only ones detected and they have similar composition.

4.1.3 XRD Diffractograms

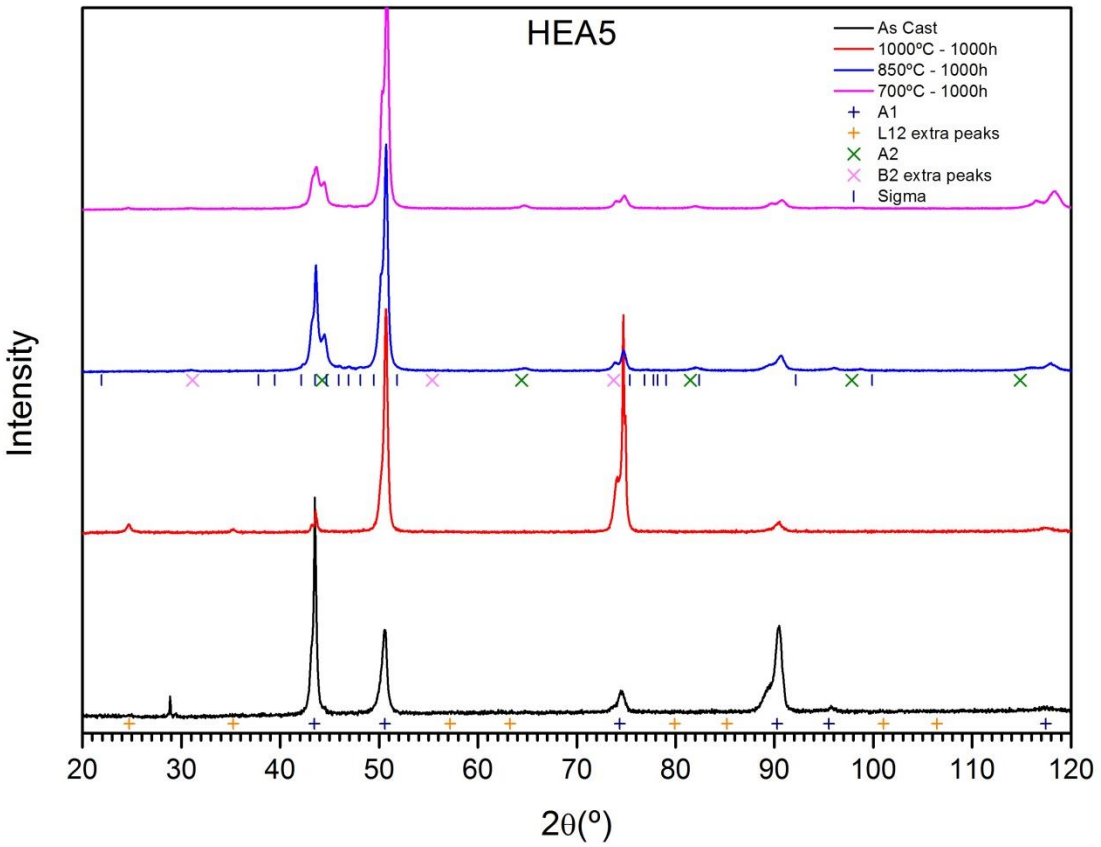

Fig. 4.5: Diffractograms of HEA5 samples

AS CAST CONDITIONS

As shown in Fig. 4.5, the as cast sample is predominantly A1 but other not identified peaks are detected like the one at 29°. The peaks at 74°C and 90°C exhibit a shoulder on lower angle values: this cannot be the Kα1-Kα2 splitting since the shoulder should be located on the higher angle value side [57]. Hence the peak splitting can be only due to the presence of two *fcc* structures, or two A1 (A1-A1) or one A1 and one $L1_2$ (A1- $L1_2$) with similar lattice parameter. Moreover the existence of two different phases is supported by the micrographic examination that shows that ID and DR are significantly different by a compositional point of view. The lattice parameters were calculated in a previous work conducted by Jones *et al.* [13] at the Rolls-Royce UTC (University of Cambridge). To account for the peak splitting, each diffraction peak was fitted with two peaks profile functions using a Lavenberg-Marquandt non-linear least squares algorithm in Wavemetric Igor Pro. Each profile function was a summation of two Gaussian peaks, to allow for the contributions from Kα1-Kα2 Cu radiation. The lattice parameters were then evaluated from the fitted Bragg angles of each peak through a non-linear least

squares minimisation and the ratio of the areas of the profile provided an estimate of the relative volume fractions of each phase. The results are shown in Table 4.3. The peak used for the calculation is the one at around 74° related to {220} planes. The area of the broader peak was approximately 2-3 times greater than that of the sharper peak, consistent with area fraction of dendrites and interdentrites, as demonstrated by Fig. 4.9-(A). The average values of DR (broad peak) and ID (sharp peak) lattice parameters are 3.602Å and 3.595Å respectively. The broadness of the DR peak is supposed to be the result of wide solidification range, that results in microsegration and hence to a continuous variation in the lattice parameter. This is confirmed by the dendrite coring observed in Fig. 4.9-(E-G). On the other hand, the sharpness of the ID peak suggests that its lattice parameter is well defined, a feature that would be consistent with a narrower solidification range.

Phase	Lattice Parameter (Å)
A1 (1) - DR	3.602
A1 (2) - ID	3.595

Table 4.3: HEA5-AS CAST Lattice parameters

1000°C / 1000H AGED

The diffractogram of the 1000°C aged sample still exhibits peaks splitting, especially considering the peaks at 43° and 74°. Hence the presence of A1-A1 or A1- $L1_2$ as in the as cast condition is foreseen. However, $L1_2$ extra peaks due to superlattice reflections of {100} planes at 25° and of {110} planes at 35° (absent in the A1) are clearly visible in this sample. This evidence leads to conclude that the peak splitting is due to the presence of one A1 and one $L1_2$ phases. Furthermore, the $L1_2$ phase is reported in other similar high entropy alloys ([1], [2]). The absence of strong evidence of $L1_2$ extra peaks in the as cast sample may be due to a lack of diffraction contrast between the atoms that occupy the face and corner sublattices or to grain texture that was not favourable to expose a great number of {100} and {110} planes. Since the peaks of $L1_2$ and A1 are clearly discernible, it was possible to estimate the lattice parameter of both, obtaining that the $L1_2$ is the smaller one, meaning that $L1_2$ peaks are the one at higher angle value side. The calculation was performed as described in §3.4 and collected in Table 4.5. Moreover a fitting of the peaks at 74° was performed with Origin 8.5 (Gaussian peaks) in order to calculate the area and then to have an approximate estimation of the volume fraction of each phase. The broader peak centred at lower angles has area 1.6 times larger than the

other peak as shown in Table 4.4. Comparing with Fig. 4.11-(A) one can suppose that, as in the as cast sample, the broader peak is related to the DR and the other to the ID.

	Centre	FWHM	AREA
A1 (1)	74.35125	1.4837	61.27532
A1 (2) or $L1_2$	74.75162	0.34275	38.72468

Table 4.4: HEA5 1000°C Peak fitting results.

The peak at 74° shows a split also on the higher angle side: in this is case this may be due to the Kα1- Kα2 splitting.

Finally, the 1000°C aged sample appears to be dual phase as cast one. This correspondence reflects the micrographic similarity.

Phase	Lattice Parameter (Å)
$L1_2$	3.616
A1	3.589

Table 4.5: HEA5-1000°C/1000H Lattice parameters

850°C / 1000H AGED

Once again in the 850°C aged sample there are evidences of *fcc* peak splitting. Contrary to the 1000°C aged sample, there is no trace of $L1_2$ superlattice peaks at 25°. The split peak has been treated with Origin 8.5 as for the 1000°C aged sample (graphs and data omitted). The broad peak centred at lower angles has 2 time larger area then the sharper peak.

Differently to the previous samples, body centred structure (*bcc*) peaks, A2 or B2 are manifest at 44,5° ({011} planes), 65° ({002} planes) and 116° ({310} planes). Moreover one tiny peak at 31° could be the B2 superlattice reflection of {100} planes, but it is too weak to be conclusive.

An accurate observation allows to notice other several weak peaks between 45° and 49°. They may be an evidence of σ phase, especially considering the strongest isolated peak at 47°. The σ peaks are weak because low symmetry structures (like σ, tetragonal) produce peaks with much lower intensity in respect to the high symmetry structure [57].

The number of phase clearly detected by the XRD is then four, meanwhile from the micrographs it was six. This observation leads one to assume that PR1s and PR2s, both Ni,Al-rich (accordingly with the EDX analysis) could be the same phase, as hypothesised in §4.1.2. Moreover DPRs have a too low volume fraction to be detected by XRD or

they are the same phase of the ID, given the similar compositional contrast. With these two hypotheses the number of phases detect by XRD matched with the micrographs examinations. The lattice parameters are reported in Table 4.6:

Phase	Lattice Parameter (Å)
A1(1)	3.624
A1(2)	3.590
bcc	2.871
Sigma	a=4.543 c=8.808

Table 4.6: HEA5-850°C/1000H Lattice parameters

700°C / 1000H

Also in the 700°C aged sample the *fcc* structure is still predominant and split peaks are evident.

One small peak at 25° is discerned and it corresponds to the $L1_2$ superlattice reflection peak, but it is too weak to be conclusive.

The *bcc* peaks are still noticeable, as well as the tiny peak at 31°. This peak, supposed to be due to the superlattice reflection of the {100} planes in the B2, is still too small to be conclusive.

Considering in more detail the 2θ interval between 45° and 49°, other weak peaks are traceable. From comparison with the 850°C aged sample, they may be possible evidence of σ. Moreover the existence of σ, one *bcc* (A2 or B2) and two *fcc* has to be supposed in order to match with five phases observed in the micrographic examination. Table 4.7 gathers the calculated lattice parameters:

Phase	Lattice Parameter (Å)
A1(1)	3.616
A1(2)	3.588
bcc	2.871
Sigma	a=4.543 c=8.808

Table 4.7: HEA5-700°C/1000H Lattice parameters

4.1.4 DSC

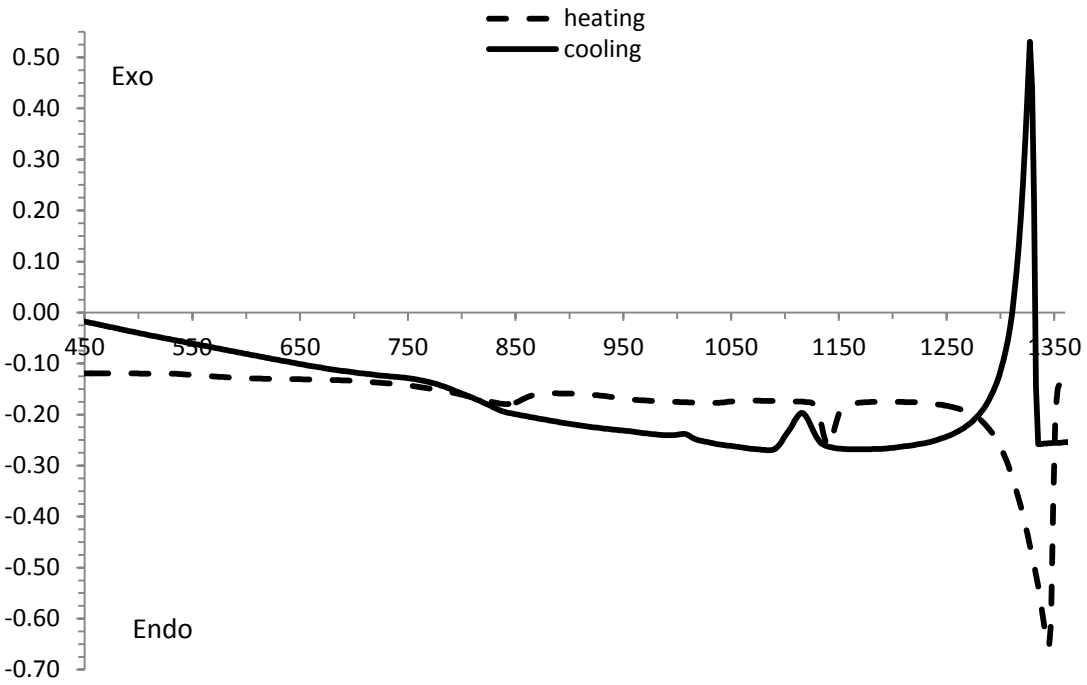

Fig. 4.6: DSC Thermogram of the HEA5-700°C / 1000H.

The DSC is performed only on the 700°C / 1000H sample and the thermogram is represented in Fig. 4.6. Upon heating a first shoulder is met at around 800-850°C. This kind of behaviour is consistent with solid state solid dissolution of precipitates. Given the data collected in the micrographs, EDX and XRD, the nature of the precipitates that are dissolving could be identified as the decomposition of σ into A1 or dissolution of ordered $L1_2$ to A1, typical of Ni-based superalloys [70]. Indeed σ dissolves during heating above 850°C in duplex steels [76]. On the other hand, $L1_2$ precipitation is induced in Ni superalloys by aging at temperatures around 750-850°C [61], [70]. This is in agreement with what observed Fig. 2.12 [72]**,** where it was noticed that for an alloy Al-Ni-Cr alloy with Al≈10% the $L1_2$ *solvus* temperature is around 830°C [61]. The dissolution of $L1_2$ at temperature below 1000°C should imply the absence of $L1_2$ in the 1000°C XRD data, but on the contrary they are evidently present. This fact is explained considering that $L1_2$ precipitation cannot be avoid even with rapid cooling, as demonstrated by primary gamma prime precipitates in superalloys discussed in §2.3.2 [61]. Other two endothermic peaks are evident, and they are identified on the basis of order of formation of the microstructure, i.e. the ID is the first to melt upon heating and the DR is the last one. Hence, there are fusion of the ID phase at 1120-1150°C and fusion of the DR phase at

1285-1350°C. The melting temperature of the ID melting of confirmed by the verticals section of the ternary diagram AlCuNi (Fig. 2.26 [60]) and also by previous work [3].

In addition, a broad flat peak from 910 to 1040°C (and its respective sharper peak during cooling) is detectable. The interpretation of this peak is discussed in §4.2.4.

During cooling from high temperature the two strong exothermic peaks correspond to DR and ID solidification respectively at 1330°C and 1120°C (as seen on the heating curve). The cooling curve exhibit also a first shoulder starting at 1030°C, more or less in correspondence to the broad weak peak observed upon heating. Finally a shoulder at 850°C is observed, reciprocal to the one detected upon heating. But, as stated in §2.3.3 [76]**,** σ does not form on fast cooling so that the shoulder at 850°c on cooling should be attributed only to $L1_2$ precipitation.

4.2 HEA5 – DISCUSSION

The discussion will be held considering each one of the microconstituents detected in the results §4.3 in order to motivate their formation accordingly to the ternary diagrams study done in the §2.3 and accordingly to all the experimental data.

4.2.1 Dendrites (DR)

Considering that XRD data of the as cast (Fig. 4.5) shows only *fcc* and taking in account the EDX analysis in Table 4.2, it is evident that DR is a saturated A1 Ni,Cr,Fe,Co-based solid solution. Indeed, the DR phase is observed in all the samples and then it must be one of the *fcc* detected in the all the XRD diffractogram. DR composition is solubility limits of the several ternary A1 solid solutions based on Cr-Fe-Co-Ni are consistent as argued in §2.3.4. In this solid solution Ni plays the role of A1 stabilizer and Cu solvent. Indeed, because of the total solid state immiscibility of Cu in Co-Cr and Cr-Fe solid solutions (due to the Cr-Cu immiscibility), solubility of Cu in the A1 phase markedly suffers the presence of Cr and its compatibility in the solid solution is guaranteed prevalently by Ni (given the total solid state miscibility of Cu in Ni). Furthermore, the total solid state immiscibility of Cr and Cu explain the Cu segregation, as discussed in §4.2.2.

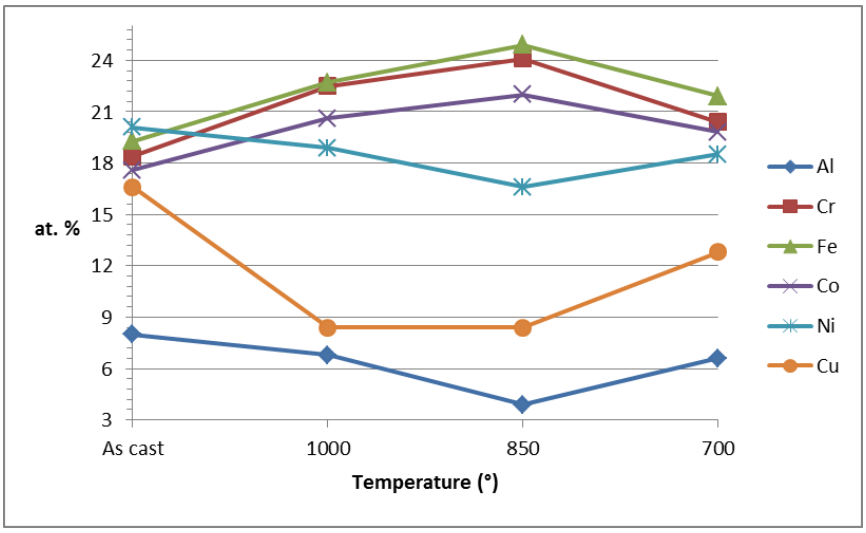

Lattice parameter Å	
As cast	3.602
1000°C	3.616
850°C	3.624
700°C	3.616

Fig. 4.7: Elements content in function of the treatment temperature in the DR and lattice parameters

The great influence of Cr on the Cu solubility in the DR A1 is proved also by the fact that Cu amount decreases increasing the treatment temperature, contrarily to the evidence that Cu solubility increases with temperature in A1 Ni,Cr,Fe,Co-based (§2.3.4). Indeed Cu rejection upon heating is due to the increased amount of Cr in the A1. The effect of increased amount of Cr on Cu solubility overwhelmed the effect of the increased temperature.

As previously seen §2.3.4, Cr (*bcc*) is the strongest A1 destabilizer and Cr excess leads to σ and A2 (with σ formation discouraged by sufficient amount of Ni). Also excess Al, whose solubility is set at values sensibly lower than 8% (especially considering CoFe A1 [92], as stated in §2.3.4) provokes NiAl B2 precipitation. Hence, Al and Cr solubility in the DR accounts for formation of B2 and σ detected by XRD in 700°C and 850°C aged samples. Indeed in as cast condition the Al content is beyond the solubility limit and then upon heating is released to form NiAl B2 precipitates (PR1s and PR2s). As evident from the graph in Fig. 4.7, Al and Ni variation are coupled, meaning that the rejection of Al implies also Ni rejection. The depletion of Al and Ni in the matrix (known to be σ blockers, 2.3.3§) allows σ formation, as it will described in the following paragraphs. The Al and Ni content drop from 700°C to 850°C is related to the fact that they are employed for the coarsening of PR1s and especially of in grain acicular PR2s. The increased amount of Al and Ni in the DR from the 850°C to 1000°C is on the contrary due to the dissolution of the NiAl B2 in the DR.

Remarkably, the variations of Al and Ni are anti-correlated to the one of Cr, Fe and Co.

As said in §4.1.3, among the two *fcc*, the DR is matched with the pattern that subtends larger areas (meaning larger volume fraction) and whose peaks are positioned at lower angles (bigger lattice parameter). The lattice parameters so found are in agreement with literature data [107], [108]. In the 1000°C treated sample, the pattern related to the DR *fcc* exhibits also peaks due to $L1_2$. Since the DR cannot be an $L1_2$ structure for compositional reasons (excess of solute elements §2.3.2), the pattern of the DR *fcc* is then actually due to the overlap of the DR A1 and one $L1_2$ with basically identical lattice parameter. The $L1_2$ will be discussed in the following paragraph. Then the 1000°C sample reveals to consist of three phases: A1 (DR)+ $L1_2$ + A1 (ID). Similar consideration may be adopted for the *fcc* in the as cast and 700°C XRD diffractograms.

4.2.2 Interdentrites (ID)

Given the XRD data of the as cast (Fig. 4.8), also the ID has to be an *fcc*. Considering the EDX analysis with the examined ternary diagrams, the ID is then considered to be an A1 saturated Cu,Ni-based solid solution. Indeed, similarly to the process done for the DR, Cu-rich interdentrite phase is present at any aging temperature and then it can be only A1. Considering the elements in the ID, the only Cu rich phase that can allow them is the Cu,Ni-based A1, where Ni plays the role of compatibilizer for Cr,Fe,Co in the Cu matrix. Their solubility remains very low: indeed, as said in §2.3.7, solubility of Cr in Cu,Ni A1 is almost negligible at temperature below 950°C and also Fe and Co are little soluble. The Cu segregation may be explained considering the low affinity of Cu with most of the elements in the alloy, especially Cr,Fe,Co, as shown in the respective binary diagrams [93]–[95].

Temperature increases enhances solubility of the several elements in the ID and it explains why the total amount of the Cu decreases at higher temperatures. Indeed the higher content of substituting elements reduces the relative percentage amount of Cu (Fig. 4.8).

Solubility limit of Al is very low, less than 5% at 700°C if Cu is over 65% and it rises up to 10% at 900°C. Hence in the as cast condition the Al exceeds the solubility limits and this induces NiAl B2 precipitates in the 700°C and 850°C aged samples. They are able to re-dissolve in the matrix at 1000°C.

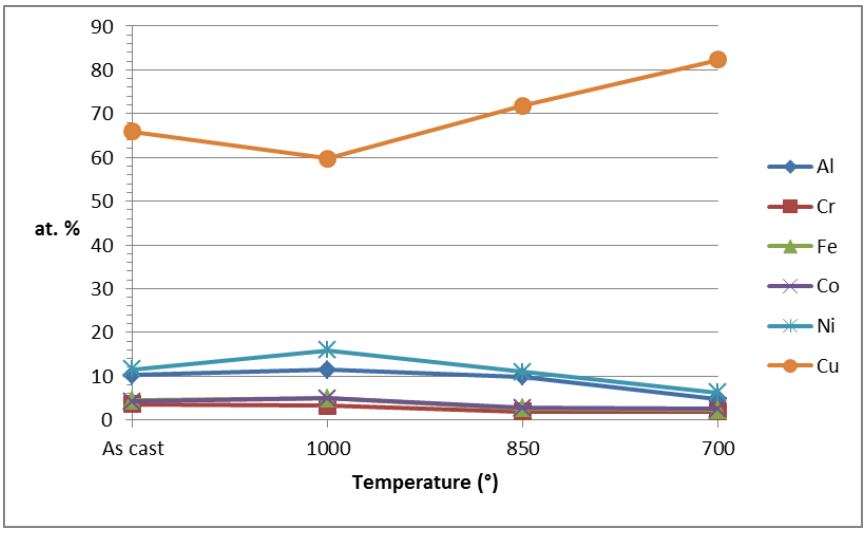

Lattice parameter Å	
As cast	3.595
1000°C	3.589
850°C	3.590
700°C	3.588

Fig. 4.8: Elements content in function of the treatment temperature in the ID and lattice parameters

As consequence of NiAl B2 precipitation, the available amount of Ni in the ID is reduced and that makes the solubility of Cr in Cu drop to almost zero. The expulsion of Cr on the grain boundaries promotes σ phase nucleation.

The values of the lattice parameter are obtained as described for the DR so that the sharp peak with lower area that is lower volume fraction is attributed to the ID. The values here reported are in agreement with literature works [109].

Cu-rich segregation into the interdentrites forms because of the highly positive ΔH_{mix} with Co, Fe and Cr. Indeed the positive mixing enthalpies between Cr-Cu and between Fe-Cu surpass 10kJ/mol (12 and 13 kJ/mol respectively [53]) and this value is regarded as the mixing enthalpy upper limit that can be counterbalanced by the configurational entropy ΔS_{conf} effect allowing effective mixing between incompatible elements, as stated is §2.1.1 [28].

4.2.3 $L1_2$ Phase

The first proof of formation of $L1_2$ phase is provided by the XRD: in the 1000°C aged sample (and less clearly in the as cast and in the 700°C ones) the $L1_2$ extra peaks due to superlattice reflections of {100} planes at 25° and of {110} planes at 35° (absent in the A1) are discernible. To be more precise, as above stated, the $L1_2$ diffractogram is actually overlap to the DR A1. The $L1_2$ diffractogram cannot be simply attributed to the DR or to the ID for compositional reason (§2.3.2). Only in the work conducted by Singh *et al.*

(2011) [34], the interdentric phase, with similar composition to the present one, has been described as $L1_2$ by TEM EDX measurements but in the AlCuNi phase diagrams (Fig. 2.9 [68]) and in any other work no $L1_2$ such rich in Cu are reported.

The second supporting evidence of $L1_2$ is given by the in Fig. 4.6. Indeed the shoulder at 800-850°C is due to precipitation of Ni_3Al γ' $L1_2$ intermetallic compound typical in Ni-based superalloys. The formation upon cooling of Ni_3Al $L1_2$ (primary γ') takes place on a nanometric scale, and this accounts for the fact that only two phases (DR and ID) are resolvable by the SEM examination [61] and their formation cannot be prevented by quenching from higher temperatures [61], [72]. As shown by the diagram in Fig. 2.12 of Al-Cr-Ni system, Al content of around 10% means a *solvus* temperatures of Ni_3Al of about 830°C [72]. So that the weak $L1_2$ peaks observed in the as cast may be due to the precipitates formed during cooling. Indeed, as formerly observed §2.3.4, at 700°C the solubility of Al in the A1 DR should be around 6%. Upon heating from the as cast (where Al content in the DR is 8%) the Al excess provokes the precipitation of B2 NiAl and $L1_2$ at 700°C. This accounts for the fact that the weak $L1_2$ extra peak is even more visible at 700°C. This peak is totally absent in the 850°C that means that $L1_2$ does not form at all in the DR even during cooling. This is because, respect to 700°C, at 850°C a bigger amount of Al has been rejected from the DR and employed in B2 formation. The Al amount in the DR is then not enough to induce Ni_3Al precipitation during cooling. Indeed as observed in §2.3.2, a minimum amount of Al (≈10%) is required to form Ni_3Al. Confirmation of the fact that Al is prevalently sequestrated by the NiAl is given by the EDX analysis in Fig. 4.5. Indeed, the drop of Al form 700°C to 850°C in the DR is not due to a decrease of solubility (since it is increased by temperature, see §2.3.4) but to the fact that at 850°C Al prefers to partition in the NiAl B2, that is stable at that temperature, contrarily to the Ni_3Al that is close to its *solvus* temperature. In the 1000°C aged sample the $L1_2$ extra peaks are clearly noticeable. The reason is that at 1000°C the solubility of Al is greatly increased in the DR and then NiAl precipitates dissolve in the DR that is hence enriched in Al. Therefore, during cooling, the Al is sufficient to provoke Ni_3Al precipitation.

Precipitations of the Ni_3Al $L1_2$ phase may be expected to take place also in the ID, as shown in Fig. 2.26 and with similar *solvus* temperautre above discussed. Indeed, with Cu≈80%, Ni=10% and Al≈10% (as in the ID) precipitation of $L1_2$ is predicted to occur

at temperaure below 750°C. Even if this is a viable mechanism too, no traces of $L1_2$ superlattice reflections are found in the ID of HEA6 (as displayed in Fig. 4.14) that possesses ery similar compotion (Table 4.11), suggesting that $L1_2$ precipitations happens in the DR.

The hypothesis that the DR and the $L1_2$ diffractograms are not discernible because they possess the same lattice parameter is likely as proved by the discussion in §2.3.2: the effect of substituting elements can make lattice parameter of Ni-based A1 (DR) very similar to the one of the $L1_2$ 3.57Å at room temperature [61], [73].

4.2.4 Precipitates PR1 and PR2

	Al	Cr	Fe	Co	Ni	Cu	Lattice Parameter Å
850°C	31.1	3.7	7.8	10.0	35.5	11.9	2.871
700°C	31.8	2.5	8.3	10.7	38.7	8.0	2.871

Table 4.8: EDX analysis and lattice parameters of HEA5 precipitates PR1 And PR2

The EDX analysis data combined with the evidence of *bcc* structure in the XRD in the 850°C and 700°C aged samples and the review of the Al-Ni-X ternary diagrams suggested that PR1s and PR2s are NiAl intermetallic compound with a B2 crystal structure (as described in §2.3.1). Hence, the small evidence of the reflection of {100} planes at 31° (Fig. 4.5) is reasonably ascribed to the superlattice reflection of the B2 structure. Formation of B2 NiAl-based phase upon heating is reported in alloys with similar compositions also in previous works [10], [12], [38].

The solubility limits of several elements in the NiAl have been previously described §2.3.1, but it is useful to recall that in the B2 structure Fe, Co substitutes in large amounts Ni, since they can form B2 aluminides with Al. Cu enters in the Ni sublattice but its solubility is limited at around 20% when Ni is not exceeding 50%. On the other side, Cr substitutes Ni and Al almost equally but solubility of Cr is quite low, especially in FeAl B2 (less than 5%). These observations can explain the EDX data in Table 4.8 and particularly the low content of Cr.

Considering the Ni-substituting elements (Fe,Co and Cu), the Al content of the PR1s and PR2s is well below the stoichiometric value (50%). This is explained considering that NiAl is a Berthollide [62], that means that it allows deviations from stoichiometry. For

example on the AlFeNi system at 850°C Al content in the B2 phase is reduced down to 22% (boundary of B2 phase in equilibrium with A1) [64], as shown in Fig. 2.7.
Precipitation of the B2 phase is foreseen by the ternary diagrams considering that Al solubility limits in the DR (Ni,Cr,Fe,Co-based A1) and in the ID (Cu,Ni-based A1) are respectively lower than 8% and 10% at temperatures below 900°C (§2.3.4and §2.3.7). Hence in the as condition the Al content exceeds the solubility both in the DR and in the ID (Table 4.2), where it was trapped by the rapid cooling rate during solidification, that does not allow the achievement of the equilibrium. For this reason upon heating from the as cast condition the excess of Al is rejected and it forms B2 with Ni. Indeed, as formerly noticed, Al content drops in the DR and ID from the as cast to the 700°C aged sample. This precipitation event accounts also for the two different morphologies: globular PR1s at the grain boundaries and acicular like PR2s within the grains. Indeed the Al rejected outside of the grain formed the globular ones, since along the grain boundaries the disorder allows a globular growth given that atom packing is not regular. On the contrary the NiAl precipitated in grain grew in an acicular shape in order to minimize the distortion. Finally, as before observed, at 1000°C the NiAl B2 can be dissolved both in the DR and in the DR, given the increased Al solubility. Indeed, for Al≈10-13% dissolution of NiAl into the A1 is foreseen at temperatures close to 1000°C, as evident from Fig. 2.20 [90]. This accounts for the absence of B2 peaks and PR1 and PR2s in Fig. 4.11.

NiAl dissolution may be responsible of the broad flat peak from 910 to 1040°C observed in the DSC in Fig. 4.6. In correspondence to this broad peak there is a shoulder starting at 1030°C on the cooling curve. This peak is reproducible (obtained also from the as cast sample in previous work conducted by Jones *et al.* [13]) so that it is a stable feature in HEA5. Its interpretation as B2 precipitation event (as said for the peak on the heating curve) is not conclusive since it is located a little over 1000°C. This means that it should be related to a hypothetic phase present also in the 1000°C sample, where nevertheless only ID and DR are visible. Micrographic and XRD studies at intermediate temperature should be performed in order to clarify this observation.

4.2.5 Precipitates PR3

The EDX analysis and XRD pattern of the 850°C treated sample suggests that PR3 are σ phase or more properly a combination of $Cr_{0.48}Fe_{0.52}$ and $Cr_{0.6}Co_{0.4}$. σ formation is also found in other high entropy alloys with very similar composition after heat and mechanical treatments [16-20].

	Al	Cr	Fe	Co	Ni	Cu	Lattice Parameter Å
850°C	0.8	53.0	21.5	18.6	5.5	0.6	a=4.543 c=8.808
700°C	0.5	52.1	23.2	19.1	4.4	0.7	a=4.543 c=8.808

Table 4.9: EDX analysis and lattice parameters of HEA5 precipitates PR3

The role of each element in σ phase has already been described in §2.3.3**,** and they are here briefly recalled in order to highlight the agreement with the chemical composition in Table 4.9. Al and Ni are σ destabilizer and in particular Al has low very low solubility in CrFe σ. Basically no Cu solubility is allowed in σ. On the contrary, Fe has a large solubility in CrCo σ, but it decreases with increasing temperature. Temperature induces also thermal suppression of CoCr σ at 1282°C, and of CrFe σ at 840°C, so that the suppression of the PR3s σ is expected to be in the between, around 1000°C. This fact allows for the disappearance of σ in the 1000°C aged sample.

σ precipitation is believed to be due to an excess of Cr in both the DR and ID. Indeed, as cast condition the amount of Cr exceeds the solubility limit (20-22% at 700°C for the DR, almost negligible for the ID, see §2.3.4 and §2.3.7). Upon heating Cr excess provokes σ precipitation from the DR and ID on the grain boundaries. Fig. 4.3 and Fig. 4.4 show that σ nucleates close to the NiAl B2 precipitates. This happens because the region on the side of is Al,Ni-depleted and richer in Cr, rejected from the DR and also from the NiAl itself (that has low compatibility with Cr). These two conditions, Al,Ni depletion and Cr enrichment, enhance σ formation.

From a kinetic point of view, the low solubility of Al in σ means that the diffusion of Al must occur before σ can nucleate and grow. This could set a kinetic constraint since if Al diffusion cannot occur in an adequate extent, σ formation is inhibited. Hence, since σ phase was detected also in sample treated with shorter heat treatment in previous researches ([16-20]), it means that the diffusion in HEAs is not sluggish as believed (§2.1.1)

4.3 HEA6 - RESULTS

The High Entropy Alloy no. 6 (HEA6) is the alloy with equimolar composition., with formula AlCrFeCoNiCu. The atomic percentage composition is given in Table 4.10.

at.%	Al	Cr	Fe	Co	Ni	Cu
HEA6	16.7	16.7	16.7	16.7	16.7	16.7

Table 4.10: Nominal Chemical Composition of HEA6 (% at.)

4.3.1 Micrographs

AS CAST CONDITION

Fig. 4.9-(A) and (B) respectively show the low and high magnification of the HEA6 as cast sample. Six features are recognizable:

1. Grey dendritic region (DR)
2. White interdendritic region (ID)
3. White precipitates in the DR (PR1)
4. Precipitation free zone in the DR (PFZ)
5. Thin black layer all around the ID (BL)
6. Transition zone in the ID (TR)

The low magnification image displays that the DR is the major phase. The observation of the image at higher magnification reveals that the small PR1s possesses a preferential orientation within the grain, probably because of the lattice constraints that bind the growth only to some more favourable directions.

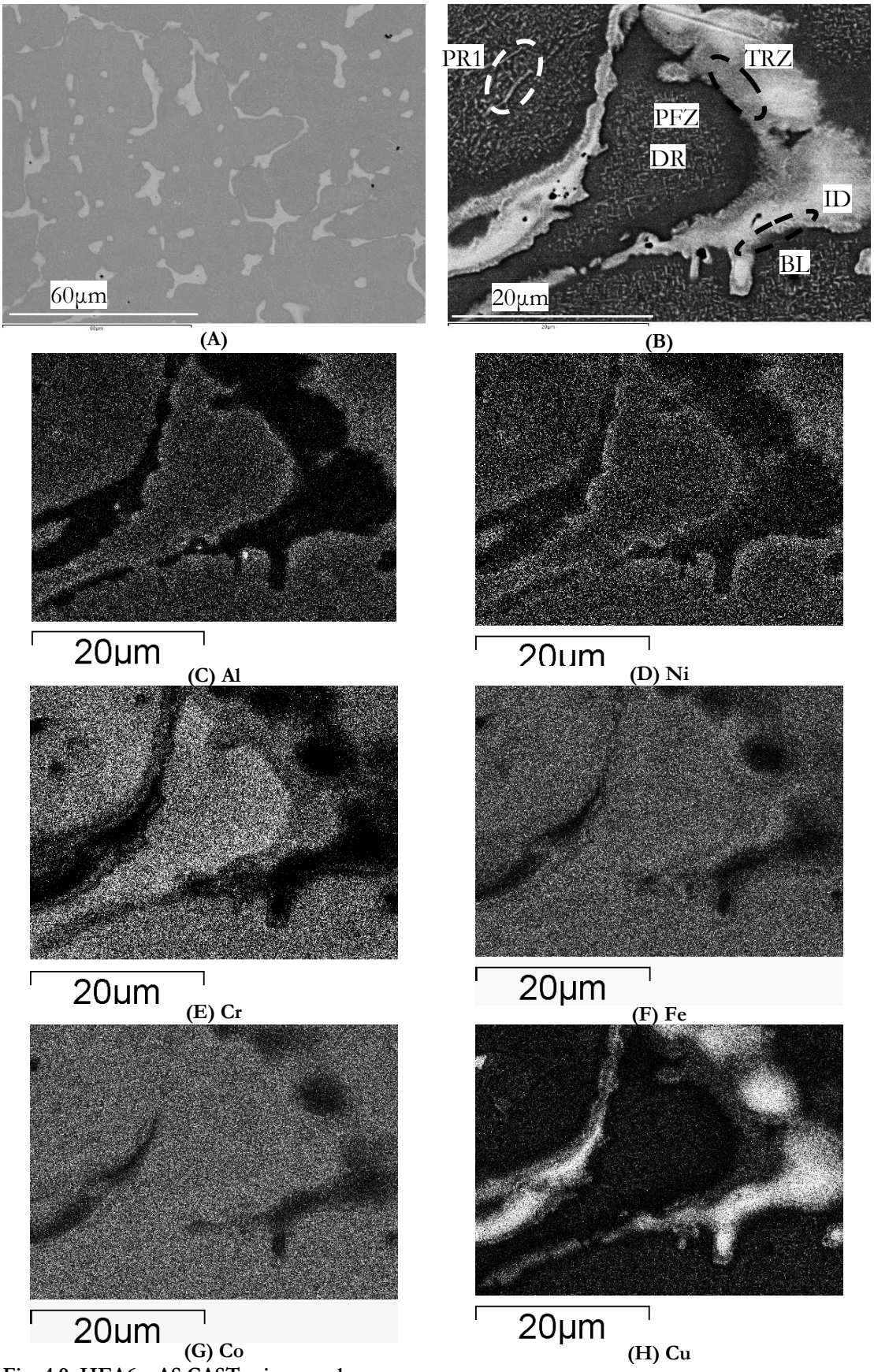

(A) **(B)**

(C) Al **(D) Ni**

(E) Cr **(F) Fe**

(G) Co **(H) Cu**

Fig. 4.9: HEA6 – AS CAST micrographs.
(A): lower magnification; (B): higher magnification; (C-H): EDX elemental maps from image (B)

Compositional information is provided by the EDX maps collected in Fig. 4.9-(C-H):

1. The DRs is Cr,Fe,Co-rich,
2. The IDs is Cu-rich;
3. The PR1s is Cu-rich (small traces in Fig. 4.9-(H));
4. The PFZ is Cr,Fe,Co-rich and there no traces of Cu;
5. The BL is Al,Ni-rich and Carafe-depleted;
6. The TRZ is Cr,Co,Fe,Cu-rich and Al,Ni-depleted.

Compositional information is well-rendered in Fig. 4.10, which represents a mixed map of Al, Cr and Cu. From this image one can appreciate that the BL is much less thick on the side of the ID where TRZ forms and that a Cu rich film forms on the outer part of the PFZ in contact with the TRZ.

Such a complex microstructure is related to strong partitioning during solidification: repulsion and separation overwhelmed homogenization effect of configurational entropy.

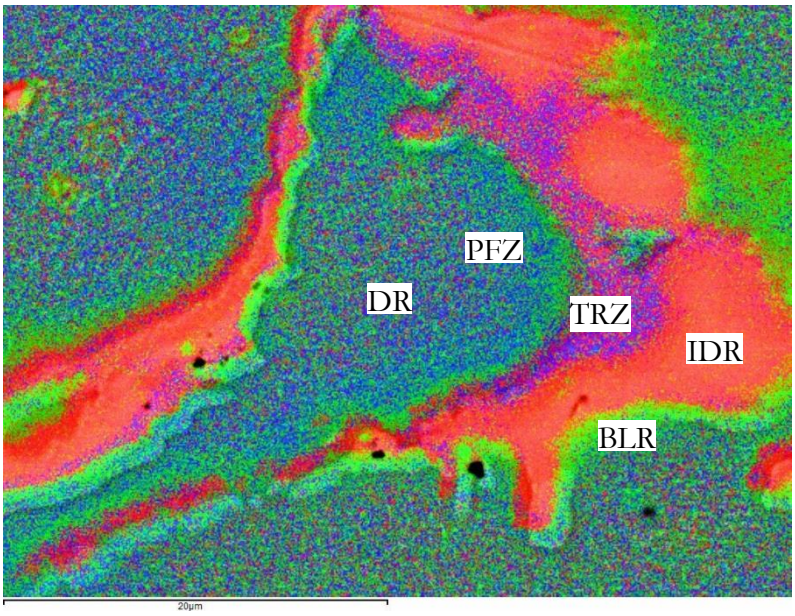

Fig. 4.10: Elemental mixed map of Cu (red); Cr (blue) and Al (green) from Fig. 4.9-B

1000°C / 1000H AGED

The microstructure of the 1000°C aged sample consists of four features (Fig. 4.11-(A) and (B)):

1. Grey dendritic region (DR);
2. White interdendritic region (ID);

3. Grey precipitates (PR2);
4. Precipitates in the DR(PR3).

The two families of precipitates were absent in the as cast condition and their distribution are slightly different: PR2s nucleate both at the ID-DR boundaries and within the ID, PR3s only in the DR.

Fig. 4.11-(C) to (H) displays the elements distribution and points out that in HEA6 not only Cu markedly segregate but Cr too:

1. The DRs are Al,Ni-rich;
2. The IDs are Cu-rich;
3. The PR2s are Fe,Cr-rich
4. The PR3s are Cr,Fe-rich

Remarkably, many micrographic regions are still severely separated even if this heat treatment was performed in proximity of liquidus temperature: this means that phase separation cannot be suppressed and then stabilisation effect of configuration entropy does not take place.

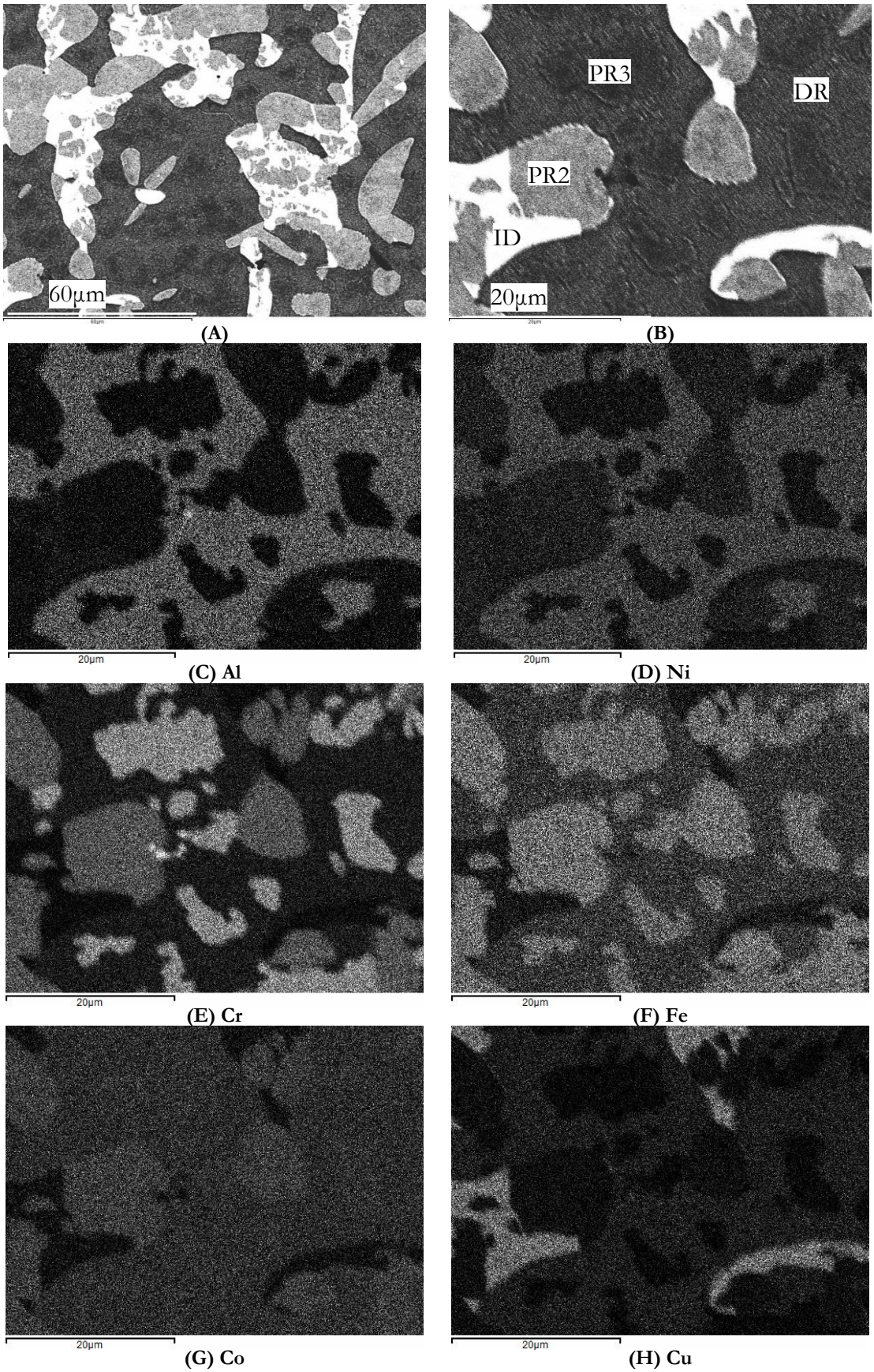

(A) **(B)**

(C) Al **(D) Ni**

(E) Cr **(F) Fe**

(G) Co **(H) Cu**

Fig. 4.11: HEA6 – 1000°C /1000H micrographs.
(A): lower magnification; (B): higher magnification; (C-H): EDX elemental maps from image (B)

850°C / 1000H AGED

After the heat treatment at 850°C the microstructure is composed of five main regions, as indicated in the high magnification in Fig. 4.12-(B):

1. Grey dendritic region (DR)
2. White interdendritic region (ID)
3. Small white precipitates in the DR (PR1)
4. Dark grey precipitates in the ID (PR2)
5. Light grey globular precipitates (PR3)

Compared to the 1000°C, the microstructure is much more fragmented and PRs heterogeneously nucleate at the DR-ID boundaries and within the grains. Remarkably, only the PR3s nucleates only on the grain borders. Moreover, in Fig. 4.12-(H), displaying the Cu EDX map, there is no evidence of composition difference between the ID and the PR1. The compositional information from the EDX maps shown in Fig. 4.12-(C) to (H) reveals that:

1. DRs are Al,Ni-rich;
2. IDs are Cu-rich;
3. PR1s are Cu-rich
4. PR2s are Fe,Cr-rich;
5. PR3s are Cr-rich.

700°C / 1000H AGED

The microstructure of the 700°C aged sample resembles the previous one but all the features are organized on a smaller size, as shown in Fig. 4.13-(A). At higher magnification (Fig. 4.13-(B)), five microconstituents are visible:

1. Grey dendritic region (DR)
2. White interdendritic region (ID)
3. Small white precipitates in the DR (PR1)
4. Tiny dark grey precipitates in the ID (PR2)
5. Light grey globular precipitates (PR3)

In comparison with 850°C sample, all the precipitates are much smaller, in particular the PR2s. Indeed, in order to detect them it was necessary to take into account also the

observations of the 850°C aged sample and to observation via the Fei Helios NanoLab (that allows higher resolution and magnifications).

The morphology and distribution of precipitates underlines that they still heterogeneously nucleate at the DR-ID boundaries, but a large amount nucleate in the bulk DR, where they seem to have a preferential orientation. Moreover the phase identified as DR is distributed as a film around the precipitates, similarly to the PRZ in the as cast. The big amounts of precipitates in the DR and its film distribution could be explained considering that the DR in the as cast is a metastable supersaturated solid solution. If this is verified, upon heating, the elements exceeding their solubility limit will induce precipitation of PR2 and PR3. Around these precipitates the matrix is now freed from the excess elements and it assumes the equilibrium structure. This hypothesis will be discussed further §4.4.2.

The EDX maps in Fig. 4.13-(C)to (H) were fundamental in the individuation of the five mentioned microconstituents, especially of PR2s:

1. The DRs are Al,Ni-rich;
2. The IDs are Cu-rich;
3. The PR1s are Cu-rich;
4. The PR2s are Fe-rich;
5. The PR3 are Cr-rich.

The prevalence of Fe content in the PR2s was determined observing that there are some Fe-rich spots in Fig. 4.13-(F) that do not corresponds to Cr-rich areas (highlighted in the circles).

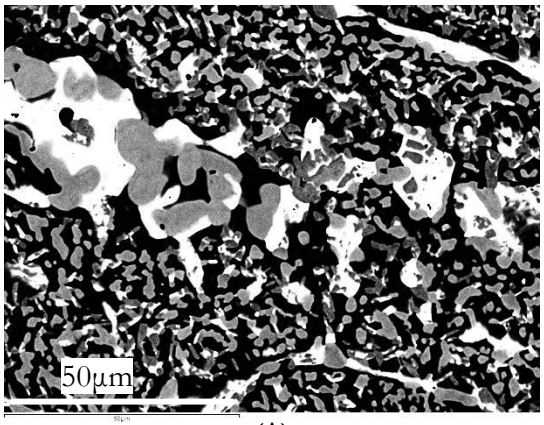

(A)

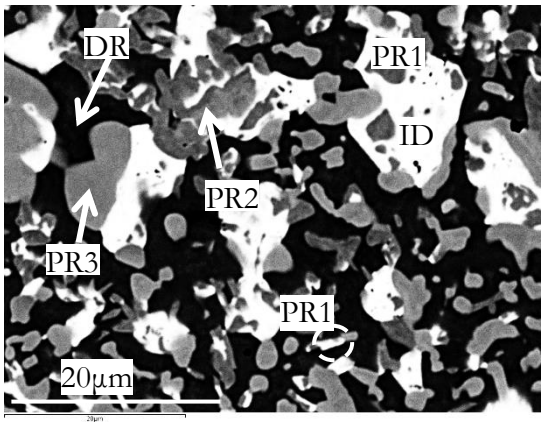

(B)

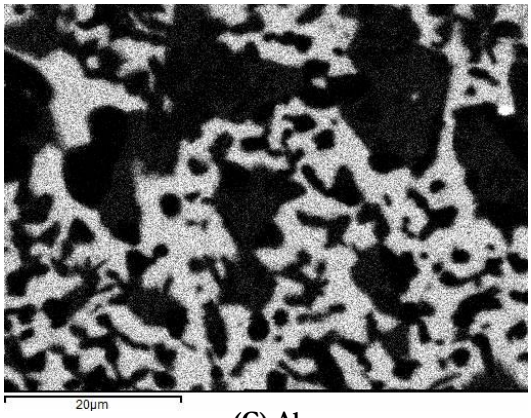

(C) Al

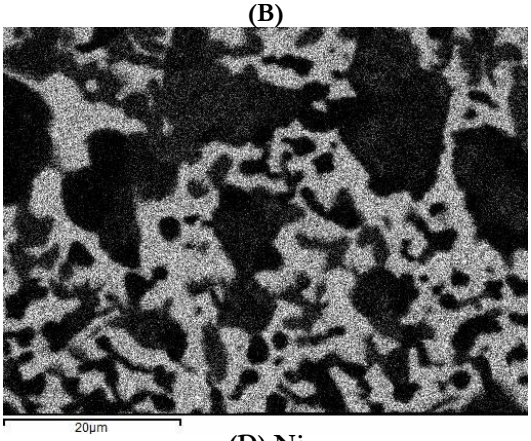

(D) Ni

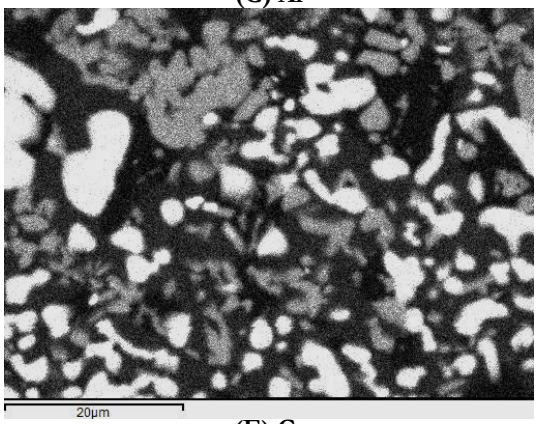

(E) Cr

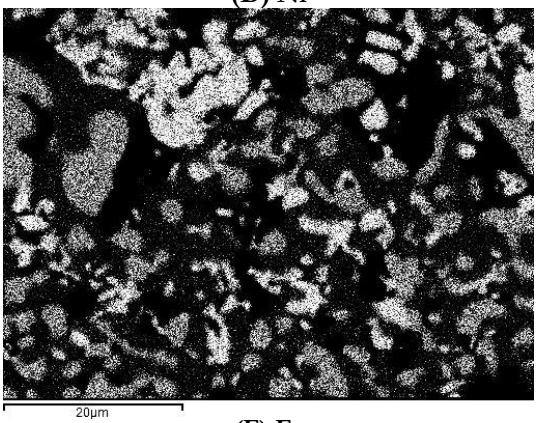

(F) Fe

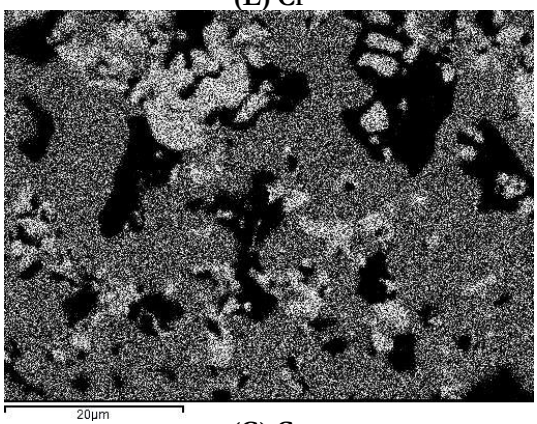

(G) Co

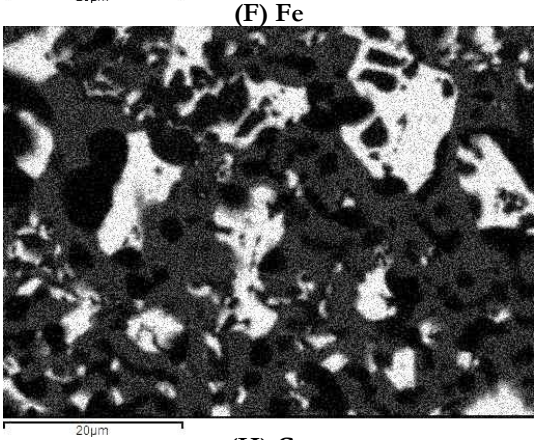

(H) Cu

Fig. 4.12: HEA6 – 850°C /1000H micrographs.
(A): lower magnification; (B): higher magnification; (C-H): EDX elemental maps from image (B)

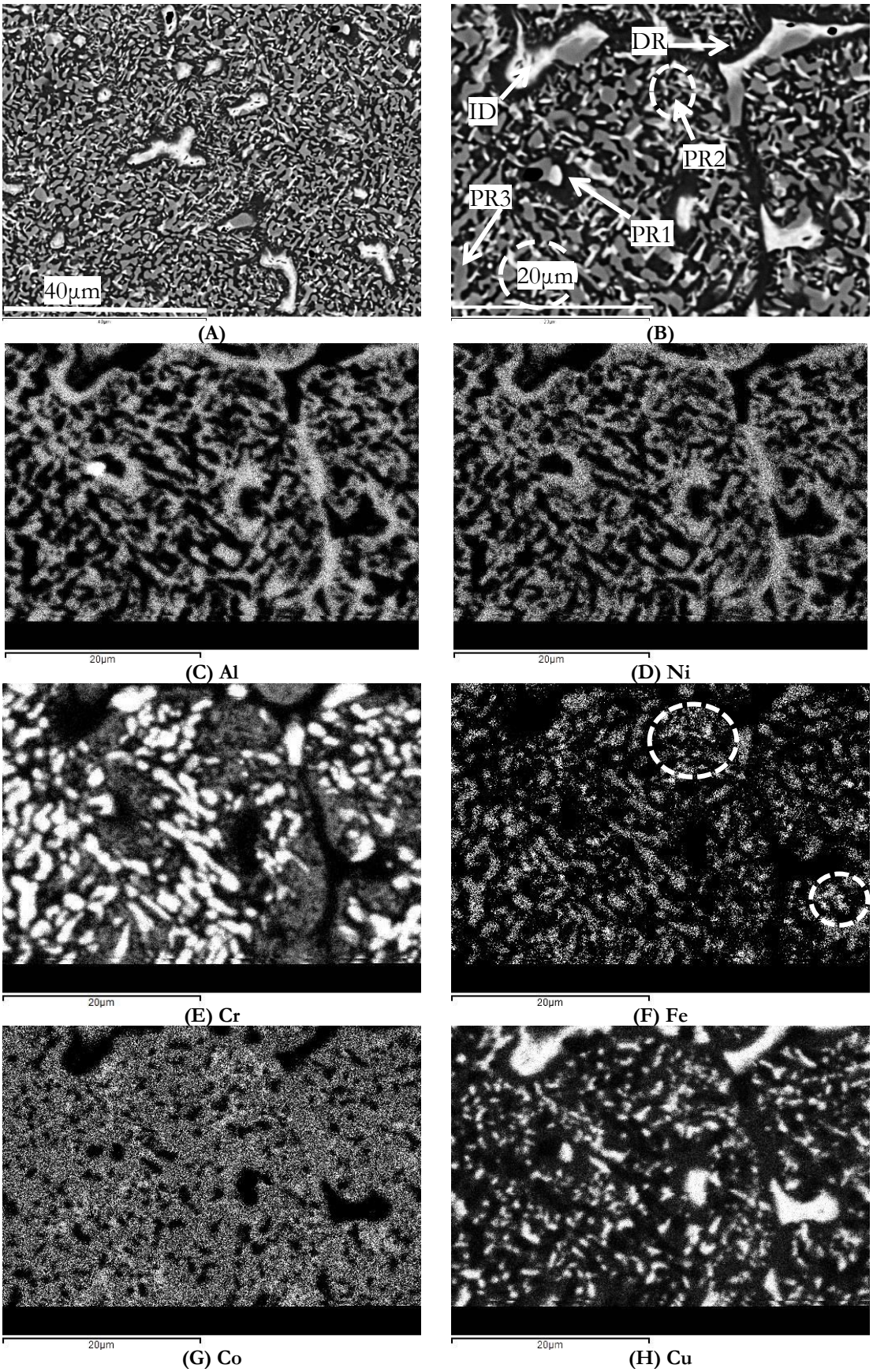

(A) **(B)**

(C) Al **(D) Ni**

(E) Cr **(F) Fe**

(G) Co **(H) Cu**

Fig. 4.13: HEA6 – 700°C /1000H micrographs.
(A): lower magnification; (B): higher magnification; (C-H): EDX elemental maps from image (B)

4.3.2 EDX Microanalysis

PHASE	STATE	Al	Cr	Fe	Co	Ni	Cu
NOMINAL	---	16.7	16.7	16.7	16.7	16.7	16.7
DR	As cast	12.6	21.0	19.8	18.0	16.6	12.1
	1000°C	23.0	9.0	12.3	15.2	25.5	15.0
	850°C	25.5	5.3	12.1	17.2	30.2	9.6
	700°C	25.7	8.0	13.3	18.0	29.9	5.3
ID	As cast	10.0	7.2	8.9	8.0	13.4	52.5
	1000°C	10.2	2.4	4.0	3.9	10.3	69.2
	850°C	7.8	2.0	2.4	3.0	6.6	78.1
	700°C	5.2	1.6	2.4	2.5	4.7	83.6
PR2	1000°C	6.6	24.9	28.7	21.8	12.2	5.9
	850°C	3.3	23.9	34.2	24.8	10.6	3.1
	700°C	*17.0*	*21.1*	*18.1*	*18.2*	*21.1*	*4.5*
PR3	1000°C	4.2	42.7	25.9	17.4	6.8	2.9
	850°C	1.4	48.1	27.0	18.6	4.0	1.0
	700°C	1.9	46.6	27.6	18.5	3.7	1.7
PFZ	As cast	*16.5*	*20.7*	*18.0*	*16.6*	*18.2*	*9.9*
BL	As cast	*19.5*	*11.9*	*14.9*	*15.5*	*20.4*	*17.8*
TRZ	As cast	*7.7*	*17.6*	*19.5*	*16.9*	*15.0*	*23.4*

Table 4.11: EDX microanalysis of the HEA6 samples (at. %).
Data with wider uncertainty are reported in italic font.

Moreover, all the data shown in Table 4.11 are average values of 5 point measurements. Some of the microconstituents were too small to be directly resolved by the EDX probe and they will be discussed in detail in the following paragraphs.

The DRs composition drastically changes from the as cast to the aged conditions. Indeed the aged samples are much richer in Al and Ni and much more depleted in Cr,Fe,Co respect to the as cast. In the aged samples, decreasing the temperature induces a drop of Cr and CU and an increase of Al and Ni. PR1s are too small to be resolved by the EDX probe, but from the maps discussed in the §4.3.1, they are Cu-rich: their formation

happens during cooling , when the temperature goes below the *solvus* line and then the excess Cu precipitates in the DR, as described further.

The ID in the HEA6 exhibits very similar composition and changings with temperature of the ID in the HEA5, like the decrease of Cu content and the rise of other elements with temperature increases. This suggests that they are the same phase.

The PR2 phase is Fe-richer and with similar amounts of Cr and Co. In the 700°C they were too small to be analysed and for this reason an area containing both the DRs and the PR2s was examined. The results obtained are close to an average between the DRs and PR2s of the 850°C sample. Considering that the two DRs have comparable compositions, this could lead to assume that PR2 at 700°C has similar composition of PR2 at 850°C and they are the same phase.

PR3s are extremely rich in Cr, over 45%, and of Fe and Co and they display a significant drop of Al and Cu in the samples aged at 850°C and 700°C.

The areas identified as PFZ, BL and TRZ in the as cast condition are very small and their chemical analysis has to be considered only useful for comparison with the others main microconstituents. Indeed, compared to the as cast DR, the PFZ is Al,Ni-richer and Cu-depleted and the BL is significantly Al,Ni-richer and Cr,Fe-depleted. In comparison with the ID, TRZ is Cr,Fe-richer and Cu-depleted.

The 1000°C aged sample shows again several phases with marked different composition and sharp interfaces, demonstrating that even at high temperatures the contribution of configurational entropy is not enough to suppress phase separation as already observed for the HEA5.

4.3.3 XRD Diffractograms

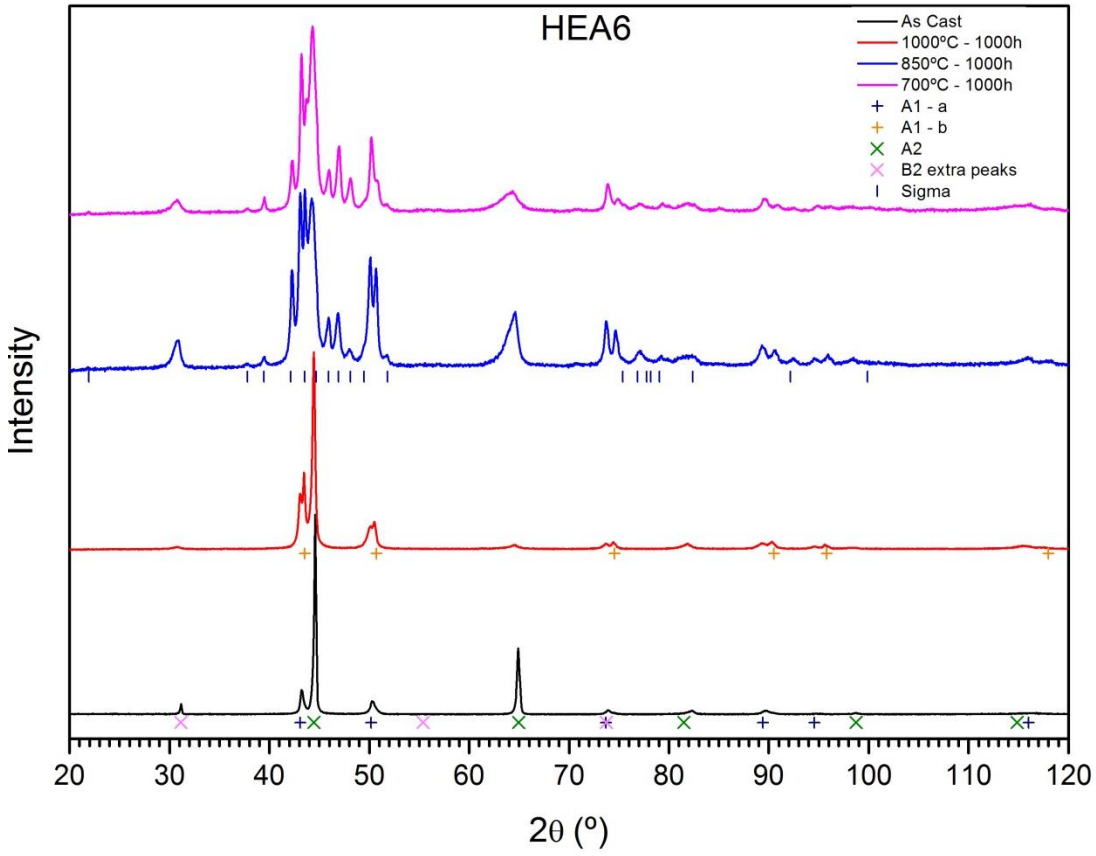

Fig. 4.14: Diffractograms of HEA6 samples

AS CAST CONDITIONS

The sample in the as cast condition is predominantly *bcc* and A1. In Fig. 4.14 the B2 extra peaks are indicated with a different colour but they are on the same pattern of the A2, meaning that the *bcc* phase in the as cast is a B2 phase. Contrary to the micrographs in Fig. 4.9 where many feature were observed, only two phases are clearly detected and there no strong evidence of peak splitting. The magnification of region between 72° and 92° allow to see that the A1 peaks exhibit shoulders that match with a secondary A1. Also the *bbc* at 82°C exhibits a very tiny shoulder on the low angle side. The lattice parameters are shown in Table 4.12.

Considering the EDX data (Table 4.11), probably the DR and the PFZ, that possess similar composition, may have such a similar lattice parameter to be undistinguishable. On the contrary, ID and BL have markedly different composition and then their pattern to be discernible from the others. The measurements of the two A1 lattice parameter has to be considered only approximated since it was difficult to discern the two patterns.

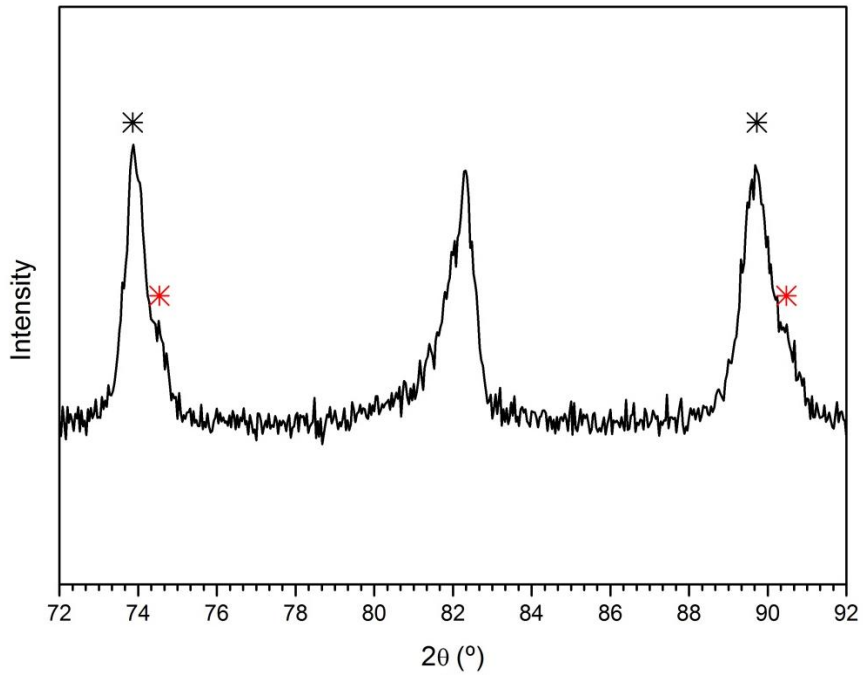

Fig. 4.15: Detail of the HEA6-AS CAST diffractogram. Black=A1 (1). Red=A1 (2)

Phase	Lattice Parameter (Å)
B2	2.874
A1 (1)	3.624
A1 (2)	3.601

Table 4.12: HEA6-AS CAST Lattice parameters

1000°C / 1000H AGED

In the diffractogram of the 1000°C aged sample three very distinct phases are observed, one B2 and two A1. The number of phases here observed is still lower than the number of microconstituents noticed in Fig. 4.11 (four features) This suggests that one phase has to possess and A1 or *bcc* (A2 or B2) structure with similar lattice parameter to the one that are here detected. Contrary to the as cast, the second A1 peaks are here clearly visible and the areas under the respective peaks calculated by a Gaussian fitting in Origin 8.5 are pretty most the same (Table 4.14).

Phase	Lattice Parameter (Å)
B2	2.883
A1 (1)	3.637
A1 (2)	3.606

Table 4.13: HEA6-1000°C/1000H Lattice parameters

	Centre	FWHM	AREA
A1 (1)	73.68721	0.57476	1.52086
A1 (2)	74.47279	0.4201	1.41471
A1 (1)	89.33633	0.56702	2.52734
A1 (2)	90.33979	0.86776	1.93666

Table 4.14: Results on peak fitting at 74° and 90°

850°C / 1000H AGED

Compared to the 1000°C sample, 850°C diffractogram displays strong evidence of σ phase in addition to the previously detected B2 and two A1 phases. The peak fitting performed on the A1 peaks at 74° and 90° reveals that the structure at lower angles (that means with bigger lattice parameter) subtends larger areas, meaning that it has a larger volume fraction in the alloy (Table 4.16). Moreover, the A2 peak at 65° is greatly enlarge respect to the as cast and 1000°C samples. The number of phases detected by XRD matched with the number of microconstituents in the micrographs (Fig. 4.12).

Phase	Lattice Parameter (Å)
B2	2.897
A1(1)	3.634
A1(2)	3.598
Sigma	a=4.563 c=8.810

Table 4.15: HEA6-850°C/1000H Lattice parameters

	Centre	FWHM	AREA
A1 (1)	73.74561	0.41978	9.88008
A1 (2)	74.68253	0.4341	7.67073
A1 (1)	89.39824	0.6438	5.87236
A1 (2)	90.57747	0.54561	3.49705

Table 4.16: Results on peak fitting at 74° and 90°C

700°C / 1000H

The 700°C aged sample is extremely similar to the 850°C one. Again, the number of detected crystal structures fits with the number of the major microstructural constituents. Similar consideration can be taken also for the areas of A1 peaks (Table 4.18).

Phase	Lattice Parameter (Å)
B2	2.891
A1(1)	3.634
A1(2)	3.587
Sigma	a=4.563 c=8.810

Table 4.17: HEA6-700°C/1000H Lattice parameters

	Centre	FWHM	AREA
A1 (1)	73.90055	0.43501	6.2881
A1 (2)	74.90033	0.96965	4.87718
A1 (1)	89.62636	0.61678	3.76134
A1 (2)	90.82923	0.56397	1.25433

Table 4.18: Results on peak fitting at 74°C and 90°C

4.3.4 DSC

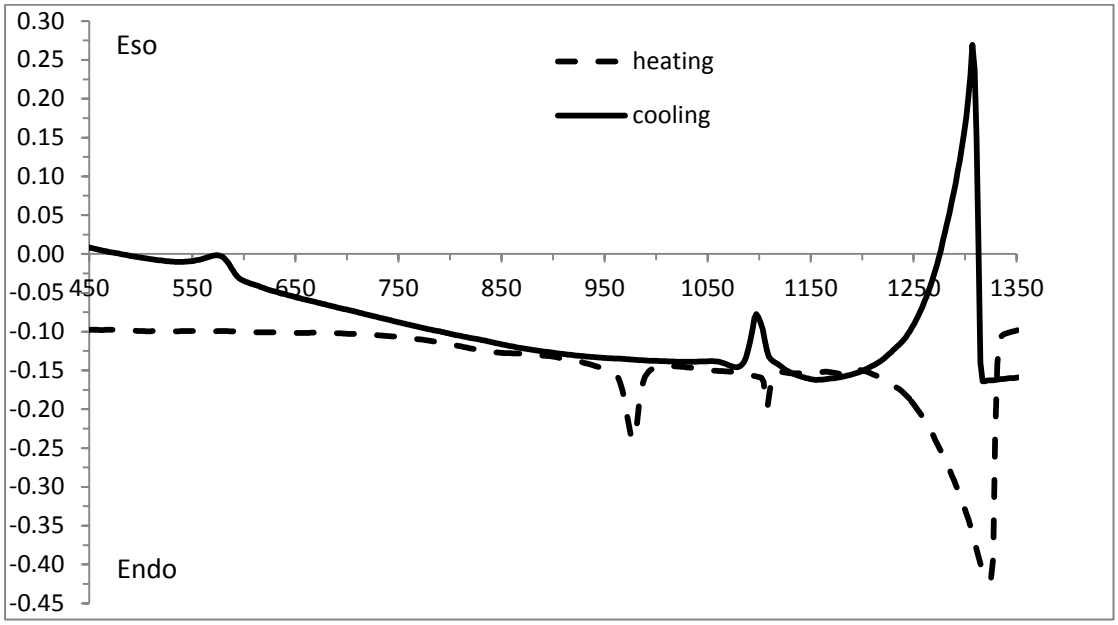

Fig. 4.16: DSC Thermogram of the HEA6-700°C / 1000H.

As for the HEA5, the differential thermal analysis was performed only on the 700°C sample since it is the one that exhibits the more complex microstructure. On the heating curve of Fig. 4.16 a shoulder at around 850°C is observed. As discussed in §4.1.4 for the HEA5, this feature is consistent with a solid state transformation, or better dissolution of precipitates. Since no $L1_2$ precipitates are detected from the XRD, the shoulder is due to continuous changing in volume fraction of σ and the A2.

Besides the shoulder, other three endothermic peaks are displayed. The identification of these peaks is based on the following bases:

- The interdendritic phase is the first ne to melt upon heating and the last one to form on cooling. The contrary happens for the dendrites.
- Both interdentric and dendritic peaks have to be mutually detected in the heating and cooling curve.

For these reason the peak centred at 978°C cannot be assigned to the fusion of the ID. This event indeed corresponds to the peak centred at 1100°C and this is consistent with the ID of the HEA5 (that possesses similar composition, as noted in §4.3.2) and with the ternary diagram shown in Fig. 2.26 [60]. This peak is symmetrically found also in the cooling curve.

Fusion of the DRs is hence attributed to the broad peak centred at 1323°C, slightly below the one observed fort he DR in HEA5. Further discussion will be held in §4.4.1.

The peak centred at 978°C is very sharp and usually these features are due to latent heat absorbed in narrow temperature range in a melting event. But, given the chemical composition of the detected phases, no phase in the alloy is expected to melt at such low temperature. The origin of this peak will be explained in the §4.4.5.

The cooling curve exhibits only two exothermic peaks, easily identified with DR and ID solidification respectively at 1310°C and 1100°C. This is consistent with the as cast microstructure, where no precipitates are observed and ID and DR are the major phases. A small shoulder starting at 1050°C is observed but is very small to be conclusive. One can only notice that it is positioned in a similar rage of the broad peak noted at around 1000°C in HEA5 (§4.1.4), attributed NiAl formation. This may account for the presence of B2 peaks in the as cast.

Significantly no shoulder at 850°C is noticed. Indeed, as stated in §2.3.3, σ does not form on cooling for kinetic reasons. This confirms that the shoulder observed upon cooling at 850°C in the HEA5 is due only to $L1_2$ precipitation.

Finally, the baseline deviation is probably due to substantial precipitations of Cu PR1 in the DR.

4.4 HEA6 – DISCUSSION

4.4.1 Dendrites (DR)

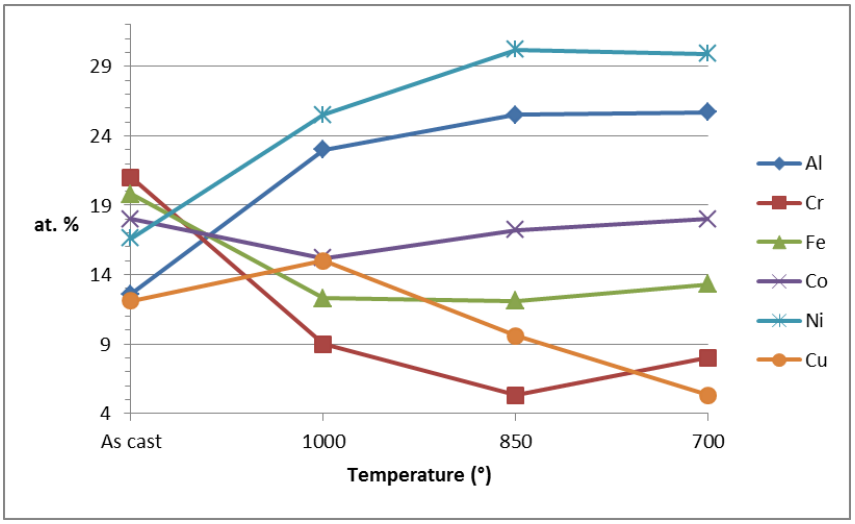

Lattice parameter Å	
As cast	2.874
1000°C	2.883
850°C	2.897
700°C	2.891

Fig. 4.17: Elements content in function of the treatment temperature in the DR and lattice parameters

The as cast diffractogram in Fig. 4.14 shows one B2 and two A1 with extremely similar lattice parameters. The B2 structure cannot be ascribed to the DR (and to the PFZ neither). Indeed no B2 structure with similar composition is shown in the phase diagrams of Cr, Fe, Co, Ni alloys (§2.3), as the DR in the as cast. Especially Cr prevents NiAl B2 formation (§2.3.1). DR in the as cast condition is then an A2 solid solution. In the XRD diffractogram there no evidence of a distinct A2 phase: it is reasonable to suppose that the pattern is overlapped to the B2 since the two phases may possess similar lattice parameter. This hypothesis is confirmed by experimental works [34], [36], [56], [110]. The small shoulder detected on the peak at around 82° in Fig. 4.15 may be a further prove of this overlap. The possibility of solidification as A2 can be predicted looking at the Al,Cr,Ni system. Indeed the AlCrNi phase diagram at 1427°C [66] in Fig. 2.21(a) and the liquidus projection diagram [65] in Fig. 4.18 show that the system solidifies as B2 only in the Al-rich part of the diagram. As noted in §4.3.4, the melting point is slightly lower of the DR in the HEA5. This observation is predicted by the liquidus projection: increasing Al and lowering the Ni amount (as from HEA5 to HEA6) moves the system to solidify as A2+B2 instead of an A1+B2. Al increases also moves the system close to its eutectic point, lowering the melting temperature, as shown also in the vertical projection of Al,

Co and Ni system in Fig. 2.20 [90]. Al amount is however not sufficient to make the alloy solidify as NiAl B2.

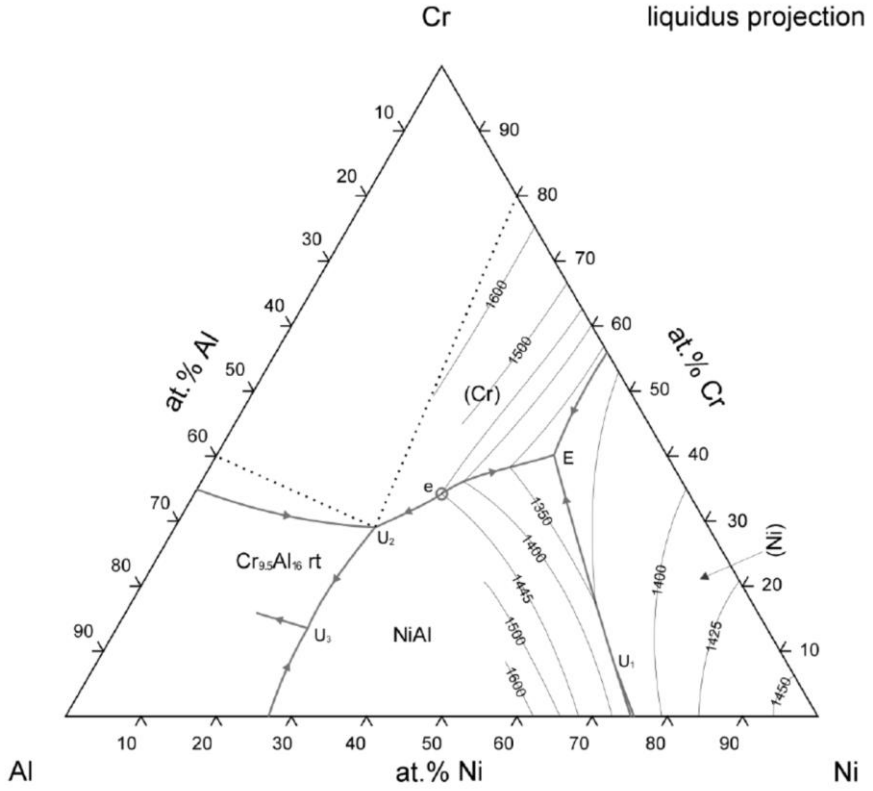

Fig. 4.18: Liquidus projection of the system AlCrNi From ASM APD [56]. Ref. [65]

At lower temperature, like shown in the AlCrNi diagram at 1027°C [66] in Fig. 2.21(b), the A2 is in equilibrium with an A1 (or even $L1_2$) and B2. This means that the DR in the as cast is a metastable A2, retained at room temperature from very high temperatures. Hence, during heating from the as cast, the metastable A2 DR is expected to reject the excess amount of elements leading to the stable phases B2 and A1. This hypothesis provides an explanation to the great compositional change observed between the as cast and the aged samples (Fig. 4.17).

Indeed, contrarily to the as cast, in the aged sample the principal elements in the DR are Al and Ni and, on the contrary, Cr, Fe and Co amounts drop (especially Cr): the composition of the DR in the aged samples meets now the solubility requirements of the NiAl-CoAl-FeAl B2 phase (§2.3.1). The B2 pattern observed in the XRD data of the aged samples is then due to the DR. Moreover, the content of Al and Ni gets lower as treat temperature increases as well as Cr and Cu content increases: this is due to the

enhanced solubility of Cr and Cu in the NiAl phase (§2.3.1), that provokes a reduction of the relative amount of Al and Ni.

As observed also in §4.2.4 about the PR1s and PR2s of HEA5, the non-stoichiometry ratio between Al and (Ni+Fe+Co) is justified by the fact that NiAl B2 is a Berthollide compound and then it tolerates non stoichiometric chemical composition.

Finally, the A1 Cr-Fe-Co based supposed to form in equilibrium with the A2 from the as cast sample, is in turn expected to be in equilibrium with σ. Indeed, the A1 (as discussed for the DR in HEA5 §4.2.1) can dissolve no more than 20-22% of Cr. Furthermore, as it can be seen in the CrFeNi and CoCrNi ternary diagrams in Fig. 2.16 and Fig. 2.17 ([83], [84]), if the amount of Ni available (sequestrated by B2 formation) is less than 10-12% σ formation is facilitated. This will be further explained in the following paragraphs.

4.4.2 As cast DR, PFZ, BL and TRZ

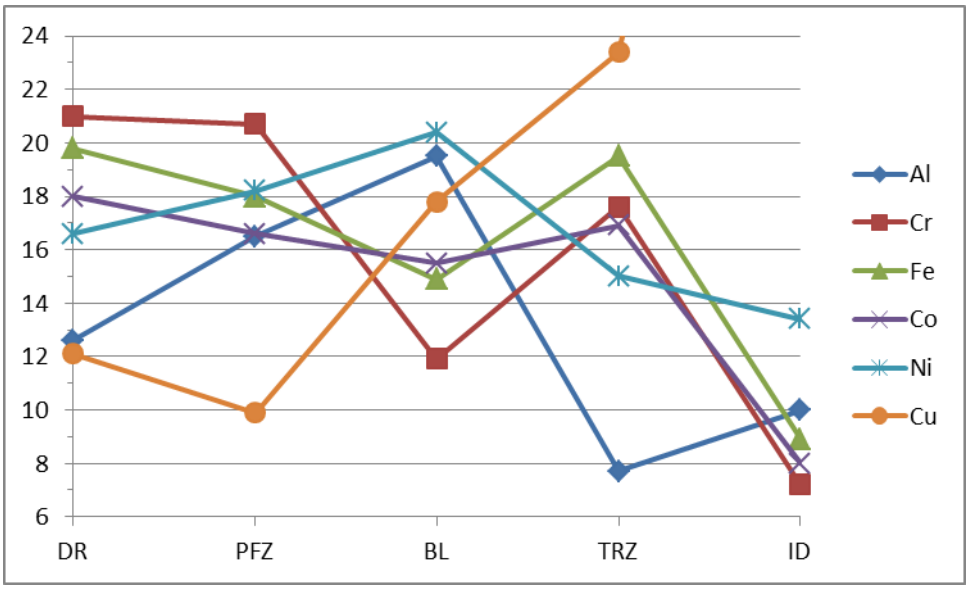

Fig. 4.19: Distribution of elements between the several regions of the as cast sample.

The number of microstructure feature observed in the micrographs of the as cast (Fig. 4.9 and especially Fig. 4.10) is much more than the three phases detected by XRD.

The difference between the DR and the PFZ regards prevalently Al and Cu and on the other hand Cr, Fe and Co remain basically unvaried. As seen in the CrCuFe diagram [96],, Cu solubility limit in the CrFe A2 is very low. During solidification the Cu partitions in the liquid, but if the solidification rate is too elevated it can be remained

trapped in the solidified DR. The PFZ is then the length along which the Cu is effectively expelled from the DR into the liquid phase. For this reason the Cu amount in the PFZ is lower and no Cu-rich PR1 precipitates form. They precipitated in the bulk DR during cooling when the *solvus* line of Cu in the A2 is crossed. This explains the profile of Cu concentration between the different regions shown in Fig. 4.19. Standing these considerations, the PFZ and the DR may possess the same A2 structure with very similar lattice parameter and they are overlapped to the B2 pattern. As well, the PR1 and the ID maybe considered having the same Cu-rich A1 crystal structure (as the HEA5 ID and as demonstrate in the next paragraph).

On the contrary Al (and the correlated Ni) amount increases from the DR to the BL. Because of compositional reason, BL is the only phase in the microstructure that can account for the B2 pattern in the as cast diffractogram. Its formation may be due to the equilibrium between the A2 phase and the B2 during cooling, as stated earlier. The question about in which stage this phase forms, in other words peritectically before ID solidification or after by solid state precipitation, has to be answered with further studies. However, evidence may be the small shoulder observed at cooling at 1060°C in the DSC that mean by precipitation after ID solidification. Formation of and Al,Ni-rich layer at around the dendrites is observed also in a previous work about an alloy with similar composition [31]. Even if it is regarded as A2 and not B2, the formation of the layer is interpreted as related to the equilibrium between the A2, A1 and B2 so that, after solidification, more and more Al and Ni atoms are continuously repelled from the dendrite and accumulated as an Al,Ni-rich layer of along the boundary between dendrite and interdendrite. Also in [46] a layer of Al,Ni-rich is reported to form at the DR boundaries, but in this work it is considered to form during solidification.

Formation of the TRZ may be motivated from the vertical section at Cr=10% of the CrCuFe ternary diagram [111]. Indeed, after the solidification of the DR, the liquid around it is enriched in Cu. The diagram shows that the liquid can solidify primary as an A1 with low amount of Cu and the remained liquid solidifies as A1 Cu-based (ID region). The presence of Ni enhances the solubility of Cu in the first A1. Moreover, the micrographs Fig. 4.11-(E) and (F) reveal that TRZ interfaces are sharp. This feature is typical of peritectic transformations, meaning that TRZ is formed by reaction of DR and liquid and the ID by reaction of TRZ and the last liquid.

This hypothesis implies that the TRZ requires a contact between liquid and it may explain that TRZ does not form where a thicker BL is formed. Indeed, if a continuous film of B2 forms, it prevents the reaction between DR and liquid, blocking TRZ formation. This hypothesis must be validated by further studies. Finally, both the ID and TRZ are A1, possibly with similar lattice [109], [112] and then with overlapped diffraction patterns.

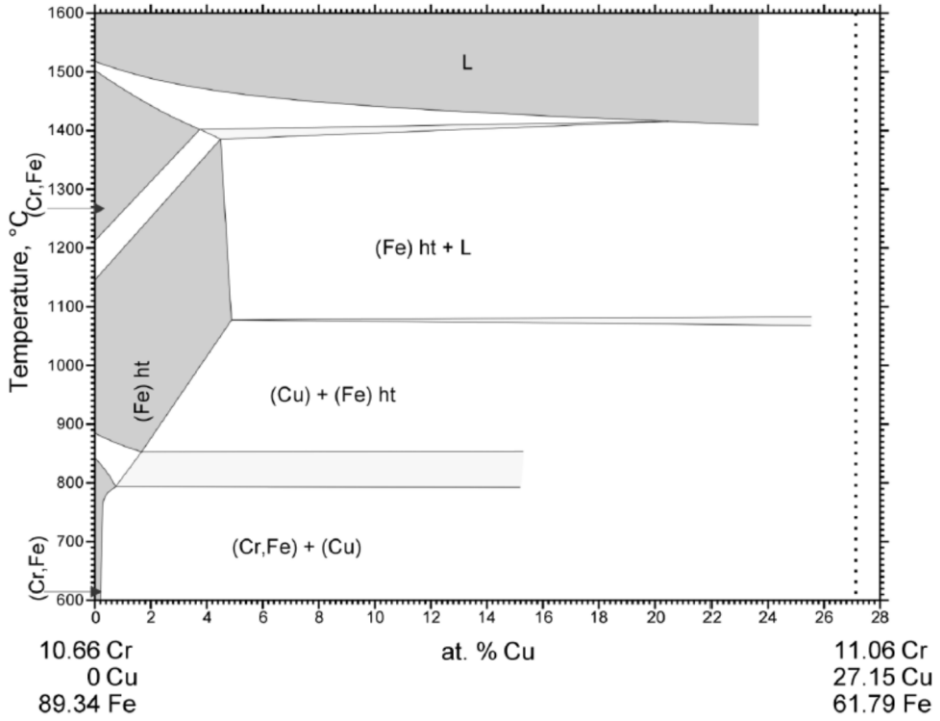

Fig. 4.20: Vertical section of CrCuFe diagram at Cr=10%. From ASM APD [56]. Ref. [111].

4.4.3 Interdentrites (ID)

The ID Cu-rich phase possesses similar composition and similar compositional changes upon heating observed in the HEA5 ID (§4.2.2) so that they can be regarded as the same A1 phase. To assign which one of the two A1 patterns detected in the aged sample belongs to the ID the following considerations are made:

- In the aged samples the second A1 phase has to be the Fe,Cr,Co-rich PR2 precipitates since the PR3s cannot be for compositional reasons;
- In the 850°C and 700°C (especially in the latter), the ID phase has a bigger area fraction respect to the PR2s (as evidently shown by comparison of Fig. 4.13-(F) and (H)). So that the set of peaks subtending the larger areas are probably due to

the ID. The contrary happens in the 1000°C, as evident from Fig. 4.11-(A) and (F) and (H).

- This means that the ID corresponds to the A1 (2) in §4.3.3. The lattice parameters so calculated are in agreement with the values found in the HEA5.

The compositional variations are due to the same phenomena explained in the §4.2.2. Notably no $L1_2$ peaks are detected in HEA6. Given that the two ID are the same in HEA5 and HEA6, this suggests that $L1_2$ has to be ascribed to precipitates in HEA5 DR and not to the ID.

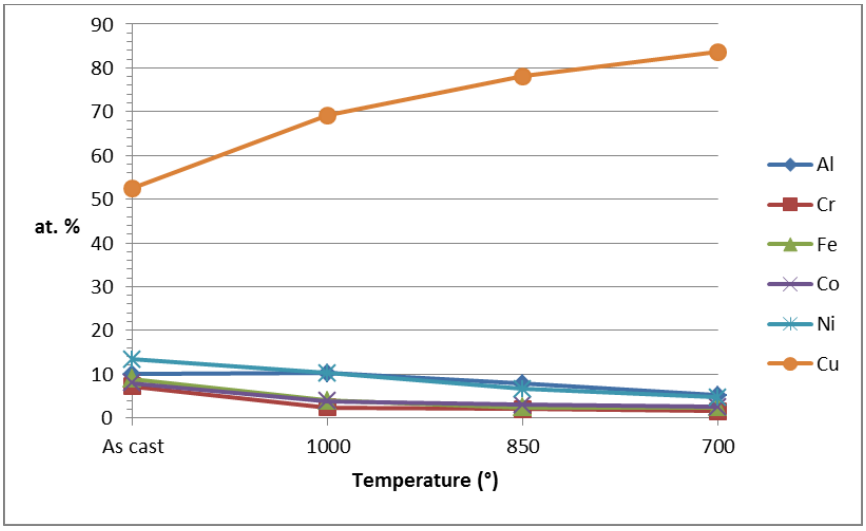

Lattice parameter Å	
As cast	3.601
1000°C	3.606
850°C	3.598
700°C	3.587

Fig. 4.21: Elements content in function of the treatment temperature in the ID and lattice parameters

4.4.4 Precipitates PR2

	Al	Cr	Fe	Co	Ni	Cu	Lattice Parameter Å
1000°C	6.6	24.9	28.7	21.8	12.2	5.9	3.637
850°C	3.3	23.9	34.2	24.8	10.6	3.1	3.598
700°C	*17.0*	*21.1*	*18.1*	*18.2*	*21.1*	*4.5*	3.634

Table 4.19: EDX analysis and lattice parameters of HEA6 precipitates PR2

Accordingly to EDX data and to the review of ternary diagrams of Cr,Fe,Co and Ni systems, PR2s are considered as A1, or better the A1(1) of §4.3.3. Indeed, as discussed in §2.3.4 and shown Fig. 2.16, Ni can stabilise the A1 solid solution even when Ni is down to 10% if Cr does not exceeds 25%. The composition is then consistent with A1 solubility limits already discussed in §2.3.4.

PR2s are present both in the DR that in the ID. They form in the DR because of the equilibrium in AlCrNi (Fig. 2.21 [65]) that leads the A2 of the as cast DR to decompose into B2 and A1. In particular, in the 700°C aged, they are tiny precipitates between the small Cu-rich PR1s, i.e. in a Cu-depleted zone, then favourable to the nucleation of Cr,Fe,Co-rich phase. The large amount of Ni in PR2s stabilises A1 instead of σ, as stated in §2.3.3**.** PR2s nucleates also inside the ID, where in the HEA5 σ phase nucleated. This difference is due to the lower driving force for Al rejection from the ID in HEA6, so that more Al remains in the ID and prevents σ (§2.3.3). The lower driving force is explained by the fact that, notwithstanding ID has the same composition of the HEA5 one, in the HEA6 the DR is richer in Al and then concentration gradient for the expulsion of Al is lower.

Finally, the micrographs in §4.3.1 underlines that the amount of PR2 greatly increased from 700°C to 850°C: increasing temperatures over 700°C provokes a drop of sigma stability in favour of A1 and A2 (§2.3.3).

4.4.5 Precipitates PR3

	Al	Cr	Fe	Co	Ni	Cu	Lattice Parameter Å
1000°C	4.2	42.7	25.9	17.4	6.8	2.9	2.883
850°C	1.4	48.1	27.0	18.6	4.0	1.0	a=4.543 c=8.808
700°C	1.9	46.6	27.6	18.5	3.7	1.7	a=4.543 c=8.808

Table 4.20: EDX analysis and lattice parameters of HEA5 precipitates PR3

The EDX data in Table 4.20 suggest that PR3s are the responsible of the σ phase pattern in the 700°C and 850°C aged samples. Its composition and lattice parameter are comparable with the σ phase detected in HEA5. σ precipitates in the DR are due to the equilibrium previously described that brings the metastable A2 DR in the as cast to decomposes into NiAl B2 plus A1 upon heating from the as cast. The A1 is in turn expected to be in equilibrium with σ phase given the high Cr content, as visible from Fig. 2.16 (if Cr is more than 20% it promotes σ). Moreover, σ gets more stable and preferred to A1 at lower temperatures, as said in §2.3.3. The evolution of σ at the boundaries ID-DR is reasonably due to the transformation of the TRZ in the as cast. Indeed, TRZ was Al depleted, and Cu and Cr which are inclined to separate. The opposite migration of Cr to the ID border grains and of Cu from TRZ to the ID leads to σ. The driving force to

the process is strong given the total immiscibility between Cr and Cu [93] and it allows for the sharp interfaces between σ and the ID.

XRD in Fig. 4.14 shows that at 1000°C σ phase is no more detected. As discussed for the σ in HEA5, it is expected to be thermally suppressed around 1000°C and to evolve into an A2. This is proved by the ternary diagrams CoCrFe [85], AlCoCr [81] and AlCrFe [67] discussed in §2.3.3: at temperature close to 1000°C, in low Co side of the diagram (less than 30%), σ is in equilibrium with A2. This A2 is supposed to have similar lattice parameter of the DR B2 [34], [36], [110] and for this reason its pattern is not discernible in the 1000°C diffractogram. Moreover, this explains the increased Al content in the PR3s at 1000°C. Indeed, contrary to σ, the Cr-based A2 can dissolve bigger amounts of Al (§2.3.5).

The transformation of σ to A2 may account for the peak centred at 978°C in the DSC curve upon heating (Fig. 4.16). The binary diagrams of Cr,Cr an Cr,Fe systems in Fig. 2.14 shows that if σ is close to its stoichiometric composition (in correspondence of the upper temperature limit for the σ formation), then its order-disorder transformation into an A2 takes place congruently in a very narrow temperature range, contrarily to common dissolution/precipitation events. That means that upon heating the σ phase undergoes to volume fraction and composition changing according to the solvus line into the A2 (as shown by the shoulder at 850°C in the DSC). Increasing the temperature, the σ phase gets closer to the stoichiometric composition corresponding to its congruent decomposition into A2. When this point is reached, all the undissolved σ quickly transforms into the A2 and, accordingly to the diagrams, this should take place at a temperature in the between 840°C (CrFe upper limit) and 1282°C (CrCo upper limit), in accordance with the peak position. Moreover, as observed in the micrographs and from the peak intensities, σ phase possesses a large volume fraction in the 700°C aged sample consistent with the big peak at 978°C.

4.5 HEA7 - RESULTS

The High Entropy Alloy no. 7 (HEA7) is Al-rich one, with formula $Al_3CrFeCoNiCu$. The atomic percentage composition is given in Table 4.10.

at.%	Al	Cr	Fe	Co	Ni	Cu
HEA7	37.5	12.5	12.5	12.5	12.5	12.5

Table 4.21: Nominal Chemical Composition of HEA7 (% at.)

4.5.1 Micrographs

AS CAST CONDITION

The microstructure (Fig. 4.22-(A) and in its higher magnification (B)) consists in four different features:

1. Grey dendritic region (DR)
2. White interdendritic region (ID)
3. Grey globular precipitates in the ID region (PR1)
4. Small grey precipitates along the boundaries between DR and ID (PR2)

The dendritic phase is the major one. The BSE images show some contrast within the dendrite which may indicate additional phases. However, there is no corresponding variation discernible from the elemental maps in Fig. 4.22-(C) to (H). The maps display also that:

1. The DR is Cu-depleted and contains all the other elements;
2. The ID is Cu-rich;
3. PR1 are Cr-rich
4. PR2 are too small to be compositionally resolved.

Notwithstanding, PR2 are not clearly resolvable, the close-spaced chains of precipitates made of PR2 appear to be Cr-rich. This suggests that the PR1 are the coarse shape of PR2.

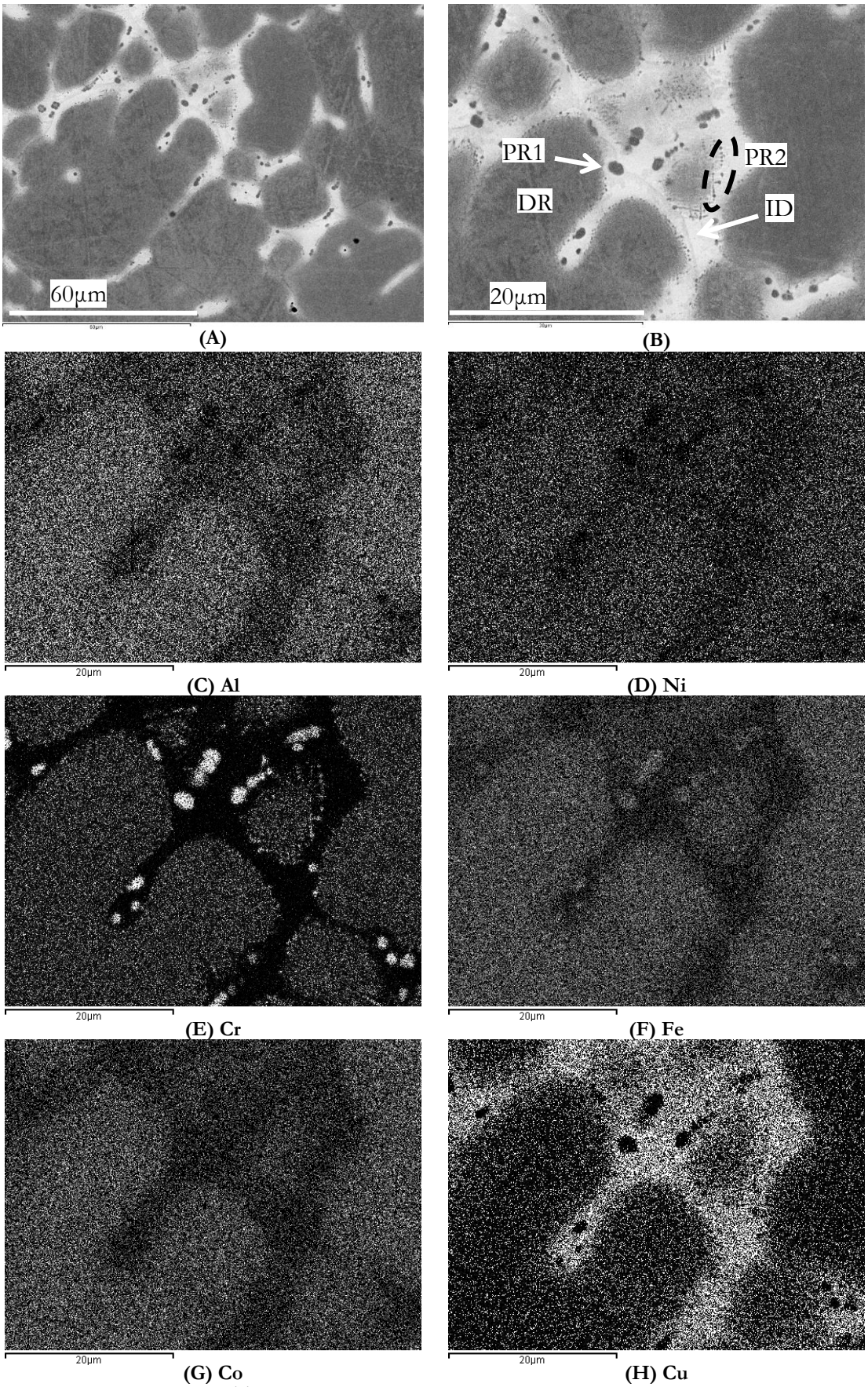

Fig. 4.22: HEA7 – AS CAST micrographs.
(A): lower magnification; (B): higher magnification; (C-H): EDX elemental maps from image (B)

1000°C / 1000H AGED

The micrographs of the 1000°C aged sample exhibits great similarities with the as cast one. Indeed, Fig. 4.23-(A) and (B) show:

1. Grey dendritic region (DR)
2. White small precipitates in the DR (DPR)
3. White interdendritic region (ID)
4. Globular grey precipitates in the ID region (PR1)

Hence, contrarily to the as cast, DPRs appear and the small PR2 disappears. The dendritic phase is still the major one. Moreover PR1 are smaller and with lower volume fraction respect to the as cast. It is evident that, also in the HEA7, phase separation cannot be suppressed by heat treatment since many micrographic regions are still markedly separated even in proximity of liquidus temperature.

The elemental maps (Fig. 4.23-(C) to (H)) show that, as in the as cast:

1. DR is Cu-depleted
2. DRP are Cu-rich
3. ID is Cu-rich
4. PR1 are Cr-rich

The DPR can be regarded as the same phase of the ID given the compositional contrast similarity, as discussed further in §4.6. Moreover the maps reveal that the elements are more homogenously distributed then in the as cast.

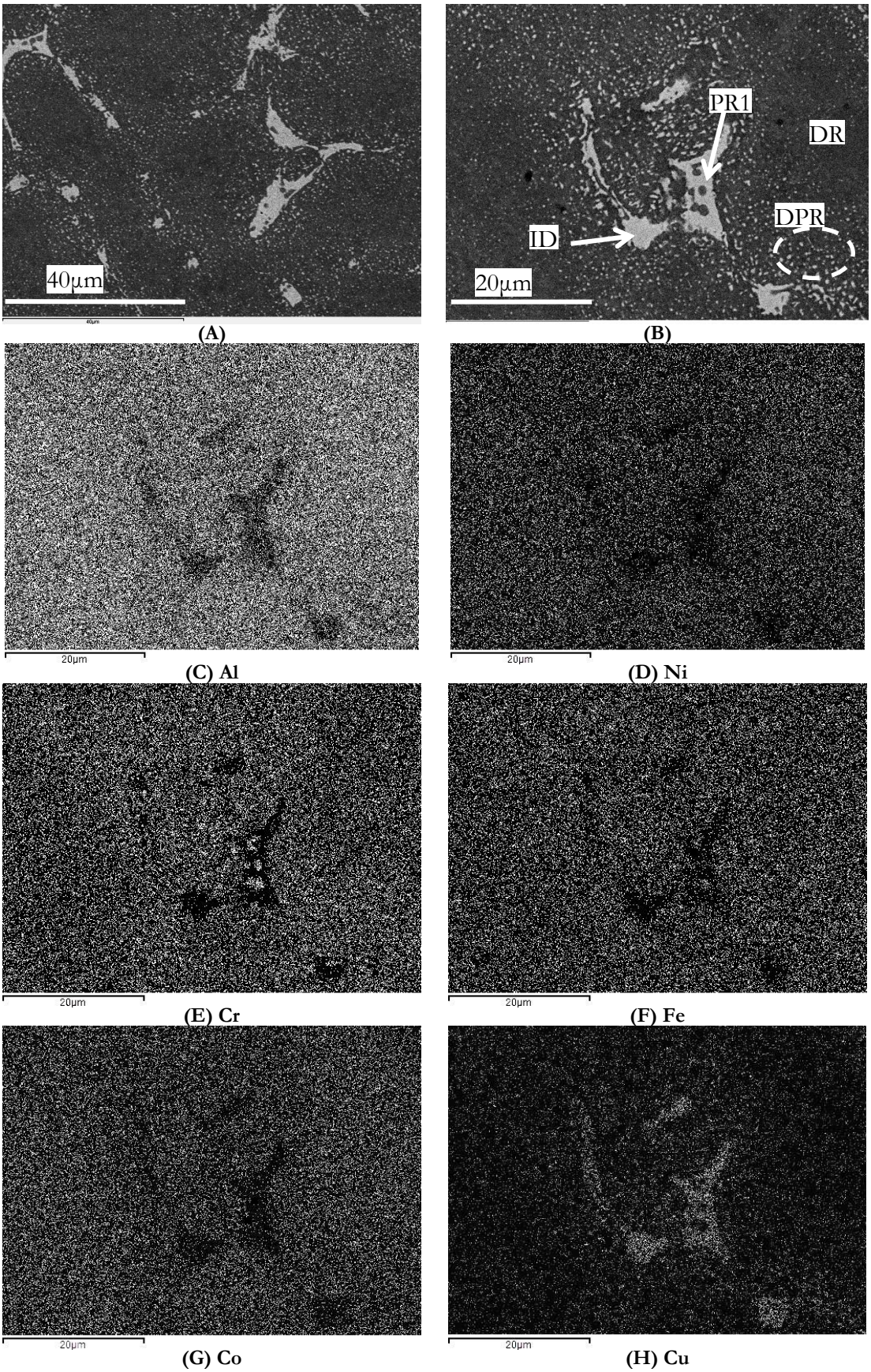

(A) **(B)**

(C) Al **(D) Ni**

(E) Cr **(F) Fe**

(G) Co **(H) Cu**

Fig. 4.23: HEA7 – 1000°C /1000H micrographs.
(A): lower magnification; (B): higher magnification; (C-H): EDX elemental maps from image (B)

850°C / 1000H AGED

The 850°C aged sample has a quite simple microstructure as shown in Fig. 4.24-(A) and (B). Only two microstructure features are discernible:

1. Grey dendritic region (DR)
2. Small round white precipitates in the DR region (PR3).

Remarkably the ID phase does not appear anymore. Moreover from Fig. 4.24-(A) the PR3s are precipitated in chains along the DR grain boundaries. This distribution resembles the one of the PR2 in the as cast condition. Compositional information is provided by the maps:

1. The DR is Al-rich and Cr-depleted;
2. The PR3 are Cr-rich

700°C / 1000H AGED

The 700°C aged microstructure is similar to the previous one. In order to detect the precipitates shown Fig. 4.25-(B) is was necessary to look at the elemental maps, especially the Cr one in Figure (H). The microconstituents are:

1. DR region, Al-rich and Cr-depleted;
2. Irregular shaped globular light grey precipitates (PR3), Cr-rich.

The comparison with the 850°C aged sample with Fig. 4.24 highlights that the PR3s are bigger in this sample and they size and shape distribution are much more irregular. This feature is probably due to the fact that the diffusion is enhanced in the 850°C and allows the PR3 to assume the round shape, minimizing the surface energy of the system by the reduction of the interfacial area with the DR.

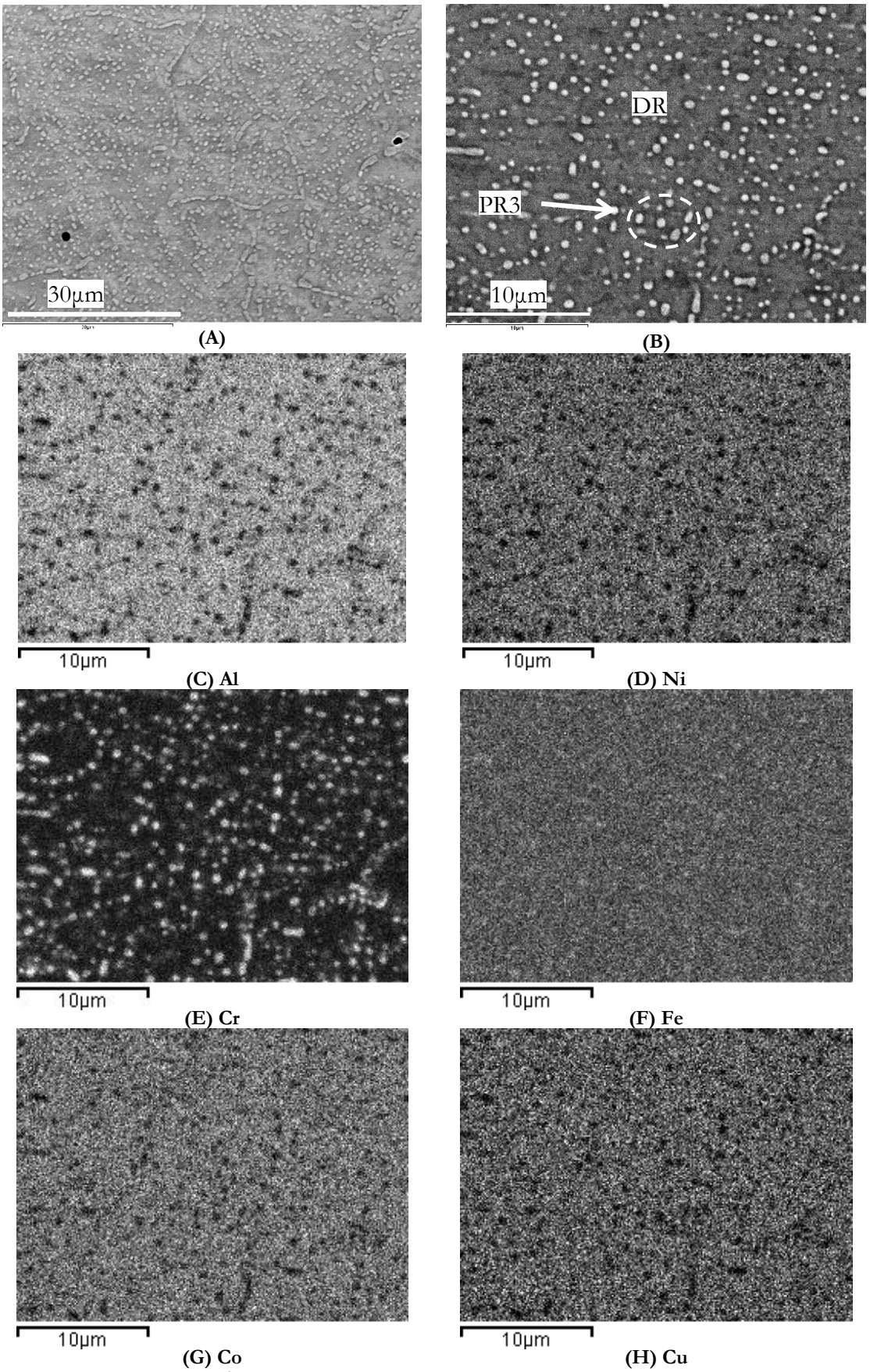

(A) **(B)**

(C) Al **(D) Ni**

(E) Cr **(F) Fe**

(G) Co **(H) Cu**

Fig. 4.24: HEA7 – 850°C /1000H micrographs.
(A): lower magnification; (B): higher magnification; (C-H): EDX elemental maps from image (B)

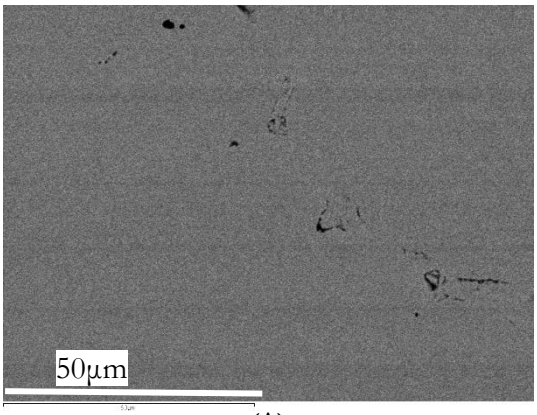

(A)

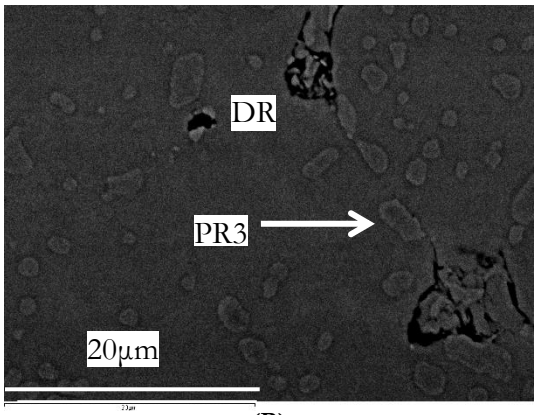

(B)

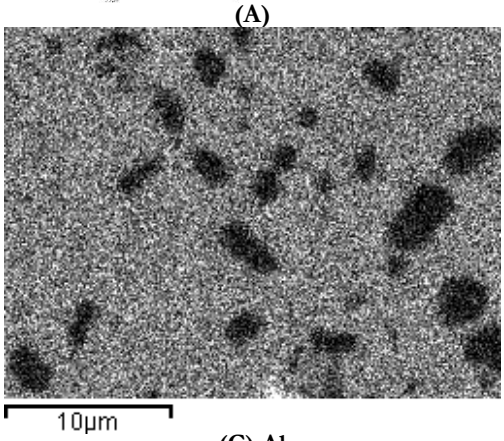

(C) Al

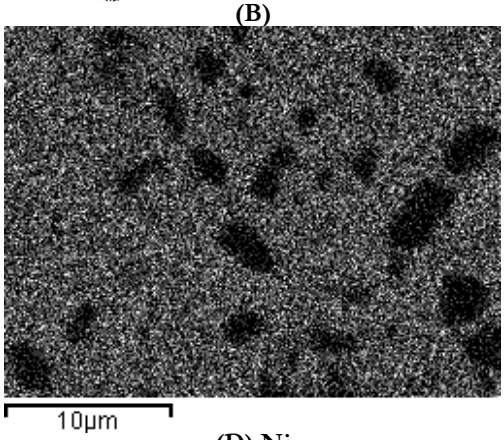

(D) Ni

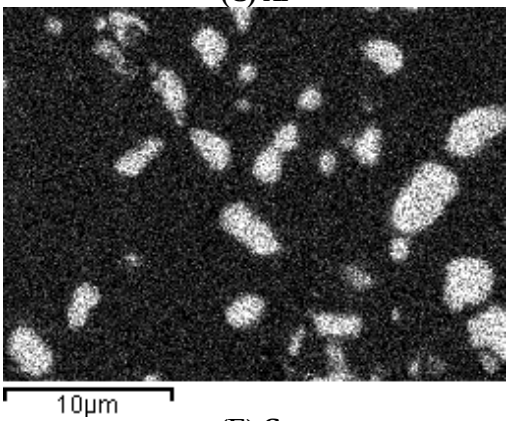

(E) Cr

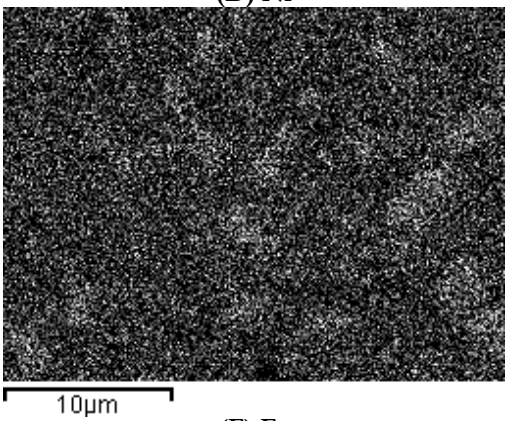

(F) Fe

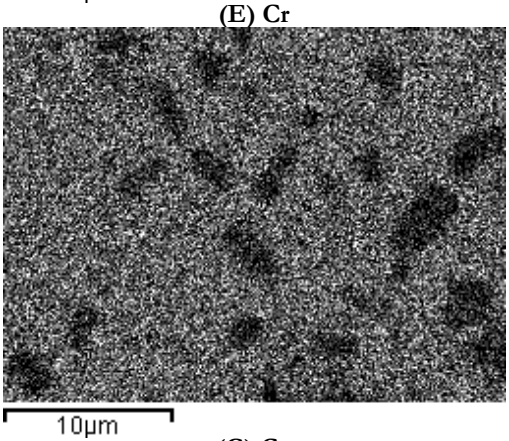

(G) Co

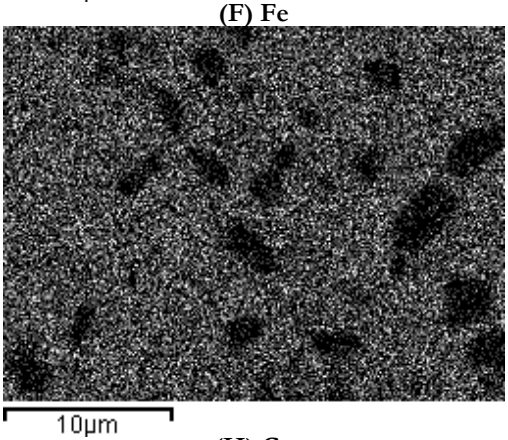

(H) Cu

Fig. 4.25: HEA7 – 700°C /1000H micrographs.
(A): lower magnification; (B): higher magnification; (C-H): EDX elemental maps from image (B)

4.5.2 EDX Microanalysis

PHASE	STATE	Al	Cr	Fe	Co	Ni	Cu
NOMINAL	---	37.5	12.5	12.5	12.5	12.5	12.5
DR	As cast	33.0	14.7	14.2	12.4	12.8	12.9
	1000°C	35.8	14.2	14.6	13.7	13.7	8.0
	850°C	41.2	4.3	11.5	14.7	15.7	12.6
	700°C	38.8	6.5	12.1	13.8	14.5	14.3
ID	As cast	29.5	1.8	4.3	3.7	7.1	53.6
	1000°C	21.9	0.9	1.4	1.4	2.2	72.3
PR1	as cast	16.1	55.1	18.5	3.6	1.7	5.0
	1000°C	14.4	58.3	20.7	3.8	1.3	1.6
PR3	850°C	*30.7*	*26.7*	*16.2*	*10.2*	*9.1*	*7.1*
	700°C	15.3	50.6	19.8	3.5	2.2	8.4

Table 4.22: EDX microanalysis of the HEA7 samples (at. %).
Data with wider uncertainty are reported in italic font.

The composition of the microconstituents (Table 4.22) does not change very much with the several heat treatments. The most significant change regards the major element of each phase, Al in the DR, Cu in the ID, and Cr in the precipitates. The DR in the 850°C and 700°C treated samples is richer in Cu respect to the one in the as cast and 1000°C, according to the fact that the ID Cu rich is no more present and dissolved in the matrix. On the other hand, 850°C and 700°C samples are poorer in Cr and Fe, accordingly to the large amounts of Cr-rich PR3s detected and then segregated out of the DR.

The microanalysis of PR3s in the 850°C was performed considering an area containing both the matrix and the PR3 since the precipitates size was too small. The values are intermediate to the composition of the matrix and of the 700°C aged PR3s, suggesting that they are the same Cr-rich phase.

Notwithstanding PR3s are compositionally very similar to the PR1, except for the larger amount of Cu, they are treated separately because the former appear only in the DR of 850°C and 700°C samples and the latter only in the ID of as cast and 1000°C.

4.5.3 XRD Diffractograms

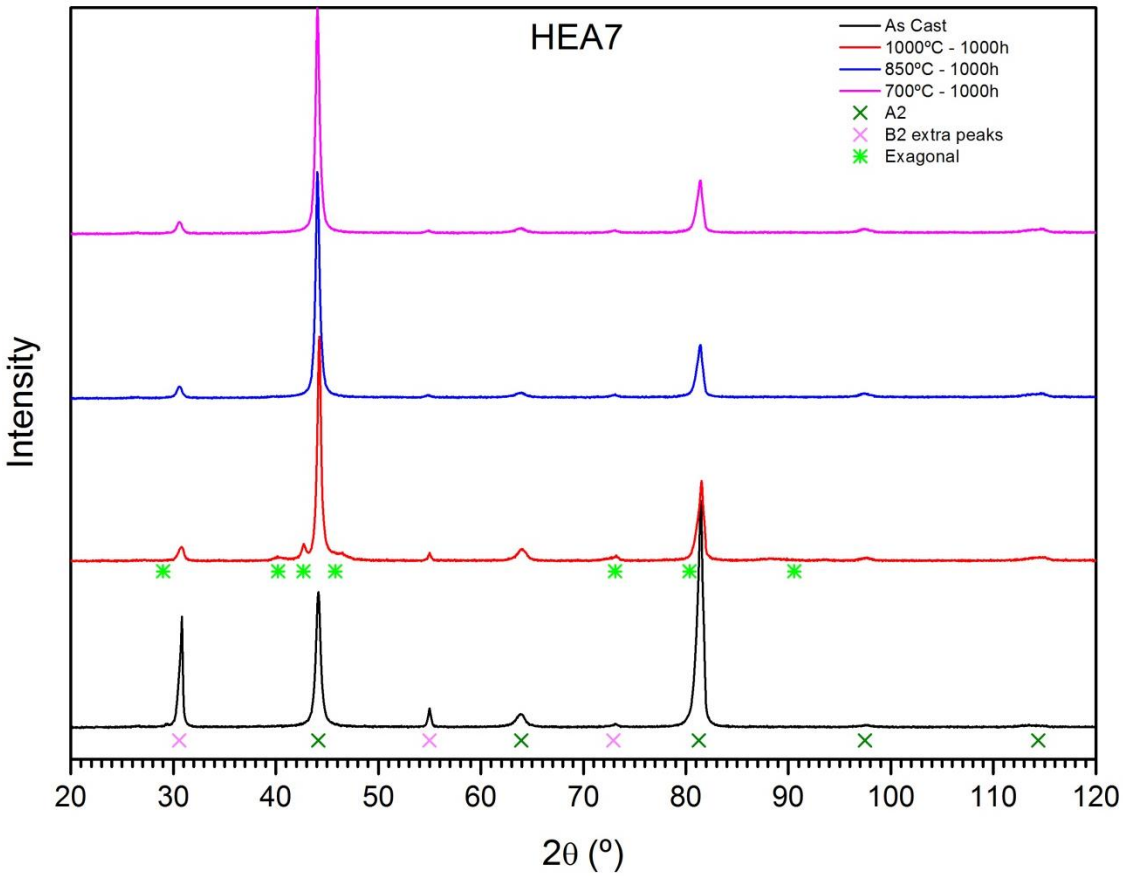

Fig. 4.26: Diffractograms of HEA7 samples

AS CAST CONDITIONS

The diffractogram of the as cast sample in Fig. 4.26 shows only one B2 structure, contrary to the three phase observed in the micrographs. Hence, the phases have to possess a *bcc* crystal structure (B2 and A2) with very similar lattice parameter. Even magnifying the diffractogram, no evidence of peak split or asymmetry was noted. Only a little unidentified peak is present on the left of the major peak at 31°. The calculated lattice parameter is 2.901Å.

1000°C / 1000H AGED

Also in the 1000°C age sample the B2 phase is the dominant one. However, a set of small not easily identifiable peaks are detected and may be assigned to a hexagonal phase. Again the number of phase detected by the XRD is lower of the number of phases noticed in the micrographs and the other phases are supposed to be *bcc* with similar lattice parameter. The estimated lattice parameters are reported in Table 4.23.

Phase	Lattice Parameter (Å)
B2	2.891
Hexagonal	a=5.174 c=4.233

Table 4.23: HEA7-1000°C/1000H Lattice parameters

850°C / 1000H AND 700°C / 1000H AGED

Both the 850°C and 700°C aged samples exhibit only a single B2 pattern and again this does not match the two microstructural features noticed. Hence they may be similar *bcc* structure. No minor peaks can be discerned except for a little broadening of the peaks at high angle values. The calculated lattice parameters of the B2 phase in the 850°C and in the 700°C are respectively 2.895Å and 2.906Å.

4.5.4 DSC

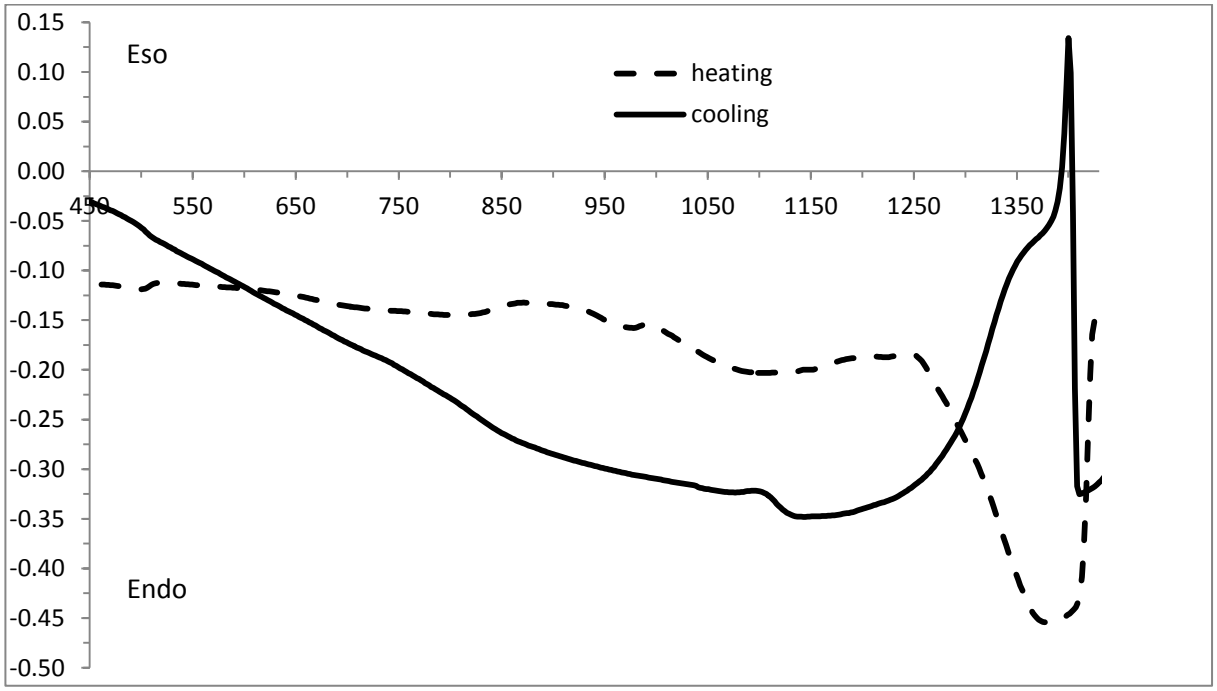

Fig. 4.27: DSC Thermogram of the HEA7-700°C / 1000H.

On the heating curve of Fig. 4.27 a first exothermic peak is shown between 850°C and 950°C. Given the exothermic nature of this peak it may be related to a precipitation event, i.e. the Cu-rich phase. Indeed, the only phase that is not present at temperature below 850°C but only at higher temperature is the Cu-rich ID phase. Then other two endothermic peaks are observed:

- One at higher temperature from 1250°C to 1400°C, due to the DR melting event;
- One wide peak from 1050°C to 1150°C, due to the melting of low melting phase, probably the Cu-rich one, as it will be discussed in §4.6.2.

On the cooling curve two exothermic peaks correspond to the DR and ID solidification events, respectively with the maximum height at 1400°C and 1100°C. In particular the DR solidification exhibits a shoulder on the lower temperature that extends down to 1250°C. These features will be discussed in §4.6.1. Finally a marked deviation of the baseline from the horizontal is evident at temperature below 1050°C. This may be due to the precipitations of the Cr-rich precipitates.

4.6 HEA7 – DISCUSSION

4.6.1 Dendrites (DR)

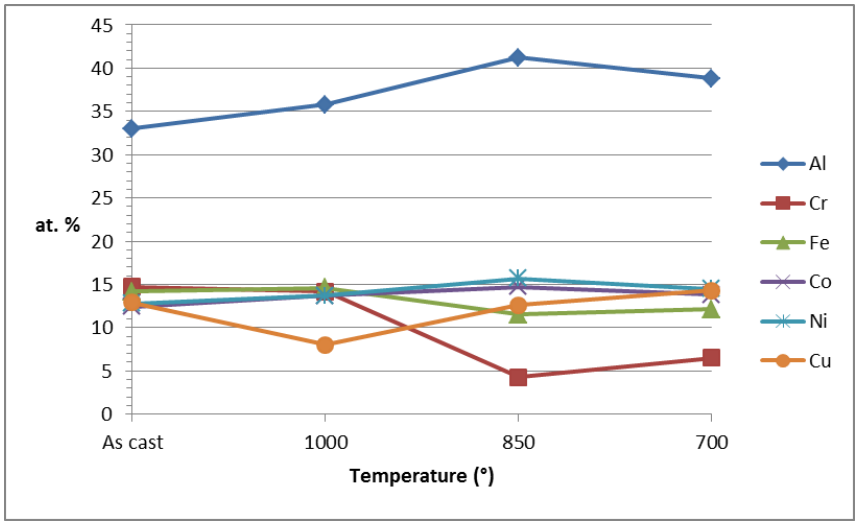

Fig. 4.28: Elements content in function of the treatment temperature in the DR

Given the chemical composition and the evidence of B2 in the diffractogram, the DR is (CoAl,NiAl,FeAl) B2, as also found in previous investigations [38]. Considering the substituting elements (Fe and Co substitute Ni) the stoichiometric composition of NiAl B2 is respected. Also the solubility limits discussed in §2.3.1 are respected. Indeed the Cr content is particularly low and it gets lower from the 1000°C to the 850°C: this is due to

the fact that at 850°C the solubility of Cr in the B2 is expected to be very low (even less that 5%, as shown in the AlCrFe diagram in Fig. 2.8 [67]. This promotes the precipitation of the Cr-rich PR3s in the DR of 850°C and 700°C aged samples. In the DSC the peak due to DR melting and solidification is very broad. The liquidus projection of AlCrNi (Fig. 4.18) shows that for the chemical composition of the HEA7 the alloy solidifies as a B2 because the Al amount is enough, contrarily to the HEA6 (§4.4.1). But the liquidus projection of AlCoCr [82] displays that Cr makes the B2 CoAl melting temperature significantly drop from 1427°C even down to 1227°C. Similarly, the vertical section of the AlCrNi diagrams [65] show that Cr increases make enlarge the NiAl + liquid and then the solidification range is larger (Fig. 4.30). This explains the broad solidification/melting peak of the DR. Moreover the diagram in Fig. 4.30 highlights the low solubility of Cr in NiAl that provokes Cr A2 precipitation in the DR when cooled below 1000°C.

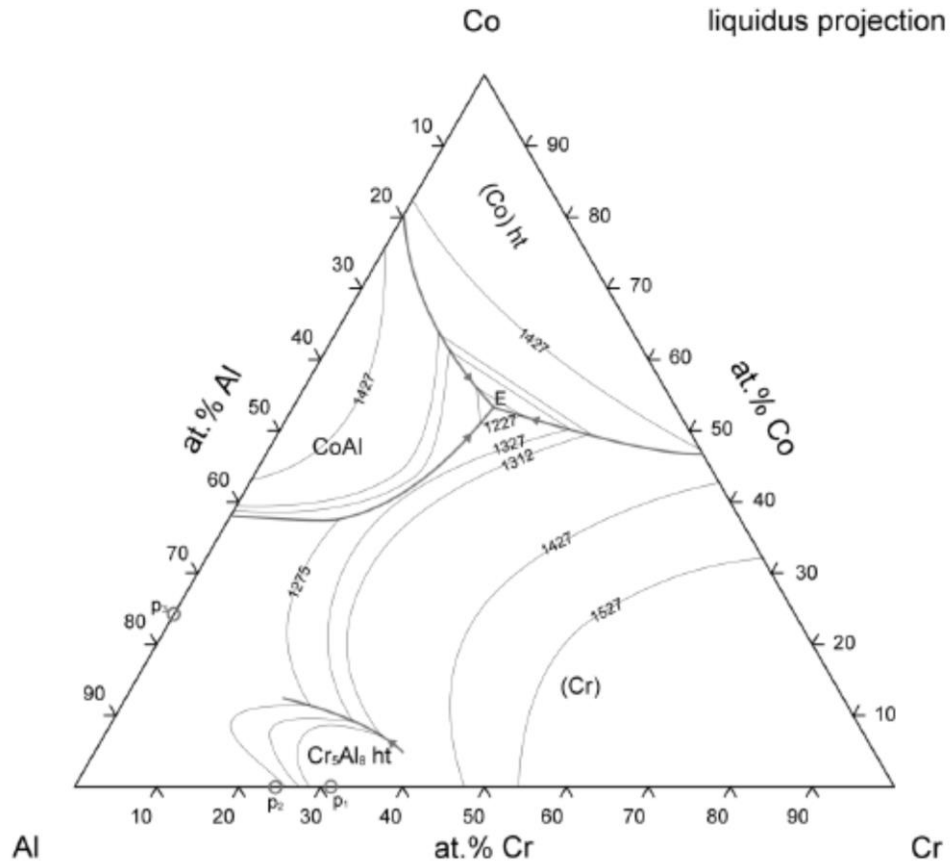

Fig. 4.29: Liquidus projection of the system AlCoCr. From ASM APD [56]. Ref. [82]

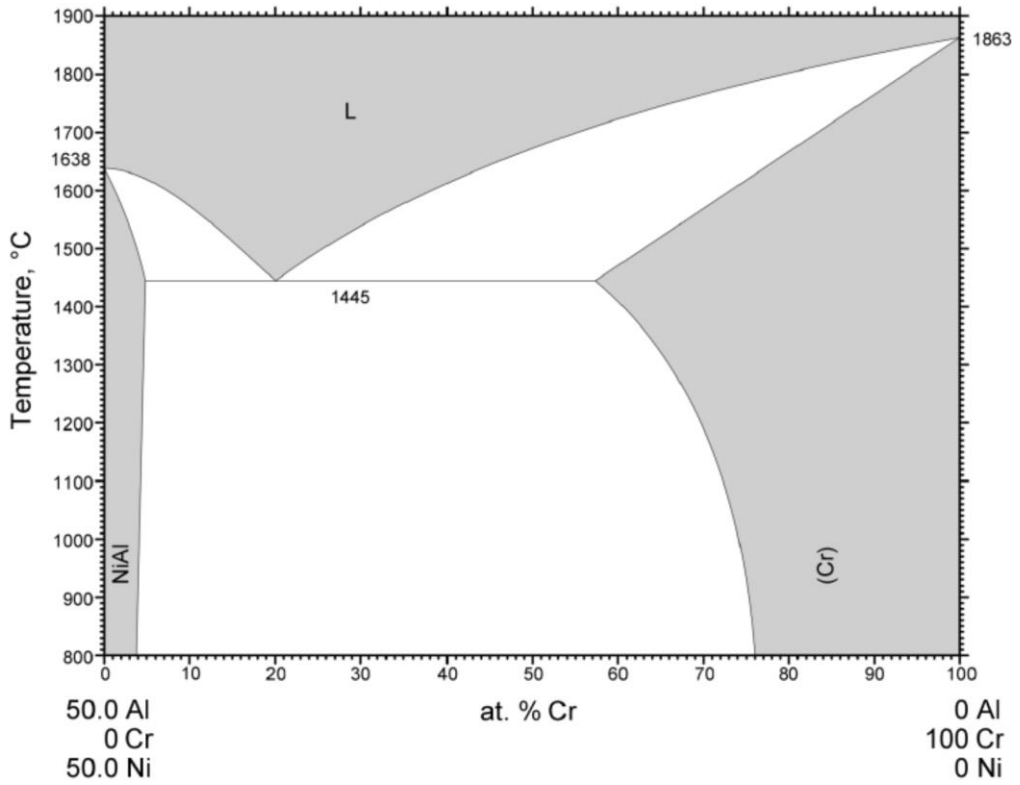

Fig. 4.30: Vertical section of the AlCrNi diagram. From ASM APD [56]. Ref.[65]

4.6.2 Interdentrites (ID)

Considering the EDX data in Table 4.22 and the binary diagram AlCu in Fig. 2.25 [100], ID is identified as $Cu_{0.75}Al_{0.25}$ A2, stable at high temperature. The composition of the ID is in agreement with the solubility limits discussed in §2.3.6. In particular solubility of Cr is very low and this is the reason of Cr-rich PR2 precipitates in the DR and at the grain boundaries in the as cast and 1000°C aged samples. This phase is supposed to possess a lattice parameter very similar to the NiAl B2 and Cr-based A2, i.e. around 2.94Å [102]. This means that the peaks of these three phases are probably overlapped on the same *bcc* XRD pattern.

$Cu_{0.75}Al_{0.25}$ formation in HEA7 is predicted by the liquidus projection of the ternary AlCuNi system [68] in Fig. 4.31: indeed when the Al content is elevated the system solidify as NiAl + $Cu_{0.75}Al_{0.25}$. The melting point of this phase is shown in the binary diagram Al-Cu [100] and it is set at around at 1050°C, accordingly to the peaks assigned to the ID in the DSC thermogram. As considered in §2.3.6 and demonstrated by the ternary diagrams AlCuNi at several temperatures [68], $Cu_{0.75}Al_{0.25}$ field gets smaller decreasing the temperature and it is almost deleted at 600°C. This means that at lower

temperature the alloy is in the B2+A2 field and no more in the B2+ $Cu_{0.75}Al_{0.25}$, as at higher temperatures. This accounts for the fact that in the 850°C and 700°C aged sample no ID phase is detected but PR3 A2 precipitates.

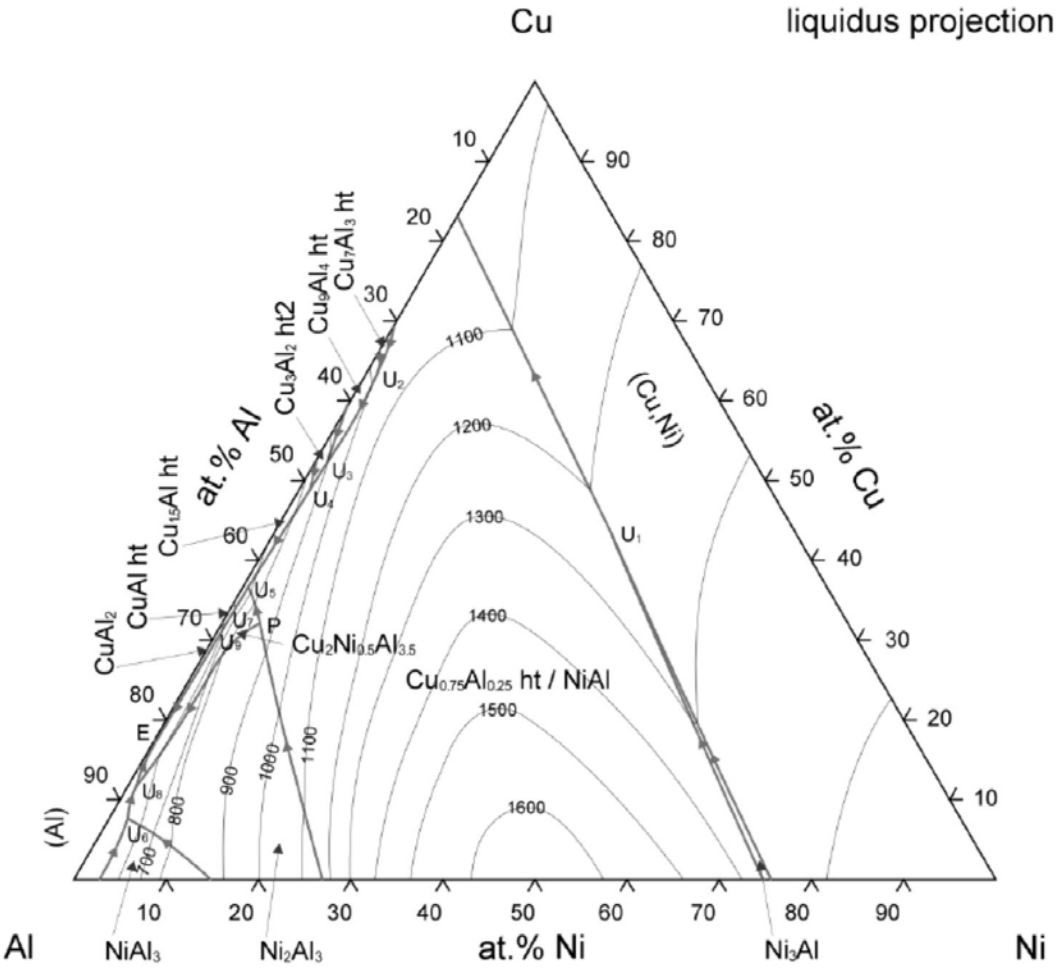

Fig. 4.31: Liquidus projection of the system AlCuNi. From ASM APD [56]. Ref.[68]

4.6.3 Precipitates PR1 and PR3

Combining the dominance of Cr content with the fact that only one *bcc* pattern is shown by XRD, PR1 and PR3 are a Cr-rich A2 solid solution. Moreover, also the small PR2 detected in the as cast can be regarded as the same phase. The Cr-rich A2 possesses a lattice parameter similar to the NiAl and ID, i.e. 2.925Å [1], [110], [31]. Solubility limits have already been discussed in §2.3.5.

These precipitates have a Cr and Fe amount very close to the σ phase detected in the HEA5 and HEA6 but much more Al. This high Al content prevents PR1s and PR3s to be σ since the Al content in HEA7 (37%, nominal) is enough to suppress σ phase, as described in §2.3.3.

The supposed hexagonal phase detected at 1000°C does not match with any hexagonal phase formed by any of the possible ternary system. Further study is required to identify it.

5. CONCLUSIONS

The recent interest in High Entropy Alloys has risen from the possible high temperature phase stability and strength that make these new materials attractive to the aerospace industry. In these alloys the thermodynamic phase stability is ascribed to the configurational entropy change due to the formation of single solid solution. This entropy contribution is supposed to be enough to overwhelm any enthalpy-related push to phase segregation or intermetallic compounds formation and, accordingly to the definition of Gibbs free energy, the higher the temperature, the higher the configurational entropy stabilising effect with regards to the solid solution. This work has explored the phase stability of $Al_xCrFeCoNiCu$ high entropy alloys after 1000 hours long high temperature ageing heat treatment, in order to assess which equilibrium phases form at high temperature and then verify the extent of the configurational entropy stabilising effect. The results of the detected phases for each alloy at each state is summarised in Table 5.1:

	HEA5 $Al_{0.5}CrFeCoNiCu$				
	DR	ID	PRECIPITATES		
AS CAST	Ni,Co,Cr,Fe A1	Cu-rich A1	Ni_3Al $L1_2$	-	-
1000°C	Ni,Co,Cr,Fe A1	Cu-rich A1	Ni_3Al $L1_2$	-	-
850°C	Ni,Co,Cr,Fe A1	Cu-rich A1	Cu-rich A1	NiAl B2	Cr,Co,Fe σ
700°C	Ni,Co,Cr,Fe A1	Cu-rich A1	Ni_3Al $L1_2$	NiAl B2	Cr,Co,Fe σ
	HEA6 AlCrFeCoNiCu				
	DR	ID	PRECIPITATES		
AS CAST	Cr,Fe,Co,Ni A2	Cu-rich A1	Cu-rich A1	NiAl B2	-
1000°C	NiAl B2	Cu-rich A1	-	Cr,Co,Fe A2	Fe,Cr A1
850°C	NiAl B2	Cu-rich A1	Cu-rich A1	Cr,Co,Fe σ	Fe,Cr A1
700°C	NiAl B2	Cu-rich A1	Cu-rich A1	Cr,Co,Fe σ	Fe,Cr A1
	HEA7 $Al_3CrFeCoNiCu$				
	DR	ID	PRECIPITATES		
AS CAST	NiAl B2	$Cu_{0.75}Al_{0.25}$ A2	Cr,Fe A2	-	-
1000°C	NiAl B2	$Cu_{0.75}Al_{0.25}$ A2	Cr,Fe A2	-	-
850°C	NiAl B2	-	Cr,Fe A2	-	-
700°C	NiAl B2	-	Cr,Fe A2	-	-

Table 5.1: Summary of phases detected after each heat treatment in each alloy

The long aging treatment allows diffusion to occur so that the achievement of equilibrium (or near equilibrium) microstructure is assumed after each heat treatment and then frozen at room temperature by a water quenching. The presence of multiple phase and intermetallics was detected in all the samples and they are regarded as the equilibrium phases at the respective soaking temperature. The main features of each alloy are here summarised:

HEA5 $Al_{0.5}$CrFeCoNiCu:

- The dendrite phase is an A1 saturated solid solution based on Ni-Co.
- Segregation of Cu is thermodynamically stable at every temperatures and it is a low-melting phase.
- Precipitation of NiAl and σ intermetallic compounds takes place following heat treatment at 700°C and 850°C in agreement with the solubility limits of Al and Cr in the dendrite and interdendrite regions (§2.3.4 and §2.3.7);
- Ni_3Al precipitation is not kinematically prevented during cooling by the advocated sluggish diffusion.

HEA6 AlCrFeCoNiCu:

- Due to the increased Al content, the dendritic matrix is no longer an A1 solid solution but entirely intermetallic NiAl, even when treated at 1000°C, accordingly to the AlCrNi ternary diagram
- The Cu segregation of is still present and thermodynamically stable
- Precipitation of σ phase and A1 Fe,Cr-rich precipitates happens according to solubility limits described in the ternary diagrams AlNiX (§2.3.1).

HEA7 Al3CrFeCoNiCu:

- Al content of is sufficient to ensure the solubility of Cu in the NiAl intermetallic matrix intermetallic at intermediate temperatures. However, at 1000°C the A2 phase $Cu_{0.75}Al_{0.25}$ stable at high temperatures segregates from the matrix (§2.3.6).
- σ phase precipitation of is prevented by the high Al content (§2.3.3). However, formation of A2 Cr,Fe-rich precipitates takes place as predicted by limits of solubility of Cr and Fe in NiAl (§2.3.1).

These evidences lead to conclude that:

1. Even at the highest temperature the configurational entropy is not sufficient to counterbalance the tendency to segregation due to the positive mixing enthalpy between Cr-Cu and Fe-Cu that induces Cu partitioning into the interdendrite regions. This phase segregation is thermodynamically stable and is not eliminable by heat treatment, contrarily to other structural metal systems. Indeed steels, Ni-based superalloys and titanium alloys are all homogenised in a single solid solution phase in order to eliminate casting-induced micro-segregation. Since this is not possible in $Al_xCrFeCoNiCu$ HEAs, their microstructural control is challenging.
2. Moreover, phase separation prevents formation of single near equiatomic solid solution, corresponding to the maximum of configurational entropy (all the elements mixed in near-equimolar ratio). This means that partitioning of elements in multiple phases drastically reduces the configuration entropy of each of them. Hence, their stability against intermetallic formation is reduced. For these reasons, except for the HEA5 - 1000°C, where the $L1_2$ precipitates are likely formed during cooling, intermetallics are found in all the samples and they are formed also at higher temperature. Hence, the thermodynamic impossibility to have a single solid solution in $Al_xCrFeCoNiCu$ involves the lowering of configurational entropy and then the higher stability of intermetallics against solid solutions. Furthermore, increasing Al content, the system is shifted from an A1+B2 field (Al=0.5) to an A2+B2 field (Al=1) to a B2 (Al=3) field, so that for high Al content the alloy solidifies as NiAl intermetallic and the main phase is intermetallic.
3. Additionally, the results of this study demonstrate that the possibility to create single simple solid solution by mixing five or more elements is not given by the configurational entropy only (i.e. increasing the number of elements). Single solid solution may be promoted when the constituent elements show extended solid solutions and no intermetallics in their binary and ternary diagrams. Indeed, the occurrence of extended single solid solution fields in the binary and ternary diagrams means that the elements are prone to form close-to-ideal solid solutions with low positive mixing enthalpies that can be counteracted by the increased configurational entropy. Moreover our study highlights that the phase separation

and intermetallic formation in $Al_xCrFeCoNiCu$ HEAs can be predicted by the analysis of conventional ternary diagrams, demonstrating that conventional metallurgy still dominates HEAs phase stability. For example, segregation of Cu, formation of σ, formation of NiAl and the effect of Al on resulting crystal structure are contemplated in the ternary diagrams.

4. Hence, microstructure is not controlled by the configurational entropy maximisation but by the minimization of the total Gibbs free energy, including both enthalpy and entropy (not only configurational, but also electronic, magnetic) contributions. Consequently, the energy reduction of the system is achieved through precipitation of intermetallic compounds and formation of separate solid solution phases, as demonstrated by the equilibrium microstructures observed after the 1000°C aging treatments.
5. Moreover intermetallic and phase separation are found in the as cast condition. This casts doubts also on the kinetic stabilisation of single solid solution. Indeed, the advocated sluggish diffusion in the HEAs should allow to prevent long range diffusion and phase separation even at lower temperature, where the configurational entropy effect is reduced. Hence the presence of intermetallics in the as cast sample after air cooling means that the diffusion is not sluggish enough to prevent phase decomposition. Alternatively, it could mean that even at close-to-*liquidus* temperatures the entropy effect is not sufficient and multiple phase and intermetallic are present.

Conclusively, all these findings suggest that in $Al_xCrFeCoNiCu$ HEAs the configurational entropy effect does not play an effective stabilisation role against microstructural evolution upon heating. The ineradicable Cu segregation, melting at about 1150°C, prohibits the employment of these alloys for high temperature components in gas turbine engines. Moreover, extended formation of brittle intermetallics makes HEAs microstructure control and processing very challenging and they cannot be regarded as materials suitable for high temperature applications.

6. SUMMARY - ITALIANO

6.1 INTRODUZIONE

Si definiscono Leghe ad alta entropia leghe metalliche "costituite da cinque o più elementi in rapporti quasi equimolari. Al fine di estendere le possibilità di alligazione, le HEAs possono contenere elementi principali ciascuno con concentrazione tra il 35 e 5 at.%. Vasti studi hanno condotto a numerosi sistemi in grado di dare origine a singole soluzioni solide con struttura cristallina semplice (ccc o cfc)" Yeh *et al.* (2004) [1].

La proprietà di dare luogo a singole soluzioni solide è la caratteristica distintiva di questi sistemi. Infatti, coerentemente alle nozioni derivanti dalla metallurgia fisica e dai diagrammi di fase, l'alligazione di numerosi elementi in rapporti quasi-equimolari è ritenuta dare luogo a molteplici composti intermetallici. La soppressione dei composti intermetallici è stata razionalizzata da Yeh *et al.* [1] ricorrendo all'ipotesi che l'aumento di entropia configurazionale per la formazione di un'unica soluzione solida controbilanci l'entalpia di formazione dei composti intermetallici. In questa teoria l'entropia configurazionale è ritenuta sufficiente a stabilizzare la soluzione solida contro gli intermetallici abbassando l'energia libera di Gibbs. Come più dettagliatamente spiegato in §2.1.1, il valore dell'entropia configurazionale è il contributo entropico dominante nella creazione di una soluzione solida ed è legato al numero degli elementi alliganti tramite l'equazione di Boltzmann (Eq. 2.2).

$$\Delta S_{conf} = -k \ln \omega = R \ln n \qquad \textbf{Eq. 2.2}$$

Considerando rispettivamente 3, 5 e 6 elementi il valore dell'entropia configurazionale assume valori rispettivamente pari a 1.10R, 1.61R e 1.79R, da considerarsi elevati dato che la variazione di entropia durante la fusione è approssimativamente pari R in accordo alle legge di Richards [27]. Tali valori del contributo entropico all'energia libera di formazione della soluzione solida sono ritenuti sufficienti a controbilanciare i contributi entalpici ed entropici non configurazionali (ovvero magnetici ed elettronici) all'energia libera di formazione dei composti intermetallici. L'entropia configurazionale dunque abbassa l'energia libera di Gibbs della soluzione solida rispetto dell'energia libera di Gibbs di formazione dei composti intermetallici e fornisce dunque una stabilizzazione

termodinamica alla soluzione solida. Inoltre, in modo analogo, il contributo entropico configurazionale dovrebbe vincere eventuali contributi entalpici positivi che porterebbero alla segregazione di fase, consentendo così la creazione di soluzioni solide anche tra elementi che secondo le convenzionali regole di Hume-Rothery [17] non sono tra loro miscibili allo stato solido.

Da tali considerazioni derivano interessanti proprietà documentate da diversi studi [1], [3], [4], [8], [9]:

1. Stabilità di fase:
   Per definizione di energia libera di Gibbs, il contributo stabilizzante dell'entropia configurazionale è accresciuto elevando la temperatura. Queste leghe sono dunque ritenute possedere stabilità di fase crescente con la temperatura. Inoltre, a temperature minori, benché tale contributo sia ridotto, le eventuali trasformazioni di fase e segregazioni sono impedite dalla diffusione lenta in una matrice priva di un elemento principale;
2. Microstruttura ultrafine:
   L'assenza di una matrice con un elemento principale riduce drasticamente la velocità di diffusione a lungo raggio in modo che il tasso di crescita sia fortemente ridotto e favorendo la nucleazioni di numerosi grani;
3. Alta resistenza:
   Mancando un elemento matrice, tutti gli atomi hanno ruolo di soluto conferendo esteso rafforzamento per alligazione, accresciuto dalla grana nanometrica;
4. Durezza a caldo:
   L'esteso effetto di rafforzamento per alligazione e la ridotta mobilità delle vacanze nella matrice priva di elemento principale contribuiscono a ridurre il fenomeno del creep;
5. Resistenza alla corrosione e resistenza all'ossidazione ad alte temperature fino a 1100°C.

Tali promettenti proprietà hanno suscitato ampio interesse da parte della comunità scientifica date le potenzialità come candidati materiali per impieghi ad alta temperatura, specialmente in ambito della propulsione aerospaziale. In particolare, leghe basate sul sistema $Al_xCrFeCoNiCu$ sono state ampiamente studiate poiché impiegano elementi

costituenti le superleghe a base Ni, attualmente adottate nei componenti ad alta temperatura delle turbine a gas dei motori aeronautici.

Tuttavia, diversi studi condotti recentemente anche presso il Rolls-Royce UTC, Department of Materials Science & Metallurgy (University of Cambridge) dal Dott. Nicholas Jones *et al.* [13] hanno lanciato dei dubbi circa l'estensione della stabilizzazione fornita dall'entropia configurazionale. Sono tre i principali apporti agli interrogativi sorti circa l'effettiva capacità di formare singole soluzioni solide da parte delle HEAs:

1. Imprecisioni nell'interpretazione di diffrattogrammi XRD con evidenti picchi dovuti alle riflessioni da super-reticolo di composti intermetallici, come discusso in §2.1.3 ([1], [2], [8], [9], [31]–[33]).
2. Trasformazioni di fase e precipitazione di composti intermetallici sono stati osservati dopo trattamenti termici ad alta temperatura medio-brevi (72 ore) [6] o trattamenti termo-meccanici [12].
3. L'utilizzo di molti elementi in rapporti quasi equimolari non è condizione sufficiente a garantire singole soluzioni solide.

Il punto 1) è dovuto al fatto che le strutture intermetalliche danno origine a *pattern* di diffrazione diversi da quelli della struttura di "origine". Si deve ricordare che in un sistema di due metalli A e B la tendenza alla formazione di un composto intermetallico si ha se la creazione di legami A-B è favorita rispetto a quella di legami A-A e B-B (entalpia di miscelazione negativa). Tale condizione fa sì che gli atomi A e B si dispongano gli uni attorno agli altri in modo da massimizzare tali interazioni cosicché, contrariamente ad una soluzione solida ideale, le posizioni reticolari non sono più equivalenti. Dunque, gli atomi A e B occupano rispettivamente precise posizioni nella cella (es.: gli spigoli o il centro del cubo in una struttura cubica a corpo centrato, *ccc*), come mostrato in Fig. 2.3. Il reticolo cristallino di un intermetallico *ccc* (B2) è dunque diverso da quello di una soluzione solida *ccc* (A2) in quanto il primo è in realtà costituito dalla sovrapposizione di un reticolo A e un reticolo B (super-reticolo). Questa sovrapposizione fa sì che il motivo che si ripete nello spazio non sia più quello "originario" ma uno nuovo: questo cambiamento permette ad un intermetallico B2 di dare luogo riflessioni alla Bragg per famiglie di piani (es: {100}) altrimenti proibite per una soluzione solida A2, benché entrambe abbiano una cella di base cubica a corpo centrato.

Il punto 2) deriva da alcuni studi che hanno evidenziato la presenza di composti intermetallici o dopo trattamenti relativamente di invecchiamento ad alta temperatura o dopo trattamenti termici prolungati ma a seguito di deformazione plastica impartita al campione [12]. Benché sia evidente che la struttura evolva in seno al trattamento impartito, tali studi senz'altro alzano dubbi circa l'effetto stabilizzante dell'entropia configurazionale senza però stabilire univocamente se le strutture ottenute sono quelle d'equilibrio. Infatti in questi studi non è possibile aver certezza che il tempo di invecchiamento sia sufficiente a consentire al processo di diffusione di avvenire completamente fino a raggiungimento dell' equilibrio termodinamico o non è possibile separare effetti termomeccanici da processi puramente termodinamici.

Il punto 3) è frutto di ampio studio condotto da Otto *et al.* (2013) [14] il quale dimostra che la formazione di singole soluzioni solide in sistemi contenti 5 o più elementi si ottiene solo combinando tra loro elementi che considerati in coppia mostrano nei loro digrammi binari ampi campi di completa miscibilità allo stato solido, ovvero ridotto discostamento dalle condizioni di idealità. Infatti solo per piccoli scostamenti il contributo dato dall'entropia configurazionale può controbilanciare i contributi entalpici alla formazione di composti intermetallici. Inoltre, in caso contrario, i precipitati intermetallici che si formano sono gli stessi previsti dai rispettivi diagrammi binari. Anche Senkov *et al.* (2013) [15] hanno dimostrato la validità di questo criterio mettendo appunto alcune HEA basate su metalli refrattari con ampi campi di soluzioni solide quando alligati in coppia (W,Nb,Ta,W,V), comprovando così che l'elevato numero di costituenti non è condizione sufficiente alla creazione di soluzione solide ma che sussiste una correlazione con i diagrammi di fase binari.

6.2 SCOPO E PROGRAMMA DI INDAGINE

Il presente lavoro si prefigge lo scopo di indagare la stabilità di fase di leghe ad alta entropia del sistema $Al_xCrFeCoNiCu$ dopo esposizione a trattamenti termici prolungati di 1000h ad alta temperatura al fine di valutare l'adeguatezza di tali materiali per applicazioni ad alta temperatura. Inoltre ci si prefigge di giustificare le fasi individuate sulla base della lettura di opportuni diagrammi di fase ternari in quanto considerate fasi di equilibrio. Per raggiungere tale scopo il lavoro è stato diviso in due parti:

1. Valutazione dell'effetto di stabilizzazione fornito dall'entropia configurazionale attraverso opportuni trattamenti termici e caratterizzazione dei campioni;
2. Previsione delle fasi ottenute in accordo ai diagrammi di fase ternari.

Il punto 1) si fonda sulle seguenti considerazioni. Come detto in §6.1, la presenza di composti intermetallici è stata diagnosticata in studi precedenti a seguito di trattamenti termici o termomeccanici. Contrariamente a quei lavori, al fine di aver la certezza di aver concesso tutto il tempo necessario ai processi diffusivi di prendere atto e dunque di portare il sistema alle condizioni effettive di equilibrio e al fine di separare effetti termomeccanici da quelli solamente termodinamici, i campioni di $Al_xCrFeCoNiCu$ sono stati sottoposti a trattamenti di invecchiamento di 1000 ore a diverse temperature (700°C, 850°C e 1000°C) direttamente dalla condizione di lingotto (as cast) e poi temprate in acqua per congelare a temperatura ambiente la microstruttura posseduta ad alta temperatura. Un tempo di 1000h si ipotizza sufficiente a consentire al sistema di raggiungere la struttura di equilibrio termodinamico, anche ammettendo lo stato di diffusione lenta ipotizzato nelle HEA. Grazie alla tempra, i campioni esaminati sono rappresentativi della microstruttura di equilibrio alla rispettiva temperatura di trattamento. L'analisi di tali campioni rivela se in condizioni di equilibrio termodinamico separazioni di fase e formazione di intermetallici sono effettivamente soppresse dalla variazione di entropia configurazionale dovuta al mix di sei elementi.

Il punto 2) si basa sul fatto che tutte le tecniche di caratterizzazione impiegate in questo lavoro hanno rivelato numerose fasi intermetalliche e segregazioni anche dopo il lungo trattamento di invecchiamento ad alta temperatura. Pertanto, intermetallici e segregazioni di fase sono stabili termodinamicamente e l'entropia configurazionale non è sufficiente a stabilizzare la soluzione solida. Il fatto che siano fasi di equilibrio suggerisce che esse possano essere predette dai diagrammi di fase ternari opportuni in termini di limiti di solubilità ed equilibri di fase. I precedenti lavori di Otto *et al.* [14] e Senkov *et al.* [15] hanno infatti evidenziato correlazioni tra fasi in HEA e diagrammi binari. L'obiettivo è estendere ai diagrammi ternari tale ragionamento ed usarli per motivare le fasi diagnosticate in termini di limiti di solubilità ed equilibri di fase.

Gli scopi prefissati sono stati raggiunti applicando il seguente programma di indagine:

1. Tre leghe $Al_xCrFeCoNiCu$ (x = 0,5; 1; 3) sono state preparate in forno ad arco sottovuoto al fine di valutare l'influenza del tenore di Al sulla microstruttura e sugli equilibri di fase. Le composizioni sono riassunte in tabella Table 3.1.

Identification	Formula	Al	Cr	Fe	Co	Ni	Cu
HEA5	$Al_{0.5}CrFeCoNiCu$	9.0	18.2	18.2	18.2	18.2	18.2
HEA6	AlCrFeCoNiCu	16.7	16.7	16.7	16.7	16.7	16.7
HEA7	$Al_3CrFeCoNiCu$	37.5	12.5	12.5	12.5	12.5	12.5

Table 3.1: Composizione nominale delle leghe analizzate

2. Da ciascun lingotto sono state ricavate tre fette da sottoporre a trattamento termico di 1000h a tre diverse temperature (700°C, 850°C e 1000°C) per assicurare il raggiungimento dell'equilibrio termodinamico e quindi temprate in acqua;
3. Microscopia Elettronica a Scansione ad elettroni retrodiffusi per evidenziare il contrasto composizionale tra le diverse fasi;
4. Microanalisi EDX di ciascuna fase e mappe elementali per evidenziare partizionamento degli elementi;
5. Diffrazione a Raggi X al fine di identificare le strutture cristallografiche presenti in ciascun stato;
6. Calorimetria a Scansione Differenziale per monitorare la formazione di fasi in seguito a riscaldamento;
7. Ampia revisione dei diagrammi di fase ternari.

6.3 RISULTATI E DISCUSSIONE

L'estesa descrizione dei risultati e della relativa discussione per ciascuna delle leghe analizzate è riportata in §4. Il quadro riassuntivo delle principali fasi costituenti ciascuna lega in ciascun stato è riportato in Table 5.1. Le caratteristiche salienti di ciascuna sono di seguito riassunte:

HEA5 $Al_{0.5}CrFeCoNiCu$:

- La fase dendritica è una soluzione satura basata su Ni-Co con struttura cristallina A1 (*cfc*).

- La segregazione del Cu è termodinamicamente stabile ad ogni temperatura e dunque ineliminabile. Inoltre si tratta di una fase fondente a temperature decisamente inferiore rispetto alle dendriti.
- La precipitazione di composti intermetallici NiAl (B2) e σ ha luogo in seguito ai trattamenti termici a 700°C e 850°C in accordo con quanto previsto dai limiti di solubilità di Al e Cr nelle regioni dendritiche ed interdentritiche (§2.3.4 e §2.3.7);
- La precipitazione di Ni_3Al non è cinematicamente bloccata durante il raffreddamento dalla presunta diffusione lenta caratteristica delle HEAs.

HEA6 AlCrFeCoNiCu:

- Dato l'incremento del tenore di Al, la matrice dendritica non è più una soluzione solida A1 ma interamente di natura intermetallica NiAl anche alla temperatura di 1000°C. Ciò è in accordo con il diagramma di fase ternario AlCrNi che prevede lo spostamento dai campi A1+$L1_2$ a A2+B2 all'aumentare del tenore di Al.
- La segregazione del Cu è ancora presente e termodinamicamente stabile anche ad alta temperatura.
- La precipitazione di fase σ e precipitati A1 ricchi in Fe,Cr si manifesta come previsto dai limiti di solubilità di NiAl nei diagrammi ternari AlNiX (§2.3.1).

HEA7 Al_3CrFeCoNiCu:

- Il contenuto di Al (37,5% nominale) è sufficiente a garantire la solubilità del Cu nella matrice intermetallica di NiAl alle temperature di 700°C e 850°C. Tuttavia, a 1000°C la fase $Cu_{0.75}Al_{0.25}$ stabile ad alta temperature e con struttura cristallina A2 segrega dalla matrice (§2.3.6).
- La precipitazione di fase σ è inibita dall'elevato tenore di Al. (§2.3.3). Tuttavia la formazione di precipitati ricchi in Cr,Fe e con struttura A2 ha luogo come predetto dai limiti di solubilità di Cr in NiAl (§2.3.1).

	HEA5 $Al_{0.5}$CrFeCoNiCu				
	DR	ID	PRECIPITATES		
AS CAST	Ni,Co,Cr,Fe A1	Cu-rich A1	Ni_3Al $L1_2$	-	-
1000°C	Ni,Co,Cr,Fe A1	Cu-rich A1	Ni_3Al $L1_2$	-	-
850°C	Ni,Co,Cr,Fe A1	Cu-rich A1	Cu-rich A1	NiAl B2	Cr,Co,Fe σ
700°C	Ni,Co,Cr,Fe A1	Cu-rich A1	Ni_3Al $L1_2$	NiAl B2	Cr,Co,Fe σ
	HEA6 AlCrFeCoNiCu				
	DR	ID	PRECIPITATES		
AS CAST	Cr,Fe,Co,Ni A2	Cu-rich A1	Cu-rich A1	NiAl B2	-
1000°C	NiAl B2	Cu-rich A1	-	Cr,Co,Fe A2	Fe,Cr A1
850°C	NiAl B2	Cu-rich A1	Cu-rich A1	Cr,Co,Fe σ	Fe,Cr A1
700°C	NiAl B2	Cu-rich A1	Cu-rich A1	Cr,Co,Fe σ	Fe,Cr A1
	HEA7 Al_3CrFeCoNiCu				
	DR	ID	PRECIPITATES		
AS CAST	NiAl B2	$Cu_{0.75}Al_{0.25}$ A2	Cr,Fe A2	-	-
1000°C	NiAl B2	$Cu_{0.75}Al_{0.25}$ A2	Cr,Fe A2	-	-
850°C	NiAl B2	-	Cr,Fe A2	-	-
700°C	NiAl B2	-	Cr,Fe A2	-	-

Table 5.1: Quadro riassuntivo

6.4 CONCLUSIONI

Le evidenze sperimentali sintetizzate in §6.3 permettono di concludere che:

1. Anche a temperature prossime a quelle di *liquidus* della fase interdentritica, l'entropia configurazionale non è sufficiente a controbilanciare la tendenza alla segregazione dovuta all'entalpia di miscelazione positiva. Questa microsegregazione è termodinamicamente stabile e non è eliminabile mediante trattamento termico, contrariamente ad altri sistemi metallici strutturali quali acciai e leghe di Ni.

2. Il partizionamento di elementi in più fasi riduce drasticamente l'entropia configurazione di ciascuna di esse: la loro stabilità contro la formazione di intermetallici è dunque ridotta rispetto alla previsione teorica. Per queste ragioni i composti intermetallici si riscontrano in tutti i campioni. Aumentando il tenore di Al (es: HEA6, equimolare) NiAl diventa addirittura la matrice principale.
3. La possibilità di creare un'unica soluzione solida tramite alligazione di 5 o più elementi non è garantita dal solo contributo dell'entropia configurazionale (cioè aumentando il numero di elementi). Un'unica soluzione solida può essere ottenuta quando gli elementi costitutivi mostrano estesi campi di soluzioni solide senza intermetallici nei loro diagrammi binari e ternari.
4. In quanto termodinamicamente stabili, le fasi in equilibrio alle diverse temperature e la formazione di intermetallici nel sistema $Al_xCrFeCoNiCu$ può essere previsto dall'analisi dei diagrammi ternari convenzionali.
5. La microstruttura non è controllata dalla massimizzazione dell'entropia configurazionale ma dalla minimizzazione dell'energia libera di Gibbs complessiva dei contributi entalpici ed entropici (non solo configurazionali, ma anche elettronici e magnetici).

Da un punto di vista applicativo, la segregazione ineliminabile del Cu in una fase fondente attorno ai 1150°C vieta l'impiego di questi materiali per le componenti ad alta temperatura dei motori a gas. Inoltre l'estesa formazione di composti intermetallici fragili ne rende difficile il controllo microstrutturale e la processabilità.

In conclusione, nelle leghe ad alta entropia $Al_xCrFeCoNiCu$ l'effetto dell'entropia configurazionale non gioca un ruolo di stabilizzazione efficace contro l'evoluzione microstrutturale quando sottoposte a temperatura elevata. Per tale ragione, le $Al_xCrFeCoNiCu$ HEAs non possono essere considerati materiali adatti per applicazioni ad alta temperatura.

REFERENCES

[1] J.-W. Yeh, S.-K. Chen, S.-J. Lin, J.-Y. Gan, T.-S. Chin, T.-T. Shun, C.-H. Tsau, and S.-Y. Chang, "Nanostructured High-Entropy Alloys with Multiple Principal Elements: Novel Alloy Design Concepts and Outcomes," *Adv. Eng. Mater.*, vol. 6, no. 5, pp. 299–303, May 2004.

[2] C. Tong, Y. Chen, S. Chen, J. Yeh, T. Shun, C. Tsau, S. Lin, and S. Chang, "Microstructure Characterization of Al x CoCrCuFeNi High-Entropy Alloy System with Multiprincipal Elements," *Metall. Mater. Trans. A*, vol. 36, no. A, pp. 881–893, 2005.

[3] Y. Y. Chen, U. T. Hong, H. C. Shih, J. W. Yeh, and T. Duval, "Electrochemical kinetics of the high entropy alloys in aqueous environments—a comparison with type 304 stainless steel," *Corros. Sci.*, vol. 47, no. 11, pp. 2679–2699, Nov. 2005.

[4] Y. Y. Chen, T. Duval, U. D. Hung, J. W. Yeh, and H. C. Shih, "Microstructure and electrochemical properties of high entropy alloys—a comparison with type-304 stainless steel," *Corros. Sci.*, vol. 47, no. 9, pp. 2257–2279, Sep. 2005.

[5] Y.-J. Hsu, W.-C. Chiang, and J.-K. Wu, "Corrosion behavior of FeCoNiCrCux high-entropy alloys in 3.5% sodium chloride solution," *Mater. Chem. Phys.*, vol. 92, no. 1, pp. 112–117, Jul. 2005.

[6] C.-Y. Hsu, C.-C. Juan, W.-R. Wang, T.-S. Sheu, J.-W. Yeh, and S.-K. Chen, "On the superior hot hardness and softening resistance of AlCoCrxFeMo0.5Ni high-entropy alloys," *Mater. Sci. Eng. A*, vol. 528, no. 10–11, pp. 3581–3588, Apr. 2011.

[7] J.-W. Yeh, "US20020159914: High-entropy multielement alloys," 2002.

[8] P. Huang, J. Yeh, T. Shun, and S. Chen, "Multi- Principal- Element Alloys with Improved Oxidation and Wear Resistance for Thermal Spray Coating," *Adv. Eng. Mater.*, vol. 6, no. 1- 2, pp. 74–78, 2004.

[9] J.-W. Yeh, S.-J. Lin, T.-S. Chin, J.-Y. Gan, S.-K. Chen, T.-T. Shun, C.-H. Tsau, and S.-Y. Chou, "Formation of simple crystal structures in Cu-Co-Ni-Cr-Al-Fe-Ti-V alloys with multiprincipal metallic elements," *Metall. Mater. Trans. A*, vol. 35, no. 8, pp. 2533–2536, 2004.

[10] T.-T. Shun and Y.-C. Du, "Microstructure and tensile behaviors of FCC Al0.3CoCrFeNi high entropy alloy," *J. Alloys Compd.*, vol. 479, no. 1–2, pp. 157–160, Jun. 2009.

[11] T.-T. Shun and Y.-C. Du, "Age hardening of the Al0.3CoCrFeNiC0.1 high entropy alloy," *J. Alloys Compd.*, vol. 478, no. 1–2, pp. 269–272, Jun. 2009.

[12] C. Ng, S. Guo, J. Luan, S. Shi, and C. T. Liu, "Entropy-driven phase stability and slow diffusion kinetics in an Al0.5CoCrCuFeNi high entropy alloy," vol. 31, pp. 165–172, 2012.

[13] N. G. Jones, J. W. Aveson, B. D. Conduit, and H. J. Stone, "On the phase stability of an Al0.5CrFeCoNiCu high entropy alloy," *Unpubl. Work.*

[14] F. Otto, Y. Yang, H. Bei, and E. George, "Relative effects of enthalpy and entropy on the phase stability of equiatomic high-entropy alloys," *Acta Mater.*, vol. 61, pp. 2628–2638, 2013.

[15] O. N. Senkov, S. V. Senkova, C. Woodward, and D. B. Miracle, "Low-density, refractory multi-principal element alloys of the Cr–Nb–Ti–V–Zr system: Microstructure and phase analysis," *Acta Mater.*, vol. 61, no. 5, pp. 1545–1557, Mar. 2013.

[16] B. Cantor, I. T. H. Chang, P. Knight, and a. J. B. Vincent, "Microstructural development in equiatomic multicomponent alloys," *Mater. Sci. Eng. A*, vol. 375–377, pp. 213–218, Jul. 2004.

[17] W. Hume-Rothery, R. W. Smallman, and C. W. Haworth, "The structure of metals and alloys." The Institute of Metals, London, 1969.

[18] Y.-L. Chen, Y.-H. Hu, C.-W. Tsai, J.-W. Yeh, S.-K. Chen, and S.-Y. Chang, "Structural evolution during mechanical milling and subsequent annealing of Cu–Ni–Al–Co–Cr–Fe–Ti alloys," *Mater. Chem. Phys.*, vol. 118, no. 2–3, pp. 354–361, Dec. 2009.

[19] Y.-S. Huang, L. Chen, H.-W. Lui, M.-H. Cai, and J.-W. Yeh, "Microstructure, hardness, resistivity and thermal stability of sputtered oxide films of AlCoCrCu0.5NiFe high-entropy alloy," *Mater. Sci. Eng. A*, vol. 457, no. 1–2, pp. 77–83, May 2007.

[20] O. N. Senkov, G. B. Wilks, D. B. Miracle, C. P. Chuang, and P. K. Liaw, "Refractory high-entropy alloys," *Intermetallics*, vol. 18, no. 9, pp. 1758–1765, Sep. 2010.

[21] O. N. Senkov, G. B. Wilks, J. M. Scott, and D. B. Miracle, "Mechanical properties of Nb25Mo25Ta25W25 and V20Nb20Mo20Ta20W20 refractory high entropy alloys," *Intermetallics*, vol. 19, no. 5, pp. 698–706, May 2011.

[22] O. N. Senkov, J. M. Scott, S. V. Senkova, D. B. Miracle, and C. F. Woodward, "Microstructure and room temperature properties of a high-

entropy TaNbHfZrTi alloy," *J. Alloys Compd.*, vol. 509, no. 20, pp. 6043–6048, May 2011.

[23] F. J. Wang, Y. Zhang, and G. L. Chen, "Atomic packing efficiency and phase transition in a high entropy alloy," *J. Alloys Compd.*, vol. 478, no. 1–2, pp. 321–324, Jun. 2009.

[24] B. Ren, Z. X. Liu, D. M. Li, L. Shi, B. Cai, and M. X. Wang, "Effect of elemental interaction on microstructure of CuCrFeNiMn high entropy alloy system," *J. Alloys Compd.*, vol. 493, no. 1–2, pp. 148–153, Mar. 2010.

[25] L. H. Wen, H. C. Kou, J. S. Li, H. Chang, X. Y. Xue, and L. Zhou, "Effect of aging temperature on microstructure and properties of AlCoCrCuFeNi high-entropy alloy," *Intermetallics*, vol. 17, no. 4, pp. 266–269, Apr. 2009.

[26] D. A. Porter and K. E. Easterling, *Phase Transformations in Metals and Alloys*. CRC Press, 1992.

[27] R. A. Swalin and R. A. Swalin, *Thermodynamics of solids*. J. Wiley New York, NY, 1972.

[28] U. S. Hsu, U. D. Hung, J. W. Yeh, S. K. Chen, Y. S. Huang, and C. C. Yang, "Alloying behavior of iron, gold and silver in AlCoCrCuNi-based equimolar high-entropy alloys," *Mater. Sci. Eng. A*, vol. 460–461, pp. 403–408, Jul. 2007.

[29] K. Rzyman and Z. Moser, "Calorimetric studies of the enthalpies of formation of Al3Ni2, AlNi and AlNi3," *Prog. Mater. Sci.*, vol. 49, no. 3–4, pp. 581–606, Jan. 2004.

[30] K.-C. Hsieh, C.-F. Yu, W.-T. Hsieh, W.-R. Chiang, J. S. Ku, J.-H. Lai, C.-P. Tu, and C. C. Yang, "The microstructure and phase equilibrium of new high performance high-entropy alloys," *J. Alloys Compd.*, vol. 483, no. 1–2, pp. 209–212, Aug. 2009.

[31] W.-R. Wang, W.-L. Wang, S.-C. Wang, Y.-C. Tsai, C.-H. Lai, and J.-W. Yeh, "Effects of Al addition on the microstructure and mechanical property of AlxCoCrFeNi high-entropy alloys," *Intermetallics*, vol. 26, pp. 44–51, Jul. 2012.

[32] H.-P. Chou, Y.-S. Chang, S.-K. Chen, and J.-W. Yeh, "Microstructure, thermophysical and electrical properties in AlxCoCrFeNi ($0 \leq x \leq 2$) high-entropy alloys," *Mater. Sci. Eng. B*, vol. 163, no. 3, pp. 184–189, Jul. 2009.

[33] C.-C. Tung, J.-W. Yeh, T. Shun, S.-K. Chen, Y.-S. Huang, and H.-C. Chen, "On the elemental effect of AlCoCrCuFeNi high-entropy alloy system," *Mater. Lett.*, vol. 61, no. 1, pp. 1–5, Jan. 2007.

[34] S. Singh, N. Wanderka, B. S. Murty, U. Glatzel, and J. Banhart, "Decomposition in multi-component AlCoCrCuFeNi high-entropy alloy," *Acta Mater.*, vol. 59, no. 1, pp. 182–190, Jan. 2011.

[35] C.-M. Lin and H.-L. Tsai, "Equilibrium phase of high-entropy FeCoNiCrCu0.5 alloy at elevated temperature," *J. Alloys Compd.*, vol. 489, no. 1, pp. 30–35, Jan. 2010.

[36] S.-T. Chen, W.-Y. Tang, Y.-F. Kuo, S.-Y. Chen, C.-H. Tsau, T.-T. Shun, and J.-W. Yeh, "Microstructure and properties of age-hardenable AlxCrFe1.5MnNi0.5 alloys," *Mater. Sci. Eng. A*, vol. 527, no. 21–22, pp. 5818–5825, Aug. 2010.

[37] M.-H. Chuang, M.-H. Tsai, W.-R. Wang, S.-J. Lin, and J.-W. Yeh, "Microstructure and wear behavior of AlxCo1.5CrFeNi1.5Tiy high-entropy alloys," *Acta Mater.*, vol. 59, no. 16, pp. 6308–6317, Sep. 2011.

[38] Y.-F. Kao, T.-J. Chen, S.-K. Chen, and J.-W. Yeh, "Microstructure and mechanical property of as-cast, -homogenized, and -deformed AlxCoCrFeNi (0≤x≤2) high-entropy alloys," *J. Alloys Compd.*, vol. 488, no. 1, pp. 57–64, Nov. 2009.

[39] C.-W. Tsai, M.-H. Tsai, J.-W. Yeh, and C.-C. Yang, "Effect of temperature on mechanical properties of Al0.5CoCrCuFeNi wrought alloy," *J. Alloys Compd.*, vol. 490, no. 1–2, pp. 160–165, Feb. 2010.

[40] T.-T. Shun, C.-H. Hung, and C.-F. Lee, "The effects of secondary elemental Mo or Ti addition in Al0.3CoCrFeNi high-entropy alloy on age hardening at 700°C," *J. Alloys Compd.*, vol. 495, no. 1, pp. 55–58, Apr. 2010.

[41] W.-Y. Tang, M.-H. Chuang, H.-Y. Chen, and J.-W. Yeh, "Microstructure and mechanical performance of new Al0.5CrFe1.5MnNi0.5 high-entropy alloys improved by plasma nitriding," *Surf. Coatings Technol.*, vol. 204, no. 20, pp. 3118–3124, Jul. 2010.

[42] M. Tsai, H. Yuan, G. Cheng, W. Xu, W. W. Jian, M. Chuang, C. Juan, A. Yeh, S. Lin, and Y. Zhu, "Intermetallics Significant hardening due to the formation of a sigma phase matrix in a high entropy alloy," *Intermetallics*, vol. 33, pp. 81–86, 2013.

[43] Y.-L. Chen, C.-W. Tsai, C.-C. Juan, M.-H. Chuang, J.-W. Yeh, T.-S. Chin, and S.-K. Chen, "Amorphization of equimolar alloys with HCP elements during mechanical alloying," *J. Alloys Compd.*, vol. 506, no. 1, pp. 210–215, Sep. 2010.

[44] T. K. Chen, T. T. Shun, J. W. Yeh, and M. S. Wong, "Nanostructured nitride films of multi-element high-entropy alloys by reactive DC sputtering," *Surf. Coatings Technol.*, vol. 188–189, pp. 193–200, Nov. 2004.

[45] B. S. Li, Y. P. Wang, M. X. Ren, C. Yang, and H. Z. Fu, "Effects of Mn, Ti and V on the microstructure and properties of AlCrFeCoNiCu high entropy alloy," *Mater. Sci. Eng. A*, vol. 498, no. 1–2, pp. 482–486, Dec. 2008.

[46] Z. Liu, S. Guo, X. Liu, J. Ye, Y. Yang, X.-L. Wang, L. Yang, K. An, and C. T. Liu, "Micromechanical characterization of casting-induced inhomogeneity in an Al0.8CoCrCuFeNi high-entropy alloy," *Scr. Mater.*, vol. 64, no. 9, pp. 868–871, May 2011.

[47] A. Munitz, M. J. Kaufman, J. P. Chandler, H. Kalaantari, and R. Abbaschian, "Materials Science & Engineering A Melt separation phenomena in CoNiCuAlCr high entropy alloy containing silver," vol. 560, pp. 633–642, 2013.

[48] Y. J. Zhou, Y. Zhang, Y. L. Wang, and G. L. Chen, "Solid solution alloys of AlCoCrFeNiTi[sub x] with excellent room-temperature mechanical properties," *Appl. Phys. Lett.*, vol. 90, no. 18, p. 181904, 2007.

[49] C. Li, J. C. Li, M. Zhao, and Q. Jiang, "Effect of alloying elements on microstructure and properties of multiprincipal elements high-entropy alloys," *J. Alloys Compd.*, vol. 475, no. 1–2, pp. 752–757, May 2009.

[50] C. Li, J. C. Li, M. Zhao, and Q. Jiang, "Effect of aluminum contents on microstructure and properties of AlxCoCrFeNi alloys," *J. Alloys Compd.*, vol. 504, pp. S515–S518, Aug. 2010.

[51] C.-M. Lin and H.-L. Tsai, "Evolution of microstructure, hardness, and corrosion properties of high-entropy Al0.5CoCrFeNi alloy," *Intermetallics*, vol. 19, no. 3, pp. 288–294, Mar. 2011.

[52] T.-T. Shun, C.-H. Hung, and C.-F. Lee, "Formation of ordered/disordered nanoparticles in FCC high entropy alloys," *J. Alloys Compd.*, vol. 493, no. 1–2, pp. 105–109, Mar. 2010.

[53] F. R. De Boer, R. Boom, W. C. M. Mattens, A. R. Miedema, and A. K. Niessen, *Cohesion in Metals. Transition Metal Alloys: Cohesion and Structure*, vol. 1. North-Holland, Amsterdam, 1989.

[54] K. Zhang and Z. Fu, "Effects of annealing treatment on properties of CoCrFeNiTiAlx multi-component alloys," *Intermetallics*, vol. 28, pp. 34–39, Sep. 2012.

[55] G. M. Paolucci, *Lezioni di metallurgia per laurea in ingegneria meccanica*, no. v. 1. Progetto Libreria, 2002.

[56] G. Sauthoff, *Intermetallics*. Wiley, 2008.

[57] C. Hammond, *The Basics of Crystallography and Diffraction*. OUP Oxford, 2009.

[58] H. Okamoto and K. Cenzual, "ASM Alloy Phase Diagram Database," 2013. [Online]. Available: www1.asminternational.org/asmenterprise/apd/.

[59] Y. I. Dutchak and V. G. Chekh, "High Temperature X-Ray Diffraction Study of the Lattice Dynamics of the Compounds AlCo and AlNi," *Russ J Phys Chem*, vol. 55, pp. 2342–2345, 1981.

[60] J. Miettinen, "Thermodynamic description of the Cu–Al–Ni system at the Cu–Ni side," *Calphad*, vol. 29, no. 1, pp. 40–48, 2005.

[61] R. C. Reed, *The Superalloys: Fundamentals and Applications*. Cambridge University Press, 2006.

[62] J. H. Westbrook, *Intermetallic compounds*. Wiley, 1967.

[63] R. Kainuma, M. Ise, C.-C. Jia, H. Ohtani, and K. Ishida, "Phase equilibria and microstructural control in the Ni-Co-Al system," *Intermetallics*, vol. 4, pp. S151–S158, 1996.

[64] L. Zhang and Y. Du, "Thermodynamic description of the Al–Fe–Ni system over the whole composition and temperature ranges: Modeling coupled with key experiment," *Calphad*, vol. 31, no. 4, pp. 529–540, 2007.

[65] P. Rogl, "Aluminium-Chromium-Nichel," in in *Ternary Alloys—A Comprehensive Compendium of Evaluated Constitutional Data and Phase Diagrams*, vol. 4, VCH, Weinheim, FRG, 1991, pp. 400–415.

[66] T. Chart, A. Dinsdale, and F. Putland, "The NPL ALLOYDATA Bank: Its Use in the Calculation of Phase Diagrams for Super-Alloy Development," in *Spec. Publ.-Chem. Soc.(Ind. Use Thermochem. Data, Proc. Conf., 1979)*, 1980, vol. 34, pp. 235–245.

[67] G. V Raynor and V. G. Rivlin, "Al-Cr-Fe," in in *Phase Equilibria in Iron Ternary Alloys*, London, 1988, pp. 81–97.

[68] A. Prince, "Aluminium-Copper-Nickel," in in *Ternary Alloys—A Comprehensive Compendium of Evaluated Constitutional Data and Phase Diagrams*, 1991, pp. 597–629.

[69] S. Ochial, Y. Oya, and T. Suzuki, "Alloying behaviour of Ni3Al, Ni3Ga, Ni3Si and Ni3Ge," *Acta Metall.*, vol. 32, no. 2, pp. 289–298, 1984.

[70] M. J. Donachie, *Superalloys: A Technical Guide*. ASM International, 2002.

[71] A. Taylor and R. W. Floyd, "The constitution of nickel-rich alloys of the nickel-chromium-aluminium system," *J. Inst. Met.*, vol. 81, pp. 451–464, 1952.

[72] Y. Mishima, Y. M. Hong, and T. Suzuki, "Determination of the γ solvus surface in Ni Al X ternary systems," *Mater. Sci. Eng. A*, vol. 146, no. 1–2, pp. 123–130, 1991.

[73] Y. Mishima, S. Ochiai, P. Machinery, and M. Science, "Lattice parameters of Ni (y), Ni3Al (y') and Ni3Ga (y ') solid solutions with additions of transition and b-subgroup elements," 1984.

[74] E. P. Abrahamson and S. L. Lopata, "The Lattice Parameters And Solubility Limits Of Alpha Iron As Affected By Some Binary Transition-Element Additions.," *Trans. Metall. Soc. AIME*, vol. 27, pp. 76–87, 1966.

[75] G. J. Dickins, A. M. B. Douglas, and W. H. Taylor, "Structure of the Sigma-Phase in the Iron-Chromium and Cobalt-Chromium Systems," *Nature*, vol. 167, no. 4240, p. 192, Feb. 1951.

[76] J. W. Elmer, T. a. Palmer, and E. D. Specht, "In situ observations of sigma phase dissolution in 2205 duplex stainless steel using synchrotron X-ray diffraction," *Mater. Sci. Eng. A*, vol. 459, no. 1–2, pp. 151–155, Jun. 2007.

[77] L.-Å. Norström, S. Pettersson, and S. Nordin, "σ-Phase Embrittlement in Some ferritic-austenitic stainless steels," *Materwiss. Werksttech.*, vol. 12, no. 7, pp. 229–234, 1981.

[78] H. Okamoto, "Co-Cr (Cobalt-Chromium)," *J. Phase Equilibria*, vol. 24, no. 4, pp. 377–378, 2003.

[79] S.-L. Chen, J.-Y. Zhang, X.-G. Lu, K.-C. Chou, and Y. A. Chang, "Application of Graham scan algorithm in binary phase diagram calculation," *J. Phase Equilibria Diffus.*, vol. 27, no. 2, pp. 121–125, 2006.

[80] Y. A. Chang, J. P. Neumann, A. Mikula, and D. Goldberg, "Cu-Co-Cr," in in *Phase diagrams and thermodynamic properties of ternary copper-metal systems Vol. 6*, DTIC Document, 1979, pp. 416–417.

[81] E. S. Moskvitina, V. N. Kuznetsov, and L. S. Guzei, "Refinement of the Co-Cr-Al Phase Diagram," *Moscow Univ. Chem. Bull.*, vol. 47(4), pp. 70–71, 1992.

[82] A. A. Bondar, "Aluminium-Cobalt-Chromium," in in *Ternary Alloys—A Comprehensive Compendium of Evaluated Constitutional Data and Phase Diagrams*, vol. 4, VCH, Weinheim, FRG, 1991, pp. 159–167.

[83] F. H. Hayes, M. G. Hetherington, and R. D. Longbottom, "Thermodynamics of duplex stainless steels," *Mater. Sci. Technol.*, vol. 6, no. 3.

[84] K. P. Gupta, "The Co-Cr-Ni (cobalt-chromium-nickel) System," in in *Phase diagrams of ternary nickel alloys*, vol. 1, Indian institute of metals, 1990, pp. 5–17.

[85] G. V Raynor and V. G. Rivlin, "Co-Cr-Fe," in in *Phase Equilibria in Iron Ternary Alloys*, London, 1988, pp. 213–230.

[86] T. Nishizawa and K. Ishida, "Co-Ni," in in *Binary alloy phase diagrams*, vol. 2, T. B. Massalski, H. Okamoto, P. R. Subramanian, and L. Kacprzak, Eds. ASM international, 1990, pp. 1214–1215.

[87] K. S. Chan, Y.-M. Pan, and Y.-D. Lee, "Computation of Ni-Cr phase diagramvia a combined first-principles quantum mechanical and CALPHAD approach," *Metall. Mater. Trans. A*, vol. 37, no. 7, pp. 2039–2050, 2006.

[88] C.-W. Yang, D. B. Williams, and J. I. Goldstein, "A revision of the Fe-Ni phase diagram at low temperatures (< 400 C)," *J. phase equilibria*, vol. 17, no. 6, pp. 522–531, 1996.

[89] A. F. Guillermet, "Assessing the thermodynamics of the Fe□ CO□ Ni system using a calphad predictive technique," *Calphad*, vol. 13, no. 1, pp. 1–22, 1989.

[90] J. Sehramm, "Das Dreistoffsystem Nickel-Kobalt-Aluminium," *Zeitschrift für Met.*, vol. 33, pp. 403–412, 1941.

[91] N. Kamiya, T. Sakai, R. Kainuma, I. Ohnuma, and K. Ishida, "Phase separation of BCC phase in the Co-rich portion of Co-Fe-Al system," *Intermetallics*, vol. 12, no. 4, pp. 417–423, 2004.

[92] T. Kozakai, R. Okamoto, and T. Miyazaki, "Phase equilibria in the Fe-Al-Co ternary system at 923 K," *Zeitschrift für Met.*, vol. 90, no. 4, pp. 261–266, 1999.

[93] H. Okamoto, "Cr-Cu (chronium-copper)," *J. Phase Equilibria*, vol. 22, no. 6, pp. 691–692, 2001.

[94] M. Palumbo, S. Curiotto, and L. Battezzati, "Thermodynamic analysis of the stable and metastable Co–Cu and Co–Cu–Fe phase diagrams," *Calphad*, vol. 30, no. 2, pp. 171–178, 2006.

[95] S.-E. Amara, A. Belhadj, R. Kesri, and S. Hamar-Thibault, "Stable and metastable equilibria in the binary Fe-Cu and ternary Fe-Cu-C systems," *Zeitschrift für Met.*, vol. 90, no. 2, pp. 116–123, 1999.

[96] C. P. Wang, X. J. Liu, I. Ohnuma, R. Kainuma, and K. Ishida, "Phase Equilibria in Fe-Cu-X (X: Co, Cr, Si, V) Ternary Systems," *J. phase equilibria*, vol. 23, no. 3, pp. 236–245, 2002.

[97] G. W. Qin, G. Zhao, M. Jiang, H. X. Li, and S. M. Hao, "The isothermal sections of the Cu-Ni-Fe ternary system at 600, 800, 1000 and 1050 degrees C," *Zeitschrift fur Met.*, vol. 91, no. 5, pp. 379–382, 2000.

[98] K. P. Gupta, S. B. Rajendraprasad, and A. K. Jena, "The Cobalt--Copper--Nickel System," *J. Alloy Phase Diagrams*, vol. 3, no. 2, pp. 65–71, 1987.

[99] K. P. Gupta, S. B. Rajendraprasad, A. K. Jena, and R. C. Sharma, "The Chromium--Copper--Nickel System," *J. Alloy Phase Diagrams*, vol. 1, pp. 39–46, 1985.

[100] X. J. Liu, I. Ohnuma, R. Kainuma, and K. Ishida, "Phase equilibria in the Cu-rich portion of the Cu–Al binary system," *J. Alloys Compd.*, vol. 264, no. 1–2, pp. 201–208, 1998.

[101] E. Obrado, L. Manosa, and M. Planes, "Stability of the bcc phase of Cu-Al-Mn shape-memory alloys," *Phys. Rev. B*, vol. 56, no. 1, pp. 20–23, 1997.

[102] P. Michel, "Formation des alliages du système Al-Cu par évaporation sous vide de constituants purs," *Comptes Rendus Hebd. des Séances l'Académie des Sci.*, vol. 236, pp. 820–822, 1953.

[103] Q. Ran, "Aluminium-Cobalt-Copper," in in *Ternary Alloys—A Comprehensive Compendium of Evaluated Constitutional Data and Phase Diagrams*, vol. 4, 1991, pp. 168–174.

[104] B. Grushko, E. Kowalska-Strzęciwilk, B. Przepiórzyński, and M. Surowiec, "An investigation of the Al–Cu–Cr phase diagram: Phase equilibria at 800–1000° C," *J. Alloys Compd.*, vol. 417, no. 1, pp. 121–126, 2006.

[105] V. Raghavan, "The Al-Cu-Fe (Aluminium-Copper-Iron) System," in in *Phase Diagrams of Ternary Iron Alloys*, vol. 6A, 1992, pp. 86–95.

[106] A. Manzoni and H. Daoud, "Investigation of phases in Al23Co15Cr23Cu8Fe15Ni16 and Al8Co17Cr17Cu8Fe17Ni33 high entropy

alloys and comparison with equilibrium phases predicted," *J. Alloy.* …, vol. 552, pp. 430–436, 2013.

[107] A. Beskrovni, S. Danilkin, H. Fuess, E. Jadrowski, M. Neova-Baeva, and T. Wieder, "Effect of Cr content on the crystal structure and lattice dynamics of FCC Fe–Cr–Ni–N austenitic alloys," *J. Alloys Compd.*, vol. 291, no. 1–2, pp. 262–268, Sep. 1999.

[108] A. V Deryabin and V. I. Rimlyand, "On the Nature of Magnetic Volume Phenomena in Invar Alloys," *Phys. Met. Met.*, vol. 54, no. 3, pp. 185–187, 1982.

[109] H. A. Moreen, R. Taggart, and D. H. Polonis, "A model for the prediction of lattice parameters of solid solutions," *Metall. Trans.*, vol. 2, no. 1, pp. 265–268, 1971.

[110] D. Farkas, C. G. Schon, M. S. F. De Lima, and H. Goldenstein, "Embedded atom computer simulation of lattice distortion and dislocation core structure and mobility in Fe Cr alloys," *Acta Mater.*, vol. 44, no. 1, pp. 409–419, Jan. 1996.

[111] V. Raghavan, G. V Raynor, and V. G. Rivlin, "The Cr-Cu-Fe (Chromium-Copper-Iron) System," in in *Phase Diagrams of Ternary Iron Alloys*, vol. 6B, Indian Institute of Metals, 1992, pp. 687–688.

[112] A. T. Gorton, G. Bitsianes, and T. L. Joseph, "Thermal Expansion Coefficients for Iron and Its Oxides from X-Ray Diffraction Measurements at Elevated Temperatures," *Trans. Met. Soc. AIME*, vol. 233, no. 8, pp. 1519–1520, 1965.

ACKNOWLEDGEMENTS

First of all, I would like to thank my supervisor Prof. Franco Bonollo for the priceless opportunity he gave me to conduct my thesis at the University of Cambridge. This experience would not have been possible without his commitment. Many thanks also to Prof. Andrea Zambon for the encouragement during the first days and for his constant interest on my work. I am also extremely grateful to them for the full confidence in me.

I would like to express my gratitude to Dr. Howard Stone, head of Rolls-Royce UTC at the University of Cambridge, for giving me the opportunity to be part of the group for my thesis project. I thank him for the systematic guidance, for the enthusiastic interest, for the insightful suggestions and comments and for the great time dedicated to me in order to provide an explanation as much complete as possible to observed phenomena. I could not have imagined having a better advisor and mentor for my master thesis. It has been an honour to work with him.

I would like to express my gratitude to my direct supervisor Dr. Nicholas Jones for introducing me to the HEAs research, for having dedicated his time in solving my doubts and for his great work conducted before my arrival that represented an extremely valuable basis to start from and that allowed me to complete the experimental work in time. The long meetings with Dr. Howard Stone and Dr. Nicholas Jones were priceless educational opportunities to me.

My gratitude also goes to whole Rolls-Royce UTC research group at the University of Cambridge for the warm welcome and the great help provided. In particular, I would like to thank Steve, Sandy, Paul, John, Kathy, Caroline and Ana for the indispensable assistance in the labs and for the great time in the pubs. Many thanks also to the technical staff in the labs, especially in the X-Ray lab.

I would like to thank also some of the great people and friends that I have met during my stay in Cambridge. Tiziana for her great ideas and initiatives and for being my all-rounder adviser for college life; Frederich, Arjun, Ani and Maxime for our man-to-man talks; Claudia for being my emergency number; the Belgium crew for sharing the Blues; Marion for her kindness; Hervé for his help in and out the dojo.

Ritornando verso casa, voglio ringraziare anche tutti i miei amici della buona vecchia compagnia del mio paese perché, nonostante la mia presenza sia piuttosto intermittente, mi accolgono sempre a braccia aperte e generosamente. Voglio esprimere la mia gratitudine anche agli amici di karate, a tutta la vecchia guardia e al maestro Mion per la fiducia che costantemente ripongono in me, dandomi sempre grandissima carica.

Benché una cornice di 120 pagine di metallurgia non sia la più adatta, voglio comunque ringraziare in questa sede le persone che più mi sono care e vicine confidando nel valore simbolico di questo elaborato. Devo quindi esprimere un'immensa gratitudine alla mia famiglia e sovra ogni cosa a mia Mamma i cui sacrifici di un'intera vita sono ineguagliabili e impagabili. Non c'è moneta ne parola per ricambiare simile grandezza. Grazie ai miei zii Marilena, Alberto e Francesco per il supporto datomi in tutte le forme possibili e con assoluta generosità. Un grazie va al mio amico Mauro, la cui amicizia è stata cementata dalla condivisione delle fatiche universitarie ed extra-universitarie nell'arco di tutti gli ultimi cinque anni. Incondizionato affetto per lei, la mia splendida ragazza, che nonostante il periodo impegnativo e critico, ha saputo superarlo alla grande e con caparbietà. Bravissima Mati. Sono fiero di aver vinto assieme la lontananza e sono felice e fortunato di averti al mio fianco.

Un profondo ma sorridente pensiero va a mia nonna Milena, che senza ogni ombra di dubbio sarebbe stata la persona al mondo più felice per me per il completamento del mio percorso di studi. Per questa ragione ho dedicato questo lavoro a lei e alla sua genuina capacità di essere felice della felicità altrui. Ben al di là del contenuto puramente scientifico, lo sfogliare le pagine di questa tesi le avrebbe dato gioia e soddisfazione come a nessun altro.